

NFLC / TR 2023

NELC / TR 2023

AD A 038262

RADOME DEVELOPMENT FOR A BROADBAND RF MISSILE SENSOR

Multilayered power series radome with integrated lens
provides excellent drag characteristics and
electrical boresight error performance

FD Groutage

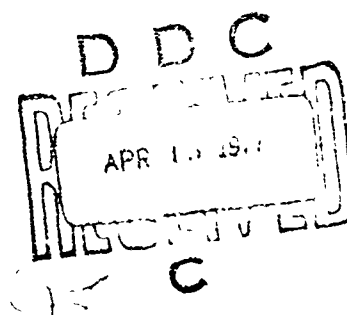
Research and Development, August through December 1976

25 January 1977

Prepared for
NAVAL AIR SYSTEMS COMMAND

APPROVED FOR PUBLIC RELEASE DISTRIBUTION IS UNLIMITED

NAVAL ELECTRONICS LABORATORY CENTER
SAN DIEGO, CALIFORNIA 92152



FILE COPY

DDC

UNCLASSIFIED

SECURITY CLASSIFICATION OF THIS PAGE (When Data Entered)

REPORT DOCUMENTATION PAGE		READ INSTRUCTIONS BEFORE COMPLETING FORM
1 REPORT NUMBER NELC Technical Report 2023 (TR 2023) ✓	2 GOVT ACCESSION NO.	3 RECIPIENT'S CATALOG NUMBER
4 TITLE (and Subtitle) RADOME DEVELOPMENT FOR A BROADBAND RE MISSILE SENSOR (Multilayered power series radome with integrated lens provides excellent drag characteristics and electrical boresight error performance) ✓	5 TYPE OF REPORT & PERIOD COVERED Research and Development rpt. August through December 1976	6 PERFORMING ORG. REPORT NUMBER
7 AUTHOR H. Grostige	8 CONTRACT OR GRANT NUMBER(s)	
9 PERFORMING ORGANIZATION NAME AND ADDRESS Naval Electronics Laboratory Center San Diego, California 92152	10 PROGRAM ELEMENT, PROJECT, TASK AREA & WORK UNIT NUMBERS 63601F, O. AF (NELC H101)	
11 CONTROLLING OFFICE NAME AND ADDRESS Naval Air Systems Command	12 REPORT DATE 25 January 1977	13 NUMBER OF PAGES 104
14 MONITORING AGENCY NAME & ADDRESS (if different from Controlling Office) NELC/TR-2023	15 SECURITY CLASS (of this report) Unclassified	15a DECLASSIFICATION/DOWNGRADING SCHEDULE
16 DISTRIBUTION STATEMENT (of this Report) Approved for public release; distribution is unlimited W447 W447		
17 DISTRIBUTION STATEMENT (of the abstract entered in Block 20, if different from Report)		
18 SUPPLEMENTARY NOTES		
19 KEY WORDS (Continue on reverse side if necessary and identify by block number) Boresight error Radomes Lenses Wave interference Missile guidance Frequency activated		
20 ABSTRACT (Continue on reverse side if necessary and identify by block number) An integrated radome/lens concept is developed for a multioctave rf radiation sensor guided missile application. Aerodynamic properties, drag, and thermal heating are analyzed. Electrical properties, transmissivity, and boresight error are optimized by using a layered wall construction and integrating a lens into the inner surface of the radome. Missile performance is evaluated with the integrated radome/lens used as part of the missile system.		

DD FORM 1 JAN 73 1473

EDITION OF 1 NOV 65 IS OBSOLETE

UNCLASSIFIED

SECURITY CLASSIFICATION OF THIS PAGE (When Data Entered)

403 940

‘

Define a baseline easy-to-manufacture and low-cost-in-production approach for a multioctave-band frequency coverage radome to interface with an rf missile guidance sensor system. The baseline (minimum-drag configuration) must optimize electrical performance in increasing transmissivity and reducing boresight error over the sensor range of look angles and across the frequency band of operation; it must also meet environmental (rain erosion and aerodynamic heating) requirements.

RESULTS

1. A baseline radome approach to meet preliminary design objectives was developed. The baseline was a multilayer-wall construction technique with a lens integrated into the final inner layer (support structure) to provide insertion phase compensation for reducing boresight error. The lens was effected by varying the inner wall shape relative to the outer wall shape.

2. Results of feasibility studies showed the integrated lens concept to be a unique insertion phase compensation technique for optimizing electrical boresight error performance (as compared to the unlensed radome) within a radome shape that provides excellent drag characteristic.

3. Preliminary choices of materials were examined for rain erosion and thermal heating properties. Within current state-of-the-art medium-range missile aerodynamic performance bounds, the preliminary material choices were found to be adequate for meeting environmental requirements. The layered-wall construction lends itself to inexpensive manufacturing by a molding process. The lens will not contribute to the cost of the radome -- cost is equivalent for manufacturing a molded object with inner and outer surfaces either the same shape or of different shape.

4. Missile performance was evaluated as a function of the nonlinear boresight error/error slope data. This analysis indicated radome boresight error slope specification requirements may be relaxed as compared to those specifications generated by analysis using a linearized boresight error slope.

RECOMMENDATION

1. Develop hardware to verify the feasibility findings.

ADMINISTRATIVE INFORMATION

Work was performed by the ERASE Project Office (NELC Code 1610) during the period from August through December 1976. The effort was directed by the Naval Air Systems Command, under Air Task A360360E/003C/7W0447 NAVAIRSYSCOM-AA-001 with 75% of the funds coming from NAVAIRSYSCOM, and 25% from Air Force ADTC/DLMI project order number ATL-T-S96. Cognizant personnel at the Naval Air Systems Command was Vytas Tarulis, AIR 360E. The cognizant technical personnel was Major John C Saffle, ADTC/AFATL DLMI, Eglin AFB, FL. The report was approved for publication by GS Borunda.

ACKNOWLEDGMENT

The author extends sincere appreciation to Daryl E Smith for his contribution to this report. Mr Smith was responsible for taking the mathematical models of the radomes and translating these models into computer programs for the computerized analysis effort.

METRICATION INFORMATION

Conventional Unit	Approx Metric Equivalent
btu/lb	2.3 kJ/kg
ft	0.3 m
lb	0.45 kg
lb/ft ³	16 kg/m ³
nmi	1.85 km
$t^{\circ}\text{C} = (t^{\circ}\text{F} - 32)/1.8$	
$t_{\text{K}} = t^{\circ}\text{C} + 273.15$	
$t_{\text{K}} = t^{\circ}\text{R}/1.8$	

CONTENTS

INTRODUCTION . . .	page 1
AERODYNAMIC CONSIDERATIONS . . .	2
Drag . . .	3
Structure . . .	8
ELECTRICAL PERFORMANCE . . .	16
Transmissivity . . .	16
Boresight Error . . .	27
MISSILE SYSTEM PERFORMANCE . . .	39
Seeker/Radome Model . . .	39
CONCLUSION . . .	59
Aerodynamic Considerations . . .	59
Electrical Performance . . .	60
Missile Performance . . .	61
SUMMARY . . .	62
RECOMMENDATIONS . . .	62
REFERENCES . . .	63
BIBLIOGRAPHY . . .	63
APPENDIX A: BORESIGHT ERROR PROGRAM MODEL . . .	65
APPENDIX B: BORESIGHT ERROR DATA . . .	87
APPENDIX C: ABLATION MODEL AND TEST DATA FOR AVCOAT 8027 . . .	95

ILLUSTRATIONS

1. Methodology for establishing radome performance requirements . . .	page 1
2. Effect of nose bluntness on 2.5:1 L/D tangent ogive nose zero lift drag coefficient . . .	5
3. Power series radome profile . . .	6
4. Zero lift drag coefficients for 2.5:1 L/D tangent ogive, hemi-ogive, and power series radomes . . .	7
5. Comparative radome shapes . . .	7
6. Comparative radomes . . .	8
7. Layered-wall construction . . .	9
8. Rain erosion results . . .	10
9. Rain penetration . . .	10
10. Maximum surface temperature vs radome axial station . . .	12
11. Maximum thermal stress vs radome axial station . . .	12
12. Summary data on AVCO 8027 . . .	14

13. Multistage impedance matching transmission line transformer . . . 17
14. Transmission loss vs frequency . . . 25
15. Transmission loss as a function of incident angle vs frequency . . . 26
16. Look angle definition . . . 27
17. Example of boresight error as a function of look angle . . . 28
18. Radome error caused by insertion phase . . . 29
19. Signal tracking without boresight error . . . 29
20. Signal tracking with boresight error . . . 30
21. Power series radome with integrated parabolic lens . . . 31
22. Radome/lens phase insertion compensation . . . 31
23. Examples of symmetrical phase (two dimensions) across antenna aperture . . . 32
24. Boresight error data (2-in-diameter antenna at 6-in station) . . . 33
25. Boresight error slope data for a compensated radome (2-in-diameter antenna at 6-in station) . . . 34
26. Boresight error data (4-in-diameter antenna at 12-in station) . . . 35
27. Boresight error slope data for a compensated radome (4-in-diameter antenna at 12-in station) . . . 36
28. Boresight error data (4-in-diameter antenna at 12-in station - alternate lens) . . . 37
29. Boresight error slope data for a compensated radome (alternate lens for 4-in diameter at 12-in station) . . . 38
30. Sensor/missile/target angular relationship . . . 40
31. Seeker tracker system block diagram . . . 40
32. Radome/seeker subsystem block diagram . . . 42
33. Missile guidance block diagram - with radome error . . . 44
34. Simplified missile guidance diagram including effects of radome error parasitic feedback loop . . . 45
35. Nonlinear radome/seeker subsystem block diagram . . . 48
36. Radome error vs look angle . . . 48
37. Linear models of boresight errors . . . 54
38. Miss distance as a function of radome error/error slope . . . 56

TABLES

1. Nose pressure drag coefficients . . . page 4
2. Summary of rainfield data . . . 9
3. AVCOAT 8027 performance estimates . . . 11
4. AFML rain erosion testing (subscale), Holloman AFB test track . . . 11
5. Boresight error data description . . . 38
6. Representative runs of missile-target encounters . . . 52

INTRODUCTION

A baseline configuration is presented here for a radome for high-speed missiles. The radome combines high aerodynamic performance with wide open sensitivity to threat radiation frequencies - it permits the use of multioctave sensors in missile guidance. Radome performance requirements are established through analysis and hardware development (fig 1). This report describes the analytical effort.

Basic radome requirement categories are electrical, aerodynamic, and structural.

The electrical requirements can be divided into two major areas - transmissivity and boresight error properties.

Broadband, multioctave frequency coverage is a baseline requirement on a missile using radiation sensing as a guidance mode. Broadband radiation sensors must be able to operate over all the frequencies that enemy targets radiate. This, in turn, places the requirement on the radome to operate over these same frequencies. However, the transmissivity requirements of a radome for a missile using passive radiation homing may not be as stringent as for the semiactive and active cases. This in part depends on the range requirement of the active sensor and the available transmitter power. The radiation loss for the passive case can be as high as 40% without violating minimum range operating requirements. Typically, semiactive and active radiation guidance sensors require radomes that are less lossy (on the order of 90% transmissivity). This is most evident in single-mode guidance systems. In multimode guidance systems the active system radome requirements could be more relaxed more on the order of those of passive systems. Additional data on the transmissivity property of radomes are presented in Electrical Performance.

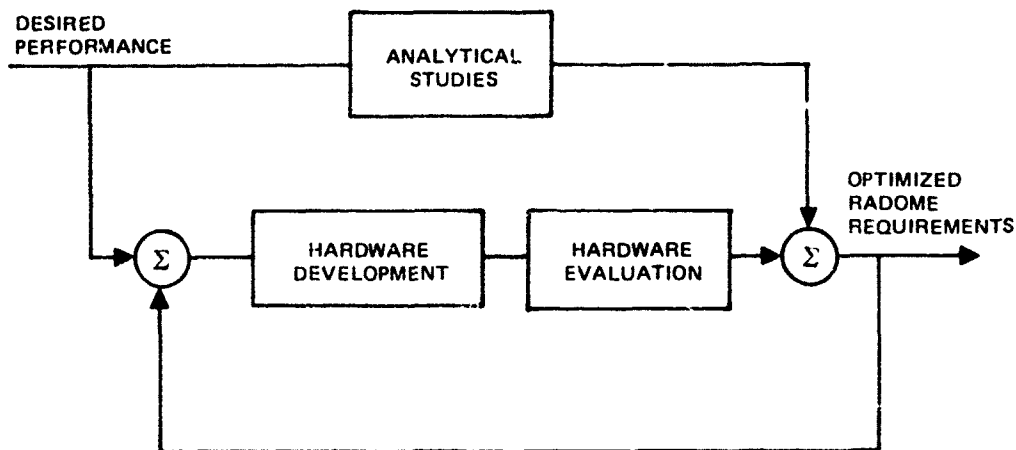


Figure 1. Methodology for establishing radome performance requirements.

The boresight error added to the sensor guidance signal by the radome is analogous to the displacement of a fish in a pool of water introduced by the air-water interface. The displacement of the apparent location from the actual location is due to a refracting of the light rays reflected from the fish as they pass through the boundary layer. The degree of refraction is dependent on the depth of the fish in the water and the angle of observation.

The boresight error is defined as the error in the direction of arrival of guidance information caused by the refracting properties of the radome. More than the boresight error itself, the rate of change of boresight error with sensor look angle (angle of direction of guidance information as seen by the sensor with respect to the centerline of the missile) is the quantity that affects the performance of a missile utilizing proportional navigation for guidance steering. Missile performance as a function of changes in boresight error is addressed in more detail in Missile System Performance.

Aerodynamic considerations play a major role in radome design, especially in the areas of shape and material. Shape sets aerodynamic drag whereas materials determine response to aerodynamic heating, dynamic pressure, and rain erosion.

Shape and materials also have major impact on electrical performance, both transmissivity and boresight error. The ideal electrical shape is not necessarily the best aerodynamic shape. A hemispherical radome is the optimum shape electrically. The optimum aerodynamic shape tends to be long and slender. Thus, the interdependence of parameters necessitates that compromise be a part of the design philosophy. The philosophy for developing a radome as outlined in this report specifies an aerodynamic shape that does not degrade missile flight performance as compared to that of a missile with a conventional tangent or von Karman ogive radome shape forebody. With the shape fixed, the requirement is to develop techniques for minimizing boresight error over the specified range of look angles and maximizing transmissivity over the frequency range while meeting the rain erosion, aeroheating, and dynamic pressure requirements. A unique and novel idea fell out of the analytical research. An integrated radome/lens for insertion phase compensation was developed. The development is presented in Electrical Performance.

The analysis to establish the performance of the integrated radome/lens concept was aided in part by a ray-tracing computer program. This program, described in appendix A, was used to evaluate boresight over the -45° to $+45^\circ$ look angle region. The analysis was done parametrically, as the boresight error is a function of at least seven variables. The variables and the methodology for conducting the analysis are described more fully in Electrical Performance. The parametric study produced a considerable volume of data, some of which are published in appendix B. The conclusions are in part based on data reduction of parametric data.

AERODYNAMIC CONSIDERATIONS

Primarily the two major areas of consideration relating to aerodynamic requirements which affect performance are drag and structure.

The two parameters are not independent of each other, and, moreover, the electrical performance is very much a function of these aerodynamic factors. Fortunately, the shapes that result in the best drag performance are those that lend themselves to meeting structural performance requirements. Unfortunately, the more desirable shapes from a drag viewpoint are not necessarily the best from the viewpoint of electrical performance. As stated earlier in the report, the decision to optimize drag performance determined the shape of the radome.

The specification of a technique for increasing electrical performance was the second phase of this development. The primary mission was to address air-to-air high-velocity/maneuvering missile intercepts.

DRAG

The drag for the missile can be broken into several components. The two major components are the zero lift drag and the induced drag. The induced drag is a function of the angle of attack. The discussion in this section will primarily be concerned with the zero lift drag, C_{DO} . The zero lift drag is a function of sea level plus a skin friction value:

$$C_{DO} = C_{DO} \text{ (sea level)} + \Delta C_D \text{ (skin friction)}$$

The zero lift, sea-level component is the factor of most concern. This is the component that is very dependent on shape.

SHAPES

Common shapes are:

- Hemisphere
- Cone
- Ogive
- Tangent
- Secant
- Von Karman
- Modified von Karman
- Power Series
- Modified power series
- Hemisphere/Ogive

There is an extensive literature on these radome shapes. Reference 1 provides an excellent overview of radome shapes and their mathematical descriptions. The NACA reports provide excellent detailed descriptions of drag and characteristics of the various radome shapes.

DRAG FOR ALTERNATE SHAPES

From an electrical standpoint, the hemisphere is optimum; however, this is a very high-drag configuration. An alternative is to put a small hemisphere nose tip on the end of an alternate shape with more desirable drag characteristics, such as a tangent ogive (commonly

¹Chin, SS, "Missile Configuration Design," McGraw-Hill Book Co. 1961

referred to as hemi-ogive). The sensor is miniaturized and located in the tip of the radome. The sensor then looks through a hemisphere yet the drag is somewhat less than it would be with a full hemisphere nose. To get a feel as to how the drag, C_{DO} , varies as a function of nose shape, length-to-diameter ratio (L/D), and mach number, tables 1A and 1B present drag data calculated by use of reference 2.

TABLE 1. NOSE PRESSURE DRAG COEFFICIENTS.

A Length of nose varies (see fig 2A)

M	C_{DO} nose					2.5:1 L/D Tangent Ogive
	D = 1 in	D = 2 in	D = 3 in	D = 4 in	D = 5 in	
1.0	0.065	0.07	0.075	0.09	0.125	0.055
1.25	0.05	0.06	0.065	0.09	0.13	0.05
1.50	0.125	0.13	0.14	0.185	0.255	0.128
1.75	0.145	0.15	0.17	0.22	0.29	0.16
2.0	0.14	0.15	0.175	0.245	0.32	0.15
3.0	0.145	0.17	0.20	0.28	0.375	0.14
4.0	0.14	0.17	0.22	0.29	0.395	0.13

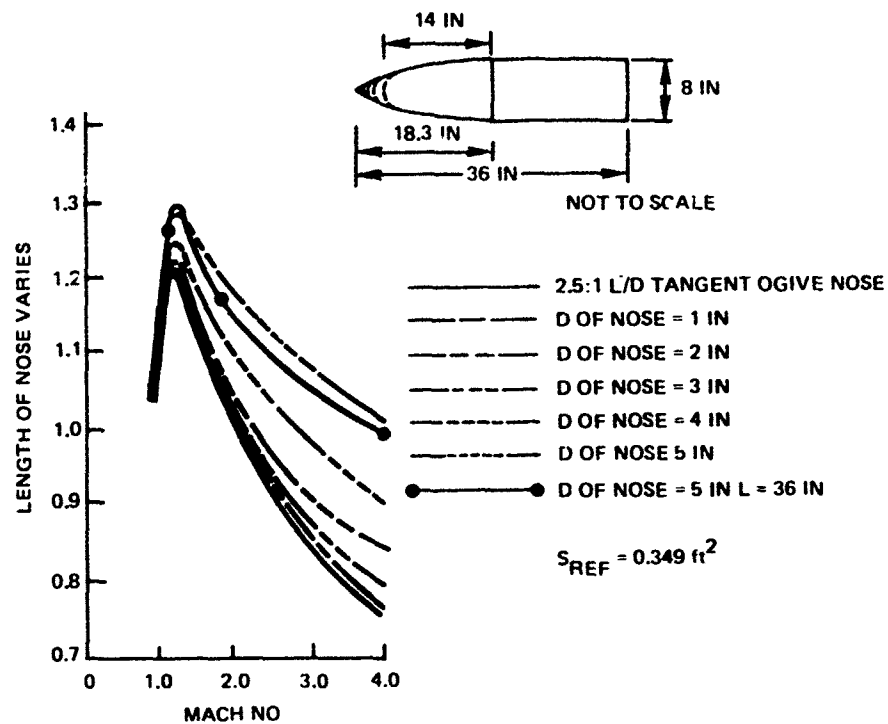
B. Length of nose = 18.3 in (see fig 2B)

M	C_{DO} nose					2.5:1 L/D Tangent Ogive
	D = 1 in	D = 2 in	D = 3 in	D = 4 in	D = 5 in	
1.0	0.065	0.065	0.07	0.085	0.115	0.055
1.25	0.06	0.06	0.07	0.08	0.13	0.05
1.50	0.125	0.12	0.135	0.175	0.245	0.128
1.75	0.14	0.135	0.15	0.205	0.275	0.16
2.0	0.14	0.14	0.17	0.225	0.31	0.15
3.0	0.14	0.155	0.19	0.265	0.36	0.14
4.0	0.13	0.16	0.20	0.28	0.38	0.13

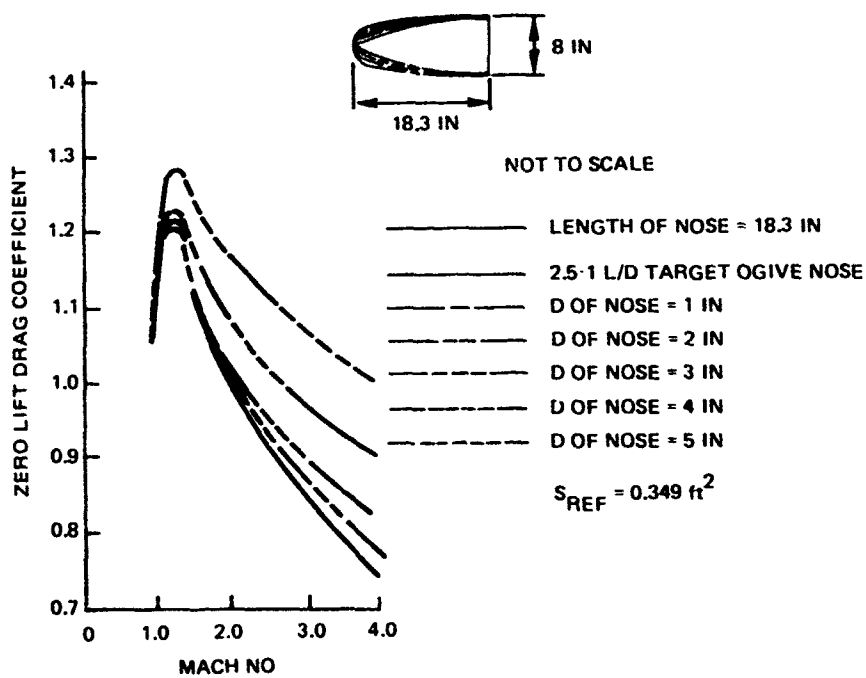
Figures 2A and 2B present the tabular data in the drag profiles. Included also in figure 2A is a drag profile for a 5-inch-diameter hemisphere on a tangent ogive with an L/D of 4.0:1; that is, the length is the full 36-inch section. As seen from this figure, a few percent decrease in drag is obtained by tapering the nose section an added 18 inches.

The hemi-ogive offers an increase in performance over the full hemisphere, but suffers in that a 10 - 15% penalty in drag is paid in comparison to more optimum drag-reducing nose shapes. In addition, the miniaturization of sensor components to fit into the small hemispherical nose lays stringent requirements upon the sensor. The sensor aperture is severely limited and does not easily lend itself to a multiguide sensor application.

²USAF Stability and Control DATCOM, vol 2, DE Ellison, September 1970



A. VARYING NOSE FINENESS RATIO



B. CONSTANT FINENESS RATIO

Figure 2. Effect of nose bluntness on 2.5:1 L/D tangent ogive nose zero lift drag coefficient.

An alternate radome shape, the power series, is attractive from the drag standpoint. The power series radome is shown in figure 3. Wind tunnel data have been taken for various power series nose shapes. Wind tunnel data comparing a tangent ogive and a hemi-ogive are presented in figure 4. The mathematical radome profile is shown in figure 5. The configuration shown is a 2.5:1 L/D ratio, 0.5 power series radome. From a mathematical viewpoint, the radome is described by a parabola:

$$y^2 = 0.8889X.$$

The nose shapes of the tangent ogive, hemi-ogive, and 0.5 power series are illustrated in figure 5 and a photograph of the three radomes is shown in figure 6. It is noted at this point that the hemisphere on the hemi-ogive has a radius of 2.3 inches. This was chosen as it represents a radome that will fit a sensor system currently under development at NELC. The sensor system is state of the art in miniaturization for a broadband, multioctave radiation sensor.

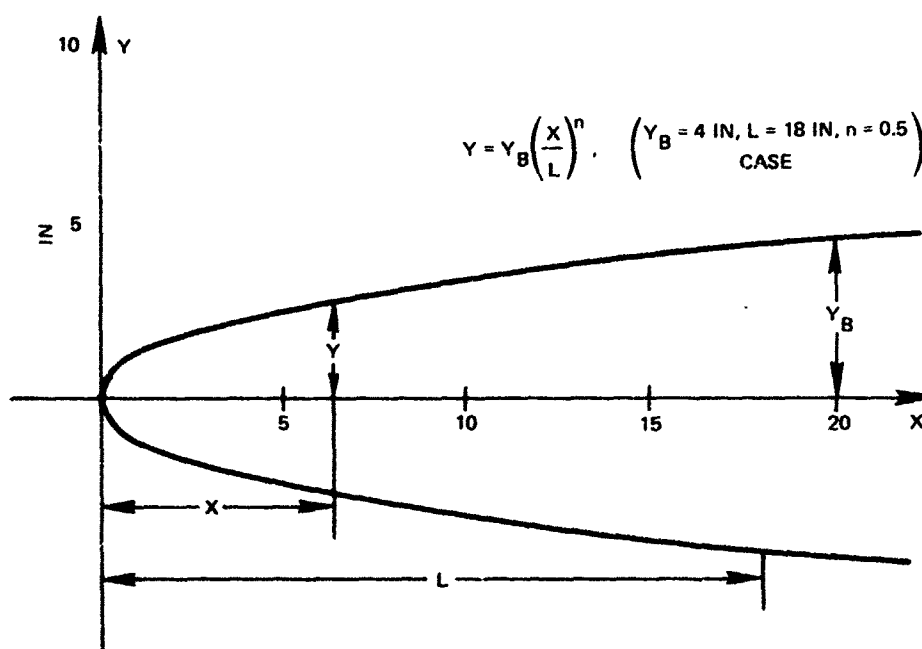


Figure 3. Power series radome profile.

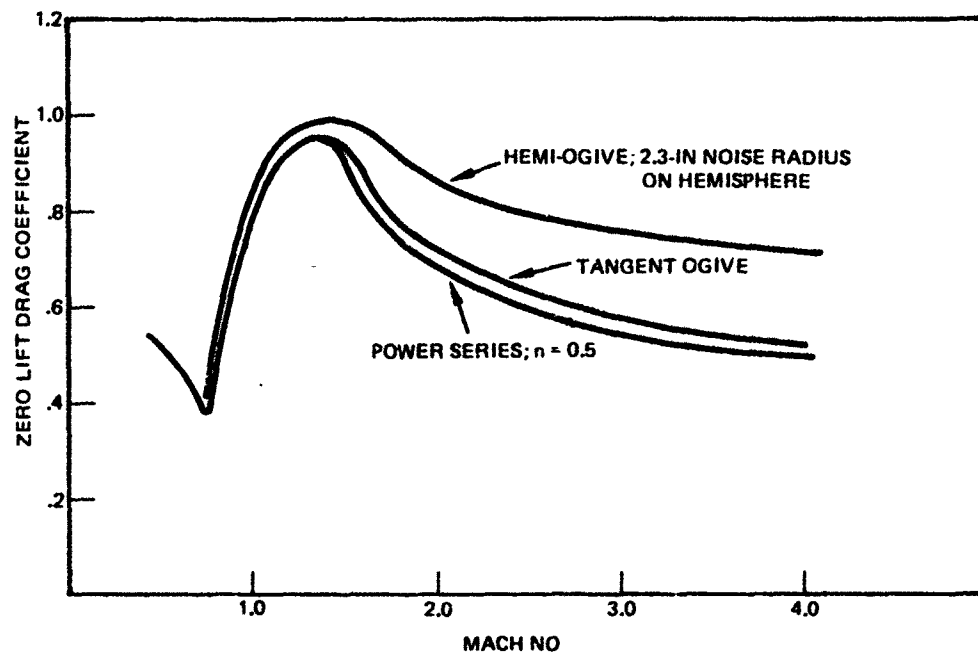


Figure 4. Zero lift drag coefficients for 2.5:1 L/D tangent ogive, hemi ogive, and power series radomes.

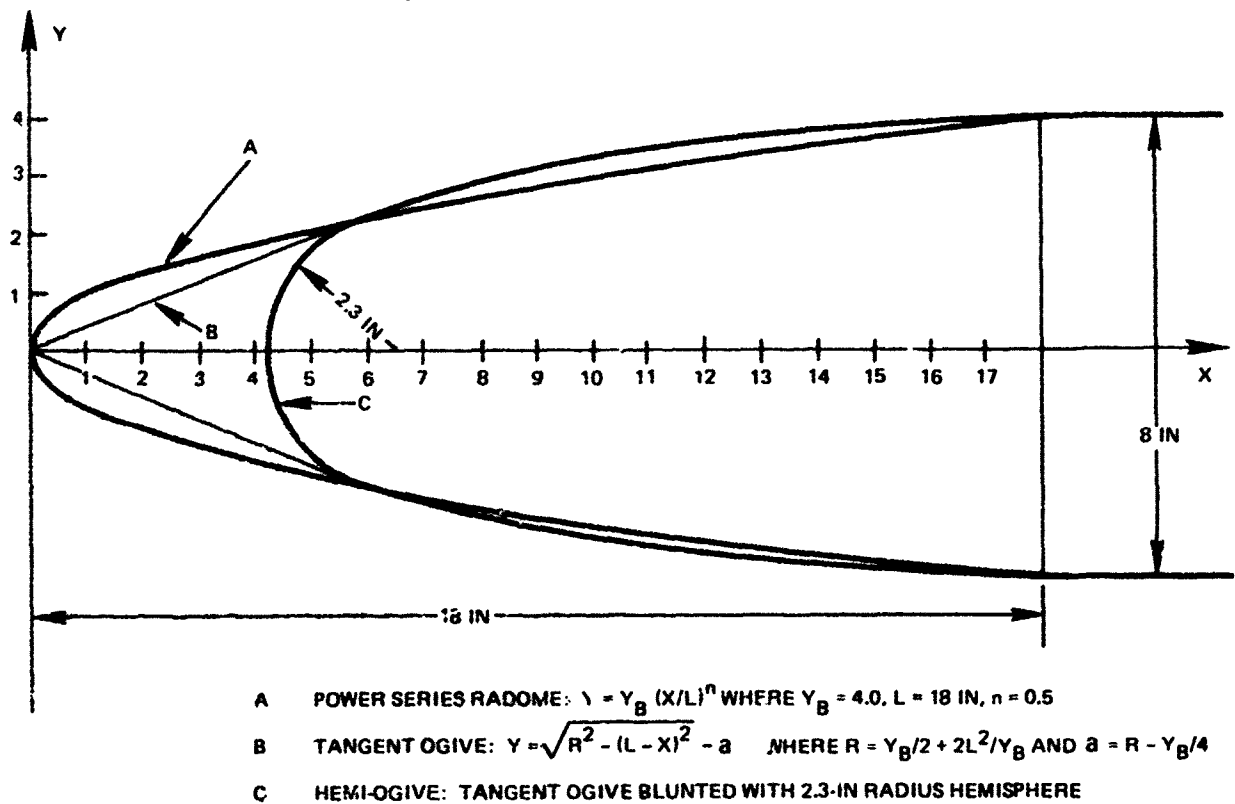


Figure 5. Comparative radome shapes.

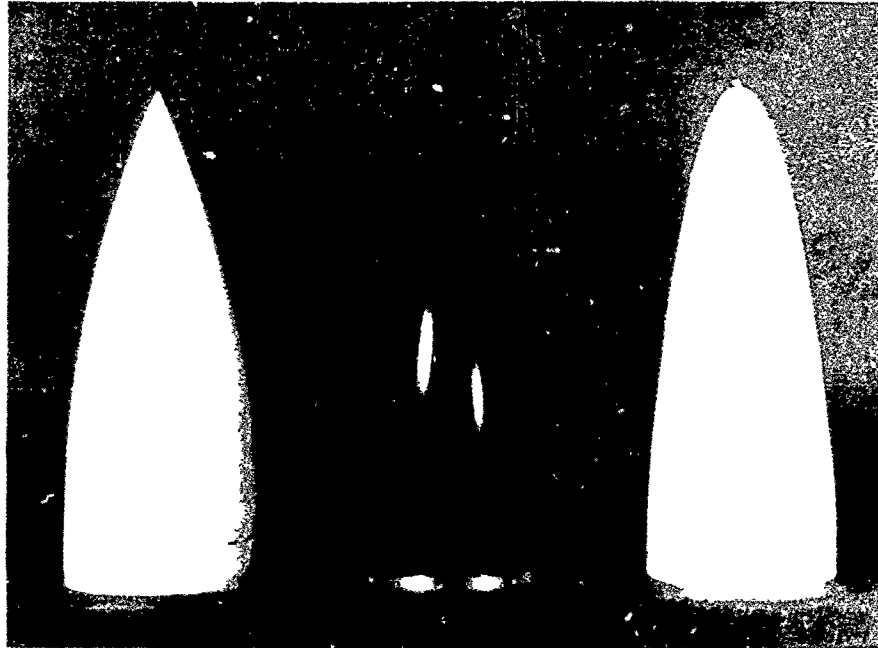


Figure 6. Comparative radomes.

STRUCTURE

Based on drag performance of the 0.5 power series, a decision was made to pursue this shape as a baseline configuration for the radome development. Areas that needed to be defined were electrical performance – both transmission and boresight error, material composition, and structural limits. The electrical properties are discussed in Electrical Performance.

The structural properties of the radome as considered here are those properties relating to resistance to rain erosion, thermal heating, and stress.

It is not the intent of this report to present an in-depth analysis of material properties relative to radome applications, but rather to present test data on materials that have qualified for radome fabrication.

In particular, the wall design that is discussed here is multi-layer construction. The electrical advantages of this kind of construction are pointed out in Electrical Performance. The material selected for the wall design is a noncharring ablative (AVCOAT 8027) bonded to a fiber glass substructure. Outside is a thin layer of low-dielectric material (impedance matching for higher transmissivity) which also provides subsonic rain erosion.

A diagram of the layered-wall construction is shown in figure 7.

The dielectric constants of the first, second, and third layers are $\epsilon_1 = 2.7$, $\epsilon_2 = 2.9$, $\epsilon_3 = 4.2$) at 10 GHz.

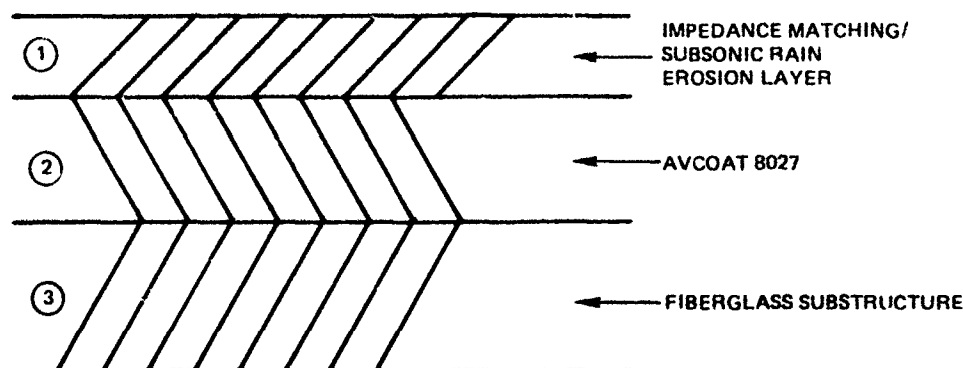


Figure 7. Layered-wall construction.

RAIN EROSION

The AVCOAT 8027 was selected for its resistance to high temperature and humidity, resistance to rain erosion, and the ability to be fabricated into shapes by inexpensive processes. A radome (hemi-ogive) was constructed (fig 6) using the layered-wall construction. The first layer was 12×10^{-3} inch thick, the second 60×10^{-3} , and the third 50×10^{-3} . This radome was tested at the Holloman Air Force Base rain erosion sled test facility.

Table 2 summarizes the results. Figure 8 shows the location and depth of craters caused by the rainfield. The depth in inches, as a function of impact angle, is presented in figure 9. The performance estimate (upper limits of rain erosion) is presented in table 3. This is a projection based on analysis of the actual data obtained for a hemi-ogive rain erosion sled test at Holloman Air Force Base.

The rain erosion test on the hemi-ogive radome proved that layered wall construction using AVCOAT 8027 as the primary rain erosion resistant material would survive a moderate-length rainfield (800 feet) at a representative velocity (2500 feet per second). The post test analysis was promising in that the projections of what the radome would survive in terms of rainfield length at various velocities is within anticipated missile operating environments. Table 4 presents additional rain erosion data for materials at high velocity (mach 4.0).

TABLE 2. SUMMARY OF RAINFIELD DATA.

Track station (rain onset)	25296
Track station (rain end)	24496
Rainfield length	800 ft
Average velocity in rainfield	2535 ft/s
Time period in rainfield	0.32 s
Mass media drop diameter	1.37 mm
Liquid water content	3.10 g/m^3

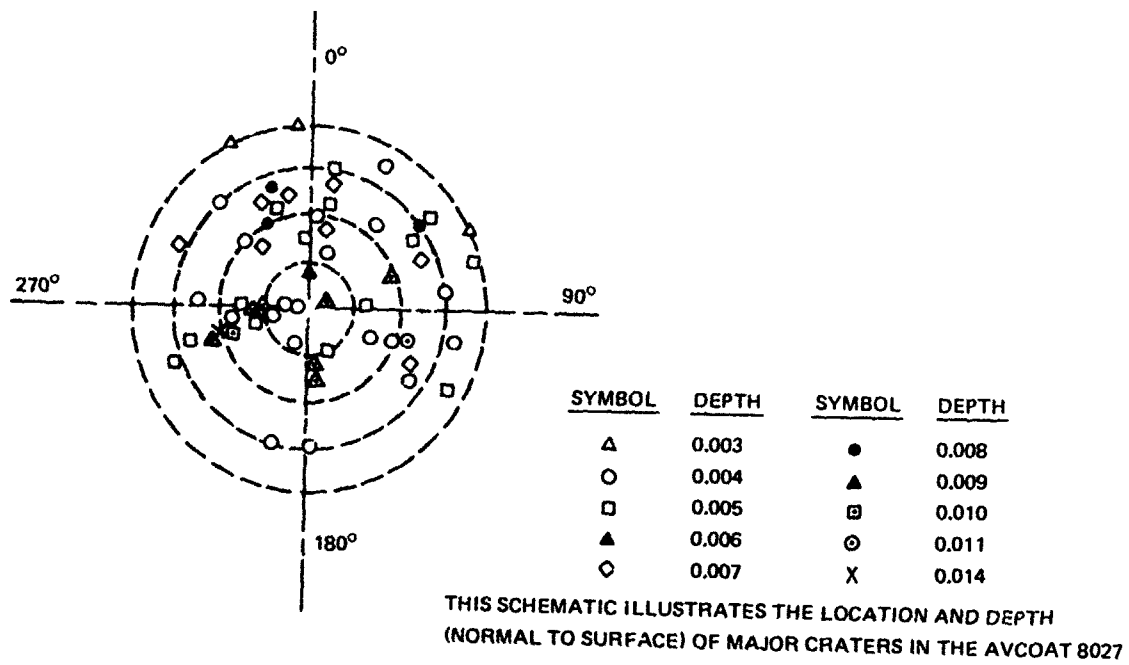


Figure 8. Rain erosion results.

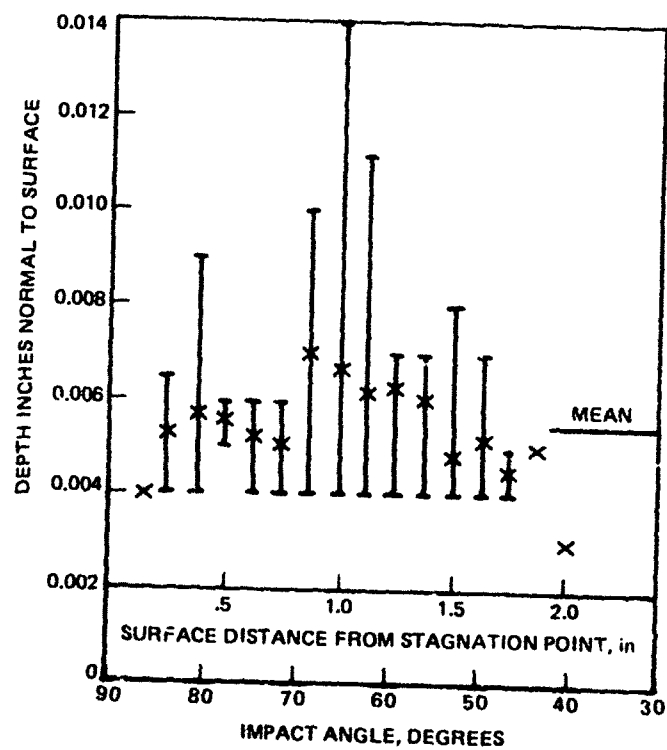


Figure 9. Rain penetration.

TABLE 3. AVCOAT 8027 PERFORMANCE ESTIMATES
(SLED TRACK RAINFIELD).

Velocity (ft/s)	Erosion Rate (in/s)	Time* (s)	Length** (ft)
2500	0.042	1.43	3600
3500	0.114	0.53	1850
4500	0.242	0.25	1125

*Allowable time in rainfield

**Rainfield length associated with allowable time

TABLE 4. AFML RAIN EROSION TESTING (SUBSCALE),
HOLLOMAN AFB TEST TRACK.

Material	Density	Test Conditions				Test Results
		Velocity	Rain rate	Rain length	Angle	
AVCOAT 8027 Castable modified epoxy (AVCO)	1.36	mach 4.0	2.64 in/h	2000 ft	45°	MDPR 0.185 -- slight surface melting
AVCOAT 8027	1.36	mach 4.0	2.64 in/h	2000 ft	60°	MDPR 0.252 -- slight surface melting
AVCOAT 9080 Silica reinforced thermoplastic (AVCO)	1.83	mach 4.0	2.64 in/h	2000 ft	45°	MDPR 0.264 -- good struc- tural integrity, no cracking or spallation
AVCOAT 9080	1.83	mach 4.0	2.64 in/h	2000 ft	60°	MDPR 0.397 -- good struc- tural integrity, no cracking or spallation
Boron nitride (carborundum) hot pressed	1.90	mach 4.0	4.6 in/h	2000 ft	60°	MDPR 1.067 -- good struc- tural integrity, no cracking or spallation
Silicon nitride** reaction sintered (Raytheon)	2.43	mach 4.0	2.64 in/h	2000 ft	45°	samples broke up severely
Silicon nitride** reaction sintered (Raytheon)	2.43	mach 4.0	2.64 in/h	2000 ft	60°	samples broke up severely

AERODYNAMIC HEATING

A radome not only must meet electrical and aerodynamic drag performance requirements, but is subjected to a stringent thermal environment – not only during tactical operation, but also while it is on the aircraft in transit. Aerodynamic heating places requirements on the thermal stress and limit properties of the radome. Figure 10 presents a relative measure of temperature changes on the radome at various stations as a function of L/D ratios.

Figure 11 presents similar relative data relating thermal stress for various L/D ratio radomes as a function of the radome axial station. It must be kept in mind that figures 10 and 11 are only qualitative in nature and present relative data.

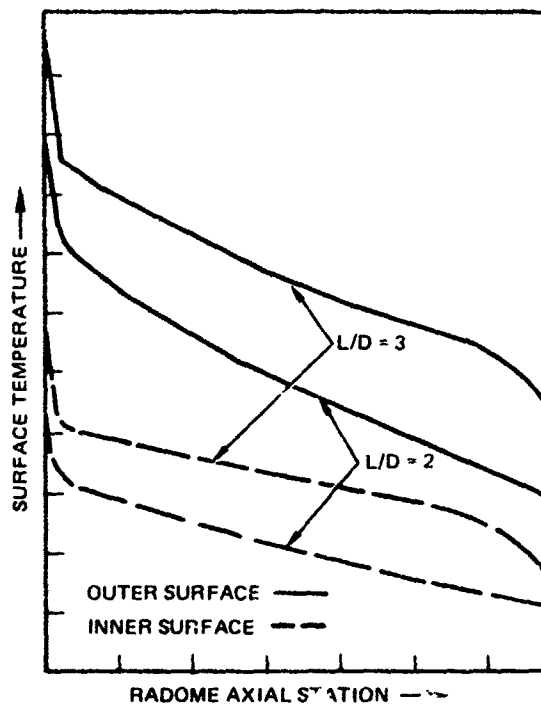


Figure 10. Maximum surface temperature vs radome axial station.

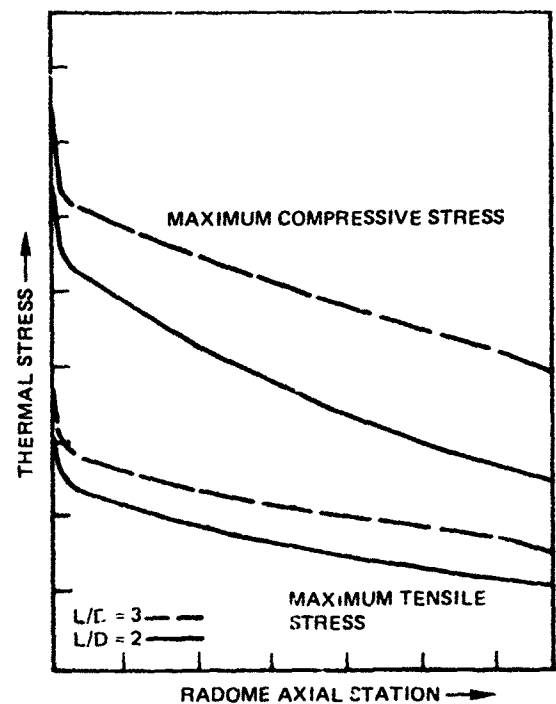


Figure 11. Maximum thermal stress vs radome axial station.

Reference 3, chapter 1, presents a brief introduction to the problems associated with aerodynamic heating. It contains numerous other references on the subject of aerodynamic heating. There are, however, some important ideas presented on these figures that are worth mentioning. The maximum surface temperature and thermal stress occur at the tip of the radome. At axial stations off the nose, the thermal stress and surface temperature drop off fairly linearly as a function of axial stations. For higher L/D ratios, higher temperature and

³"Techniques for Airborne Radome Design," Dr TE Tice, editor-in-chief (vol 1 and 2)

thermal stresses are experienced as compared to the smaller L/D ratio radomes. A technology that has surfaced to address aerodynamic heating for radomes of high-velocity missiles is the development of noncharring ablative materials. Several materials have been developed which can be used as a noncharring ablative cover. The material to be discussed here is the AVCOAT 8027 previously mentioned. Appendix C presents details on the ablative properties of AVCOAT 8027. This material is contained in reference 4.

The AVCO material has the unique property of removing heat from the radome tip through ablation. At the ablative temperature, the material decomposes at a nearly constant temperature of 1200°R to yield gaseous products. AVCO has conducted thermal tests on AVCOAT 8027 and has modeled the test results, which are shown in figure 12. This high-temperature environment occurs only at high velocities over an extended period of time in a dense air atmosphere.

Reference 3, chapter 6, presents a technique for calculating surface temperature of a radome at various distances normal to the surface. The temperature can be approximated by

$$T_x \approx T_b - (T_b - T_i) \left(1 - \frac{h' e^{\frac{-\delta x}{2a\sqrt{t}}} + h'}{h' e^{\frac{-\delta x}{2a\sqrt{t}}} + h'} \right)$$

where

T_b = boundary layer temperature, °F

T_i = ambient temperature, °F

$h' = \frac{h}{k'}$

h = heat transfer coefficient, btu per square foot-of-second

k' = thermal conductivity, °F air

δ = constant, 1.63

e = base of natural logarithmic, 2.71828

x = distance normal to surface, feet

$a = \text{diffusivity, } \left(\frac{K}{\rho_m C} \right)^{1/2}$

K = thermal conductivity of radome material

ρ_m = density of radome wall material

C = specific heat of radome wall material

t = time, seconds

For the layered radome concept the critical layer for temperature considerations is the substructure layer when glass fiber reinforced resin is used as the substructure layer. Worst-case

⁴"Tactical Missile Ablative Radomes," GW Christiansen and JP Ott, The Tenth Symposium on Electro Magnetic Windows, Georgia Institute of Technology, July 1970.

TYPICAL ELECTRICAL PROPERTIES

DIELECTRIC CONSTANT	LOSS TANGENT	FREQUENCY
3.05	0.07	0.5 GHz
2.97	0.055	3 GHz
2.85	0.05	5 GHz
2.90	0.03	10 GHz

$$Q^* = \frac{\frac{q_{cw}}{h_s} (h_s - h_w)}{\rho \dot{s}} = H_d + C_p (T_a - T_o) + \eta (h_s - h_w)$$

AVCO MODEL 500 AND 10 MEGAWATT PLASMA AND ABLATION DATA ON AVCOAT 8027

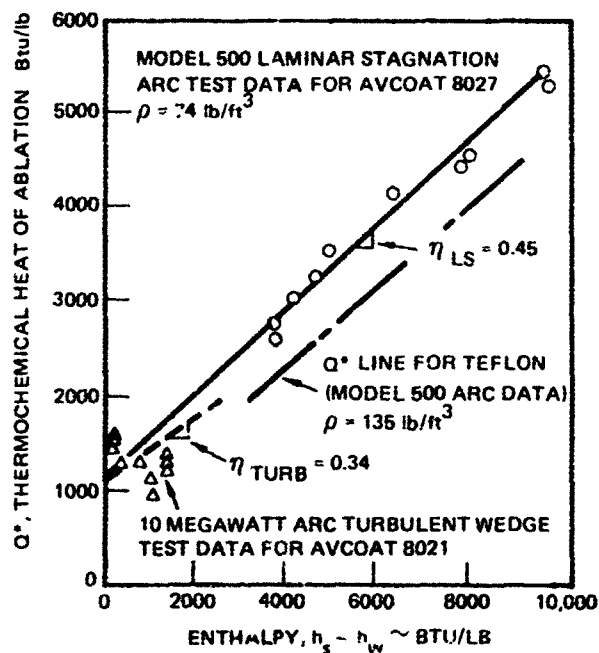


Figure 12. Summary data on AVCO 8027.

conditions for typical missiles would be a 60-second flight at low altitudes (5000 feet) at average velocity of mach 2.5. Under these conditions the following example calculates the surface temperature of the fiber glass substructure after penetrating the outside noncharring ablative layer.

$$K = 0.00002778 \frac{\text{btu-ft}}{\text{s-ft}^2-\text{°F}}$$

$$\ell_m = 0.74 \text{ pcf}$$

$$C = 0.41 \text{ btu/lb-°F}$$

$$a = \left(\frac{K}{\ell_m C} \right)^{1/2} = 9.56882 \times 10^{-4}$$

$$t = 60 \text{ s}$$

$$\delta = 1.63$$

$$\frac{\delta}{2a\sqrt{t}} = 1.09957 \times 10^2$$

$$h' = \frac{0.04}{7.5 \times 10^{-6}} = 5.333 \times 10^3$$

$$x = 0.005'' = 4.16667 \times 10^{-3} \text{ ft}$$

$$T_b = 600^\circ\text{F}$$

$$T_i = 80^\circ\text{F (assumes the missile is being carried at mach 0.8 prior to launch)}$$

$$\begin{aligned} T_x &\approx 600 - (600-80) \left(1 - \frac{5.333 \times 10^3 e^{-1.09957 \times 10^2 x}}{1.09957 \times 10^2 + 5.333 \times 10^3} \right) \\ &= 600 - (520) \left(1 - \frac{3.37307 \times 10^3}{5.44329 \times 10^3} \right) \\ &= 600 - (520) (0.380326) \\ &= 402.23^\circ\text{F} \end{aligned}$$

The surface temperature of the substructure reaches approximately 400°F at the end of the 60-second flight. The time required for the entire substructure to reach the ambient stagnation temperature (600°F) is beyond the flight time of the missile.

The thermal stress associated with the high-temperature environment was only highlighted from a qualitative viewpoint. Both the thermal stress and surface temperature aspects of the layered radome concept must be considered in more depth. It is only the intent of this report to point out relative and quantitative aspects of the thermal heating problems associated with radome design. Physical testing is required to verify these initial temperature calculations and quantify the thermal stress properties.

ELECTRICAL PERFORMANCE

Two major areas associated with radome electrical performance were evaluated – transmissivity and boresight error. Both areas were evaluated by use of mathematical models on the digital computer. Both transmissivity and boresight error are functions of many variables; therefore, a parametric analysis approach was used for maximizing performance in both areas. A true maximum performance both in maximizing transmission and in minimizing boresight error was not obtained with the parametric analysis approach. True maximum performance would have required generating an infinite volume of data. As this was not possible, trends in the data were evaluated to establish those parametric values that yielded the best radome performance. Parametric data were obtained by holding all parameters constant except one (other than frequency); as this one parameter took on different values, the performance was analyzed over a frequency band. For most of the analysis, the frequency band over which performance was analyzed was 1.0 to 24.0 GHz (roughly 4-1/2 octaves).

The primary objective was to find a wall construction that would minimize transmission losses and minimize the boresight error as a function of look angle for the power series shape ($n = 0.5$) power series radome described in the previous section. The layered wall concept was adopted as the technique for radome construction. The primary mode of guidance for the missile using this radome is passive radiation sensing. The transmission requirements for a radome on a passive radiation sensing missile are less stringent as compared to the requirements for an active or semiactive radiation sensing missile for equal range performance and moderate power transmitter capabilities. However, it will be pointed out later in this section that radome losses in active and semiactive sensors can be tolerated provided that sufficient transmitter power and signal processing gain are available. This is especially true for a multisensor guidance system in which the terminal phase is active. The passive sensor operates on much, much higher signal-to-noise ratios as compared to the active or semiactive radiation sensors. Active and semiactive systems have very low signals to work with. For the active or semiactive systems, if maximum range is a design goal, then the radome must pass at least 90% of the incident energy. The passive sensor, however, can operate with a radome that has up to 50% transmission losses.

A multimode guidance sensor, one which uses a passive sensor for launch and mid-course guidance and an active sensor for terminal guidance, would require the terminal range requirements to be on the order of a few nautical miles. The passive sensor would deliver the missile to the terminal basket for the final guidance phase. This would be within operating ranges such that radome losses would not degrade terminal range performance.

Some examples illustrating this fact are presented in the following paragraphs

TRANSMISSIVITY

The major parameters of which the radome rf energy is a function are:

- Frequency
- Wall construction
- Incident angle
- Polarization

The parameters that the designer has little control over are the incident angles, frequencies, and impinging energy polarizations. That leaves wall construction as the variable parameter. The wall construction encompasses the number of layers, dielectric constant of each layer, and layer thickness. The technique that was used to achieve the broadband coverage was an impedance matching technique. The outside is a thin, low-dielectric layer. Succeeding layers have dielectric constants of increasing value. This is analogous to a transmission line, as shown in figure 13.

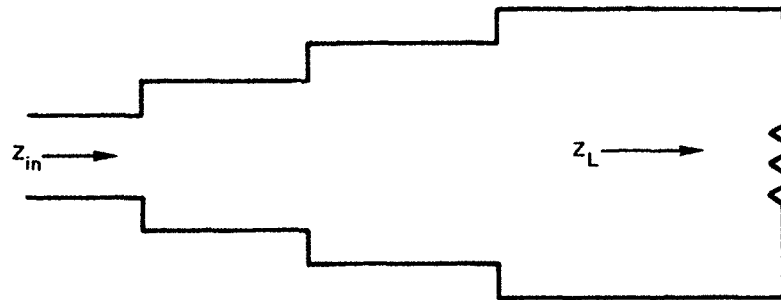
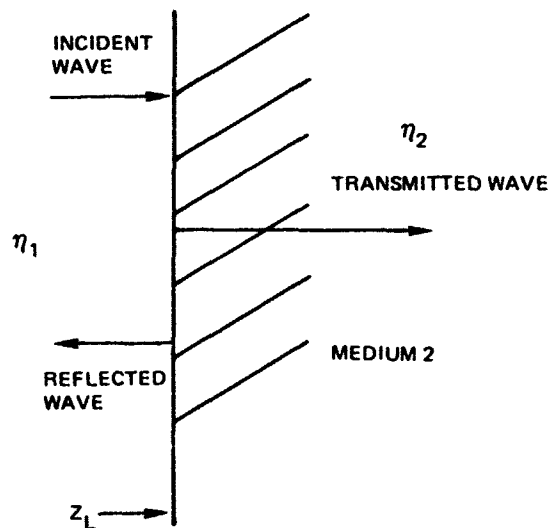


Figure 13. Multistage impedance matching transmission line transformer.

A multistage impedance transformer is used to minimize the reflections. This idea (impedance matching) can be examined for a single-boundary-layer example. Consider the single boundary layer in the following drawing:



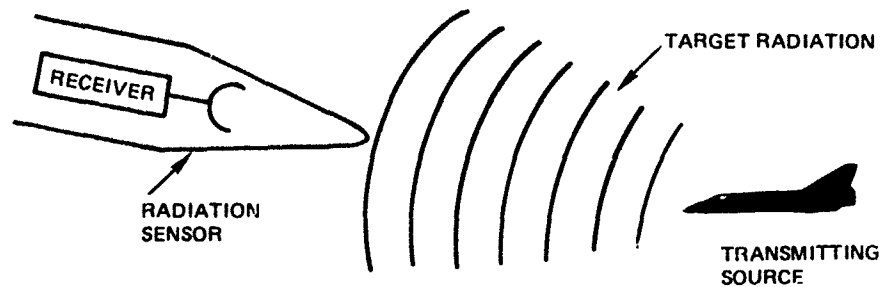
The reflection coefficient is defined as:

$$\rho = \frac{Z_L - \eta_1}{Z_L + \eta_1}$$

It is seen that for $Z_L = \eta_1$ there are no reflections; ie, all the energy is transmitted. Equivalently, since $\eta_1 = \mu/\epsilon_1$ and $Z_L = \mu/\epsilon_2$ when $\epsilon_1 = \epsilon_2$ or the dielectric constants of the two media are equal, there is no reflection at the boundary. The reflections are large when Z_L is small compared to η_1 or is very large compared to η_1 or is purely imaginary.

PASSIVE RADIATION SENSOR POWER REQUIREMENT

A passive radiation sensor is one in which only radiation being emitted from a remote source is detected. This is illustrated below.



The power received at the radiation sensor (P_r) is given by

$$P_r = \left(\frac{\lambda}{4\pi R} \right)^2 G_t G_r P_t$$

or

$$R = \left(\frac{G_t G_r P_t \lambda^2 L}{P_r (4\pi)^2} \right)^{1/2}, \text{ for } L < 1$$

where

R is range from transmitter to receiver

G_t is gain of transmitting antenna

G_r is gain of receiver

P_t is transmitter power

L is sum of loss

As an example, let the minimum power level for signal track be -70 dBm; ie, $P_{rm} = -70$ dBm, or equivalently 1×10^{-10} watt. Also, let the transmitter power be 1 kW, or 30 dBW, at a

frequency of 10 GHz. Assume the transmitter antenna has 0-dB gain, or is omnidirectional. Assume the receiver has an antenna with 10-dB gain, or equivalently a gain of 10, and there are no losses. With the above assumptions

$$R = \left(\frac{1 \times 10 \times 1000 (0.0009)}{1 \times 10^{-10} (157.91367)} \right)^{.5}$$

$$= 2.387 \times 10^4 \text{ metres}$$

$$= 78\,324.203\,0 \text{ feet} = 13.05 \text{ nmi.}$$

Assume now a 3-dB transmissivity loss through the radome. The range can now be calculated as

$$R = \left(\frac{1 \times 10 \times 1000 (0.0009) (.5)}{1 \times 10^{-10} (1.579\,136\,7)} \right)^{.5}$$

$$= 1.6881 \times 10^4 \text{ metres}$$

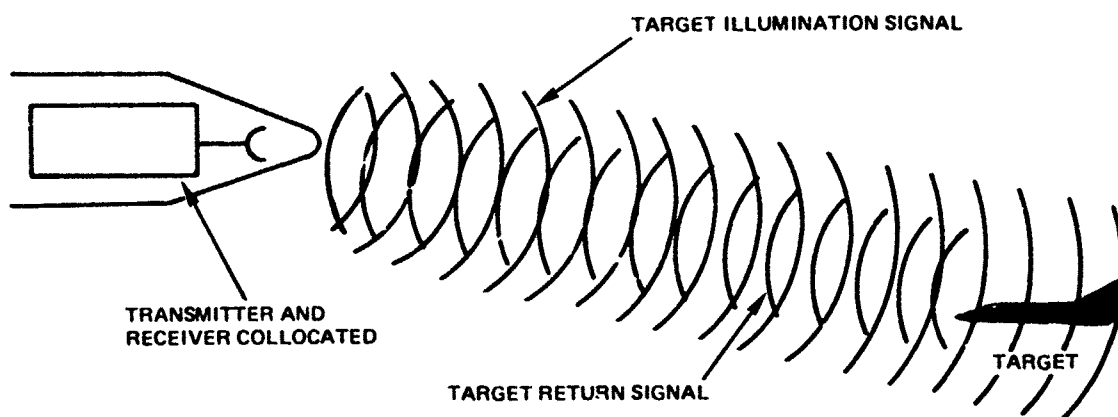
$$= 5.53836 \times 10^4 \text{ feet}$$

$$= 9.25060529 \text{ nmi}$$

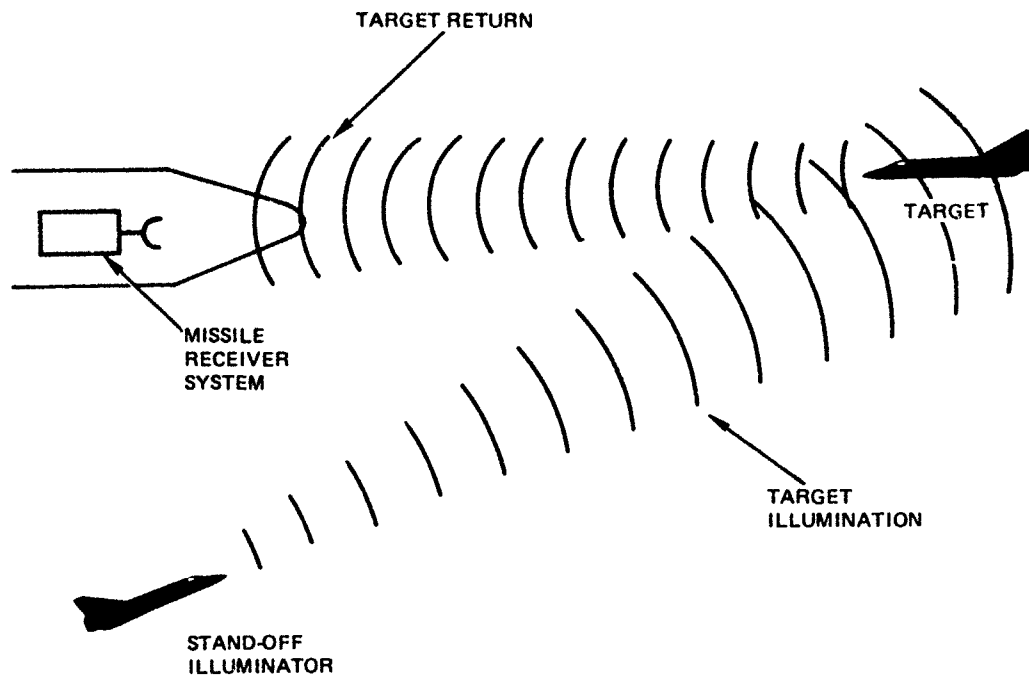
A 6-dB transmissivity loss would cut the range in half. Likewise, to double the range, an additional factor of 6 dB is required.

ACTIVE/SEMIACTIVE RADIATION SENSOR POWER REQUIREMENTS

An active guidance sensor is essentially a small radar. That is, the missile guidance system is composed of a transmitter and a receiver. The target is illuminated by the on-board (missile located) transmitter collocated with the receiver. The target illumination is detected by the radiation sensor. This guidance scheme is illustrated below.



Somewhat similar to the active guidance scheme is the semiactive system. The illuminator in this system, however, is not collocated with the missile guidance receiver but located at a stand-off range. This guidance scheme is illustrated below.



The range calculation for an active system is defined as

$$R_{\max} = \left(\frac{P_t G_t G_r \sigma \lambda^2 G_p L}{(4\pi)^3 P_{r_{\min}}} \right)^{1/4}$$

where all the parameters are those defined in Passive Radiation Sensor Power Requirement with the exception of σ and G_p . σ is defined as the radar target cross section and G_p as processing gain. To compare the operation of the active system to that of the passive system, the same values for the parameters are assumed, with the exception of G_t and σ ; ie,

$$P_t = 1000 \text{ watts}$$

$$G_t = 10$$

$$G_r = 10$$

$$\lambda = 0.03 \text{ metre}$$

$$P_{r_{\min}} = 1 \times 10^{-10} \text{ watt (minimum detectable power)}$$

$$\sigma = 10 \text{ square metres}$$

$$L = 0 \text{ dB} = 1$$

$$G_p = 0 \text{ dB} = 1$$

$$\begin{aligned} R_{\max} &= \left(\frac{1000 \times 10 \times 10 \times 10 (0.0009)}{(4\pi)^3 1 \times 10^{-10}} \right)^{1/4} \\ &= 259.509 \text{ metres} \\ &= 851.409 \text{ feet} \\ &= 0.141902 \text{ nmi} \end{aligned}$$

If an equivalent range is required to that of the passive system, the processing gain must be increased. The value of the processing gain to yield an equivalent range can be calculated as

$$\begin{aligned} 2.387 \times 10^4 \text{ metres} &= \left(\frac{1000 \times 10 \times 10 \times 10 (0.0009) (G_p)}{(4\pi)^3 1 \times 10^{-10}} \right)^{1/4} \\ G_p &= \frac{(2.387 \times 10^4)^4 (4\pi)^3 1 \times 10^{-10}}{900} \\ G_p &= 7.15868 \times 10^7 \end{aligned}$$

This processing gain, G_p , calculated to yield equivalent operating ranges for the passive and active system, is quite large. Processing gain is obtained at the expense of processing time. Processing gain and processing time are inverse functions of each other. Therefore, bounds must be placed on the processing time which is realistic to actual system performance. The numbers used in the above example are not representative of actual active systems -- antenna gains are usually larger than 10 dB although the power for active systems is usually referred to in terms of average rather than peak power. A more practical way of describing an active system and the associated processing gain is in terms of a doppler system. Range computation for a pulse-doppler radar is given as

$$R = \left(\frac{\bar{P}_t G_t G_r \sigma \lambda^2 L_r^2}{(4\pi)^3 k T_s b(S/N)} \right)^{1/4}$$

where

\bar{P}_t is average transmit power

G_t is transmitter antenna gain

G_r is receiver antenna gain

σ is target radar cross section

L is losses other than radome

L_r is radome loss

k is Boltzmann constant

T_s is system noise temperature

b is noise bandwidth

For a matched doppler filter the noise bandwidth can be approximated as

$$b \approx \frac{1}{T_d} = \frac{1}{(N_c - 1)T},$$

where

T_d is the coherent transmit time of pulse train

N_c is number of coherently integrated pulses

T is the average interpulse period

S/N is the per pulse signal-to-noise ratio in the doppler filter

Typical values are as follows:

$$\bar{P}_t = 50 \text{ watts}$$

$$G_t = 20 \text{ dB} = 100$$

$$G_r = 20 \text{ dB} = 100$$

$$\sigma = 10 \text{ square metres}$$

$$kT_s = kT_o (\bar{F} - 1)$$

where

\bar{F} is system noise factor

T_o is reference temperature

$$\begin{aligned} kT_s \text{ typical} &= 1.38 \times 10^{-23} (290) (8) \\ &= 320 \times 10^{-20} \end{aligned}$$

$$\lambda = 0.3 \text{ metre; } F = 10 \text{ GHz}$$

Assume no losses; ie.

$$L_r = 0 \text{ dB}.$$

Also let

$$S/N = 20 \text{ dB} = 100$$

and

$$b = 100 \text{ cycles}.$$

Thus,

$$\begin{aligned}
 R &= \left(\frac{50 \times 100 \times 100 \times 10 \times 0.0009}{(4\pi)^3 \times 1.38 \times 10^{-23} (290) (10) (100) (100)} \right)^{1/4} \\
 &= 8.67614 \times 10^3 \text{ metres} \\
 &= 4.68 \text{ nmi.}
 \end{aligned}$$

Thus, for typical parameters in an active system the 4.68-nmi operating range is only a fraction of that of the passive system, and typically a passive system would be operating against an emitter with transmitting power of much more than 1 kW. To increase the operating range of the active system to that of the passive system with the 13-nmi range, the transmitter power of the active system would have to be increased by approximately 20 dB, or a factor of 100, or 5000 watts of average power. This is unrealistic, and if radome losses were added, the transmitter power requirements would be even more stringent. As a terminal sensor, however, a 3 - 4-nmi operating range would be acceptable, and radome transmission losses would not impact the overall system as severely. If losses are now considered such as

$$L_r = -3 \text{ dB} = 0.5$$

$$\begin{aligned}
 R &= \left(\frac{50 \times 100 \times 100 \times 10 \times 0.0009 \times 0.316 \times 0.5 \times 0.5}{(4\pi)^3 \times 1.38 \times 10^{-23} (290) (10) (100) (100)} \right)^{1/4} \\
 &= 6.13496 \times 10^3 \text{ metres} \\
 &= 3.31049 \text{ nmi.}
 \end{aligned}$$

It is easily seen that maximum radome transmission loss is a function of required range performance. For the example given it is conceivable that a 3-dB transmission loss can be tolerated, provided the 3-nmi operating range is the requirement. It was also assumed that a 20-dB signal-to-noise was required with a receiver with a 10-dB noise figure and a 20-dB antenna gain. These parameters may be adjusted to yield better range performance; for example, the antenna gain could be increased to 25 dB.

In comparing the radome losses of active and passive systems, it is important to remember that increased power requirements for the active system are four times as great as for the passive system to yield equivalent range performance prior to the radome losses. This is extremely important when considering a system that has already been designed and developed but does not have sufficient operating range.

In an active system the processing gain or transmitter power together must be increased by 6 dB to account for a 3-dB radome loss. In the passive system the operating range, operating against a typical transmitter, is sufficiently large that cutting the range performance by 30% (a 3-dB loss) does not degrade overall missile system performance. For most systems the sensor minimum range performance exceeds maximum aerodynamic performance. In the passive/active system the passive system would deliver the weapon to the

terminal range where range requirements could be realistically met even when transmission losses were on the order of 3 dB.

Assuming the system aspects of the problem have been resolved (range requirements for acquisition, launch, midcourse, and terminal), the next logical step is to analyze the candidate radomes and evaluate their performance to determine whether or not they will be satisfactory to meet system operating range requirements. The next section addresses this problem.

TRANSMISSIVITY DATA

Transmission data were generated for energy striking a multilayer dielectric configuration. Initially the transmission data were generated for perpendicularly polarized energy striking a nonlossy, parallel-multilayer dielectric at normal incident angles. This was done to get a relative idea of the effect of varying the thicknesses of the dielectric layers.

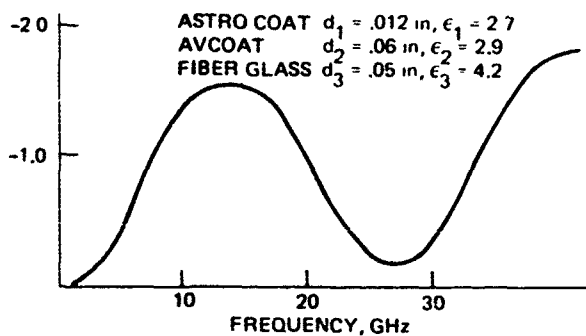
Figures 14A through 14F present the results of varying the dielectric layer thicknesses of the multilayer dielectric composite material. Figure 14A presents data on the multilayer wall construction of the hemi-ogive radome shown in figure 6. Over the 1 - 20-GHz band the maximum transmission loss was calculated to be 1.5 dB. This agreed favorably with the actual measured data shown in figure 14B.

In figure 14C the fiber glass layer thickness was cut in half. That is, the layer was reduced from 50×10^{-3} to 25×10^{-3} inch. The general shape of the transmission loss curve did not change appreciably. The loss did decrease slightly over the frequency range with a slight variation in the shape of the curve. Figures 14D-14F present similar data for changes in the individual layer thicknesses.

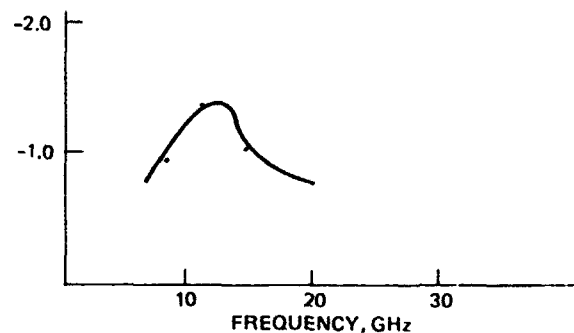
In general, as the thicknesses of the dielectric layers increased, the oscillation of transmissivity, ie, the variation of transmissivity, as a function of frequency increased. Comparison of figure 14E to figure 14F points out this oscillatory property of transmissivity as a function of frequency. It was also noted that the transmission loss did not increase over -2 dB over the variations of individual layer thicknesses.

In addition to data calculated for the normal incident energy, transmissivity data were calculated for perpendicularly polarized energy striking the multilayer composite dielectric material at various incident angles as a function of frequency. Here again the multilayers were parallel to each other. A loss tangent for each layer was also included in the calculations to predict the transmissivity properties of the layered dielectric material. Figure 15A presents data for the transmission loss as a function of incident angle versus frequency. These data were calculated for the individual layer thicknesses of $d_1 = 0.012$ inch, $d_2 = 0.04$ inch, and $d_3 = 0.025$ inch. The dielectric constants were $\epsilon_1 = 2.7$, $\epsilon_2 = 2.9$, and $\epsilon_3 = 4.2$. The loss tangents were $\tau_1 = 0.003$, $\tau_2 = 0.05$, and $\tau_3 = 0.01$.

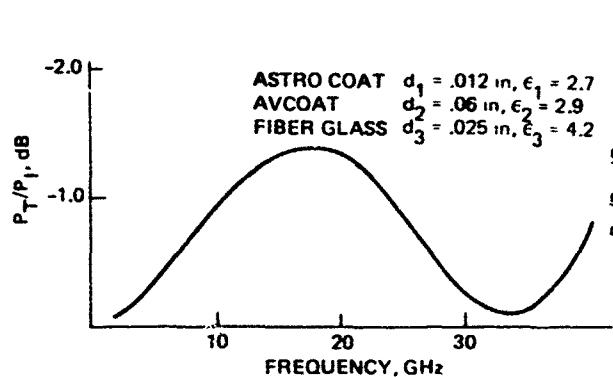
The data here follow the general theory that as the incident angle increased, the transmission loss also increased. For incident angles less than 40° , the transmission loss over the frequency band did not exceed a 3-dB loss. The data of figure 15A were for a nonlensed radome. The radome yielding the best boresight error performance was a lensed radome; therefore, an approximation of the lensed radome was modeled to generate transmissivity data. These data for a lensed radome (lens approximated by a constant increase in wall thickness) were calculated and are presented in figure 15B. This is a conservative estimate of what the transmission loss would be. The actual transmission loss would be less than is illustrated in figure 15B because of the energy focusing effect of the lens and the nonuniform wall thickness.



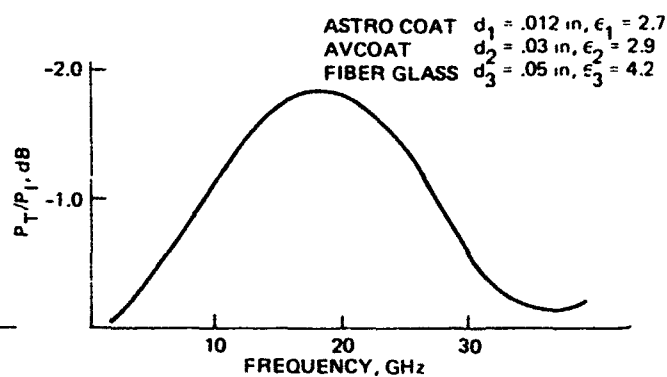
A. MULTILAYER DIELECTRIC



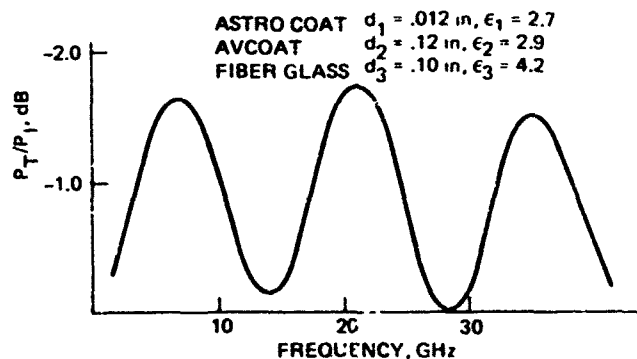
B. MEASURED



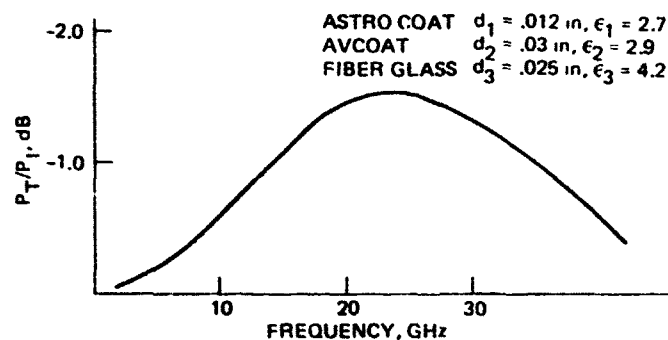
C. MULTILAYER DIELECTRIC



D. MULTILAYER DIELECTRIC



E. MULTILAYER DIELECTRIC



F. MULTILAYER DIELECTRIC

Figure 14. Transmission loss vs frequency.

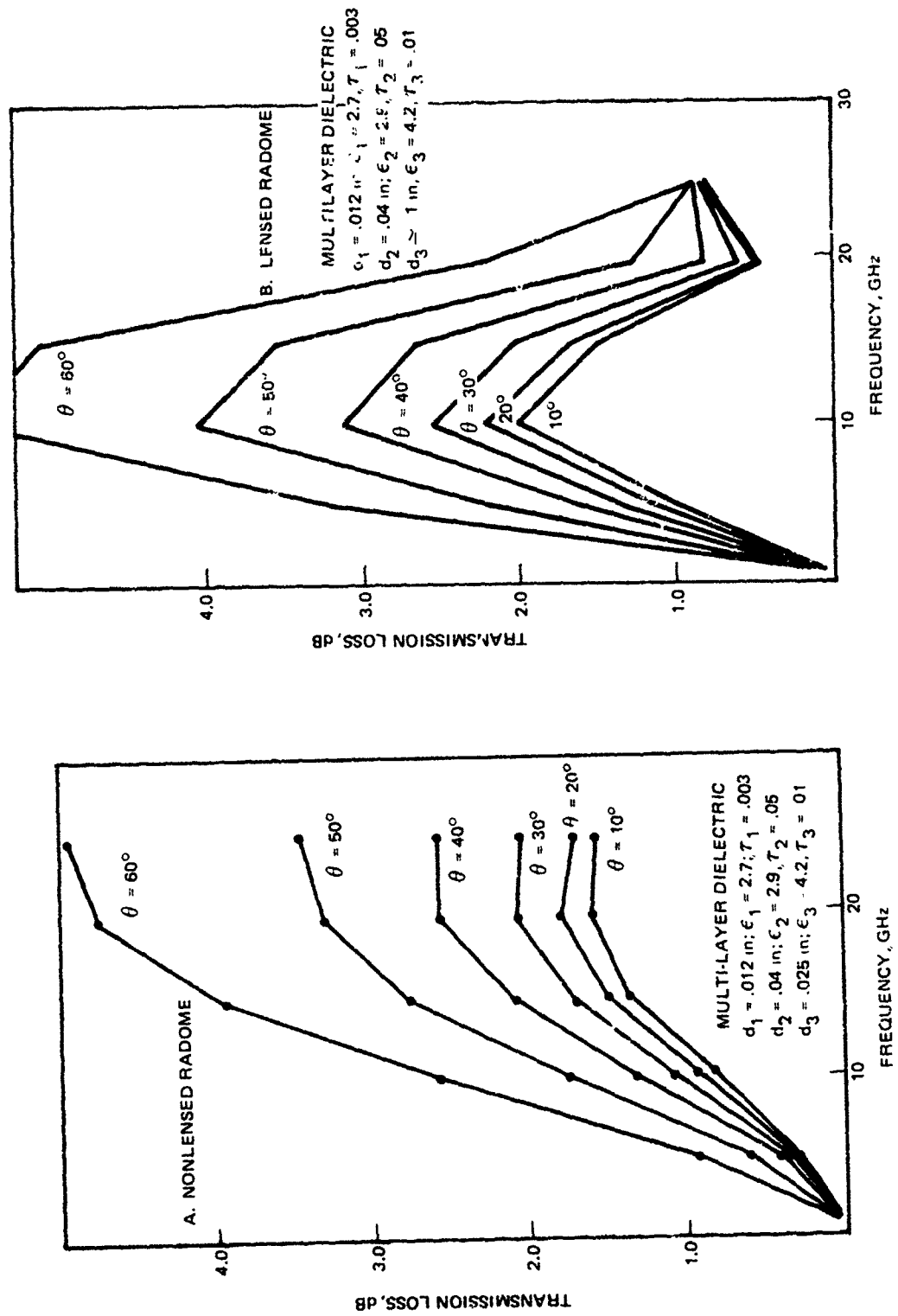


Figure 15 Transmission loss as a function of incident angle vs frequency.

BORESIGHT ERROR

Boresight error is a function of even more variables than transmissivity, including

- Antenna station
- Antenna aperture
- Nose shape
- Rf energy
 - Frequency/polarization
- Wall construction
 - Layer thicknesses and dielectric constants
- Phase compensation
 - Lens shape
 - Lens dielectric constant

As with transmissivity, the analysis of the boresight error as a function of gimbal angle was done parametrically over a range of values for each parameter. The gimbal angle is shown in figure 16. The assumption is made that the radome is perfectly symmetrical. Thus, the boresight error as a function of look angle will be an odd function. Figure 17 illustrates a typical boresight error function curve.

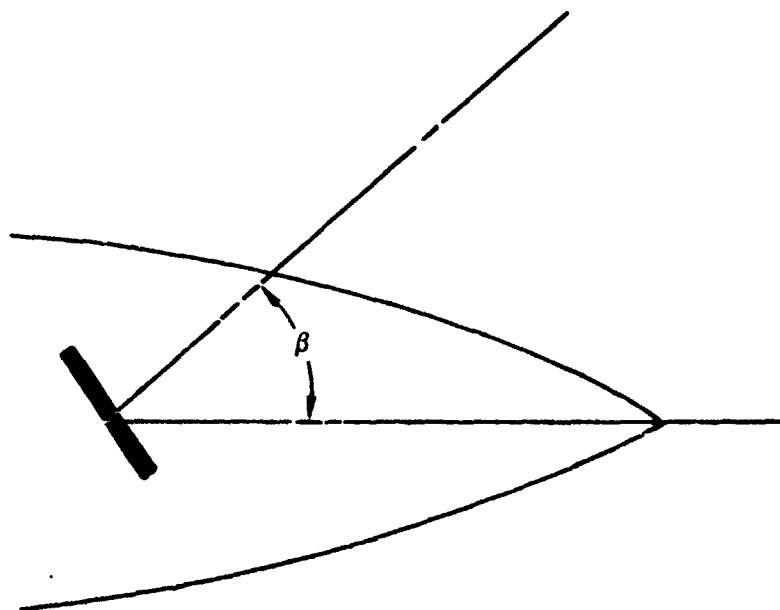


Figure 16. Look angle definition

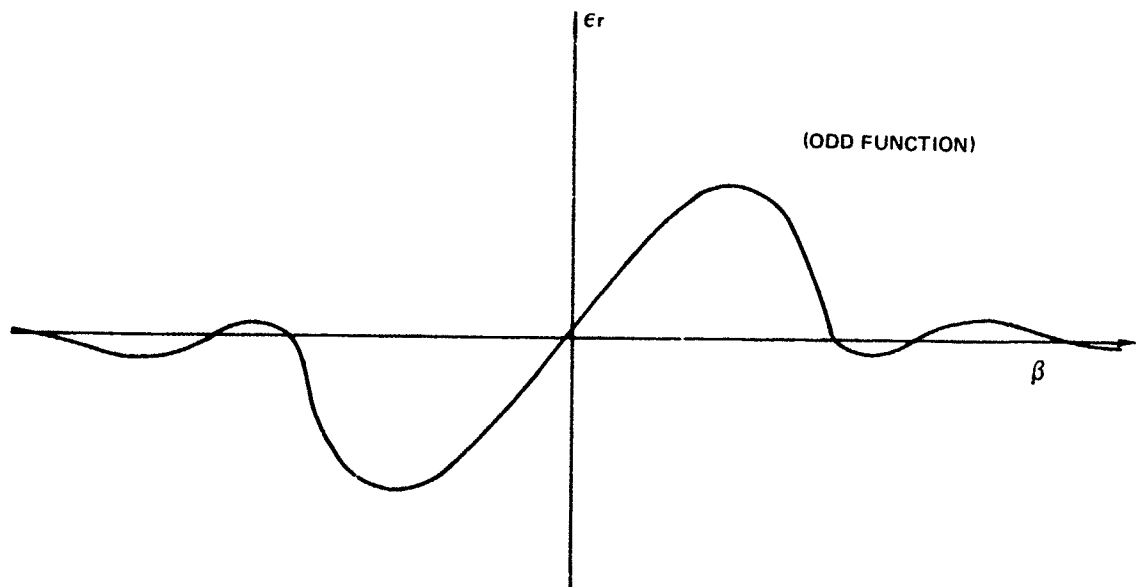


Figure 17. Example of boresight error as a function of look angle.

CAUSES OF RADOME BORESIGHT ERROR

Boresight error is caused by energy striking the radome at various incident angles. This occurs because the curvature of the radome is nonuniform. Figure 18 illustrates this principle. The incident ray that is labeled B in figure 18 strikes the radome at a much greater angle than does the incident ray labeled A; therefore, the path length through the radome wall is different for each ray and there is a phase delay or phase differential between the two rays. This phase contributed by the radome is called insertion phase. A gimbaled antenna will align itself in a manner such that the phase distribution across the antenna aperture is relatively constant or symmetrical with the antenna centerline. For an oncoming wave front such as illustrated in figure 19 an antenna aligns itself so that it is orthogonal to the direction of travel of the wave front.

The points labeled A, B, C, and D along the wave front are all in phase with each other. The antenna aligns itself to be parallel with the line intercepting the points A, B, C, and D. If, however, A, B, C, and D are not phase coherent (additive, nonuniform phase contributed by the radome) at a perpendicular to the direction of arrival, the antenna will realign itself orthogonally to an apparent direction of arrival of the oncoming wave. This is shown in figure 20.

The differential between the actual angle of arrival and the apparent angle of arrival is termed the boresight error angle (δ). It is noted in figure 18 that the higher incident angles occur farther back on the radome. It is at these higher incident angles where increased phase (insertion phase) is added to the incident energy. A technique for balancing out the insertion

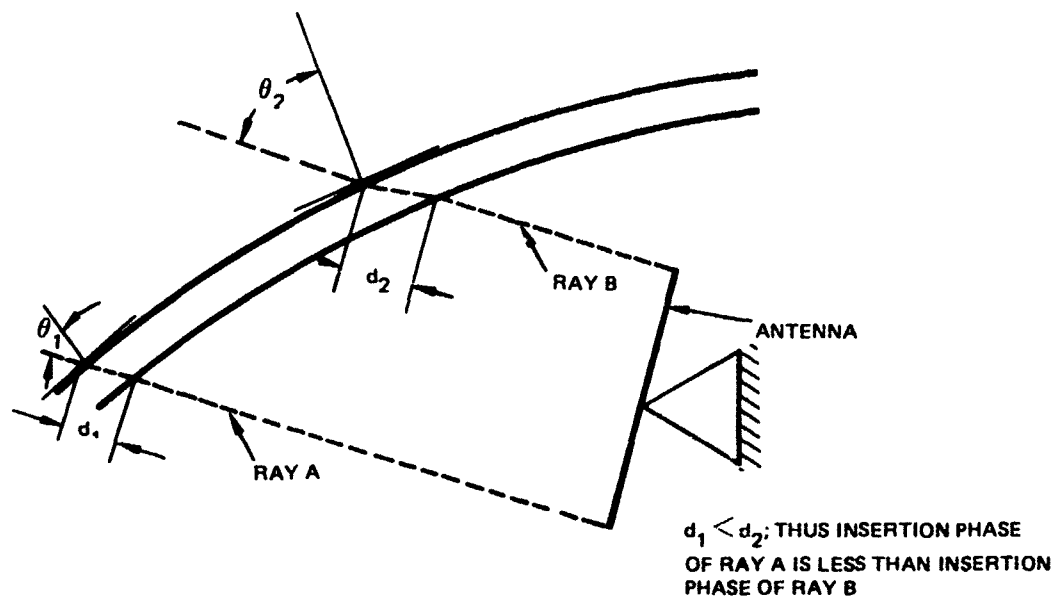


Figure 18. Radome error caused by insertion phase.

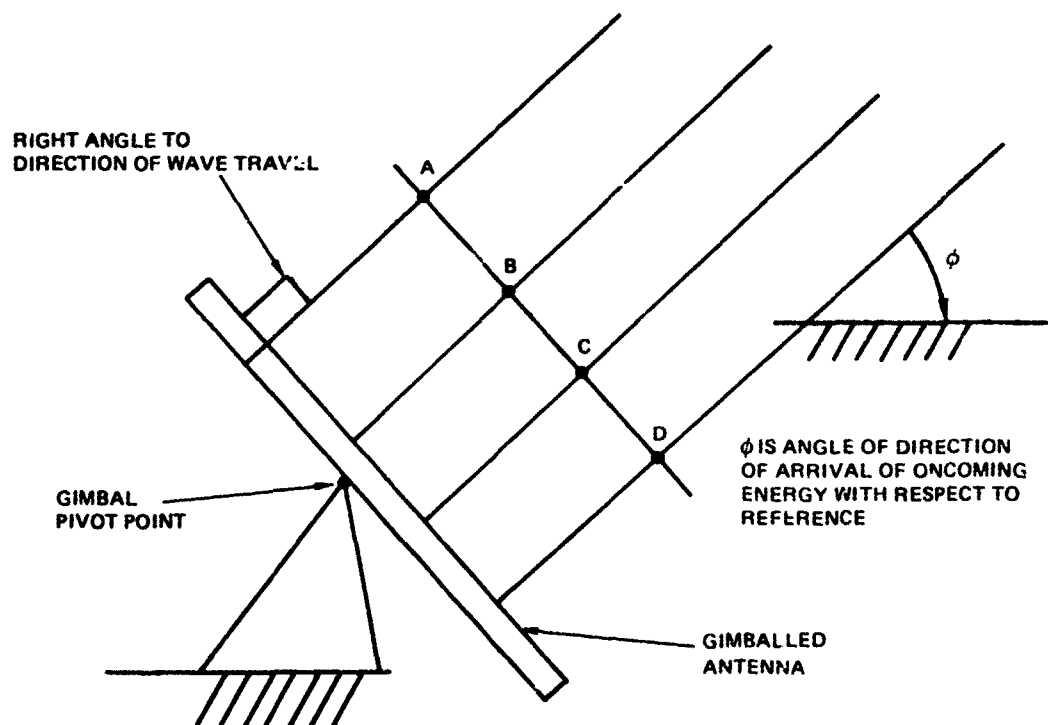


Figure 19. Signal tracking without boresight error.

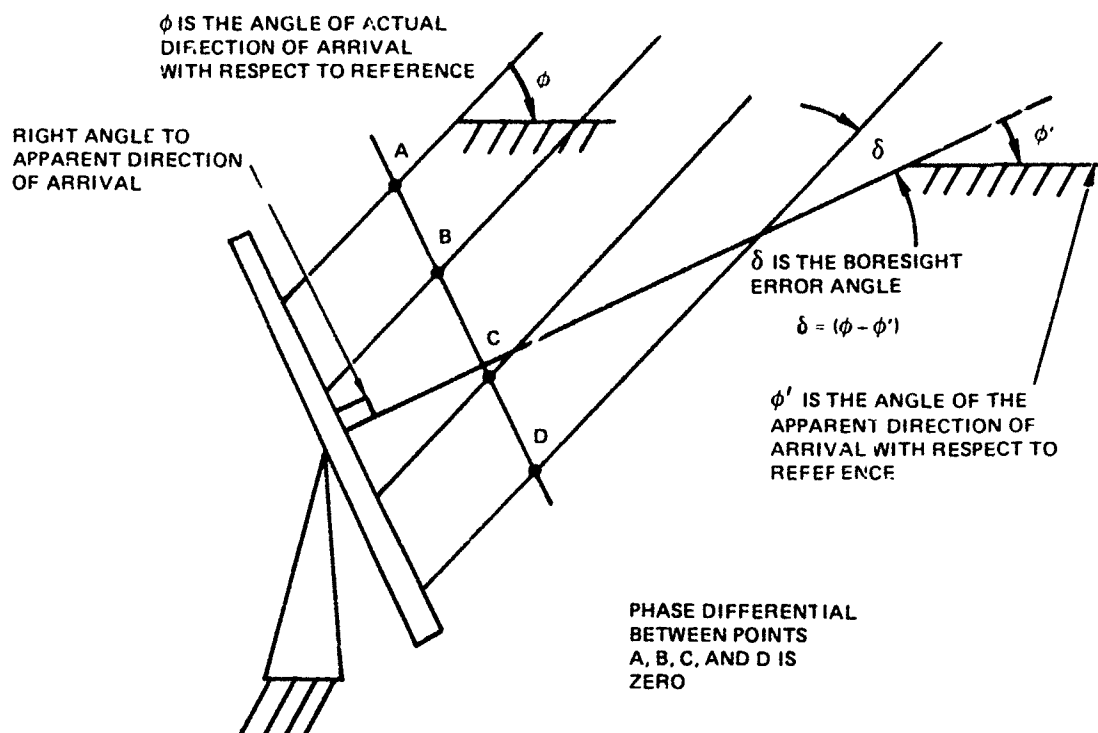


Figure 20. Signal tracking with boresight error.

phase or holding it relatively uniform or symmetrical across the antenna aperture was investigated. This insertion phase compensation technique was accomplished by integrating a lens into the radome structure. Figure 21 illustrates the procedure for a parabolic lens integrated with a power series radome. Quantitatively, what this does is add wall thickness at the lower incident angles. By referring to figure 22 it can be seen that the incident angle of the ray B, Θ_2 , is greater than that of the incident angle Θ_1 caused by ray A. By appropriately determining the lens, the lengths of the paths through the radome wall are relatively equal in length, or, more appropriately, the insertion phase added by the radome to incident wave at ray A is equal to that added at ray B. Ideally, what the phase compensation must do is maintain a symmetrical phase distribution across the aperture of the antenna. Figure 23 shows an example of symmetrical phase patterns (symmetry with respect to either side of antenna from centerline) across the antenna aperture.

INTEGRATED RADOME/LENS MODEL

Having established a technique for insertion phase compensation, a mathematical model of the integrated radome/lens was developed. A signal flow chart of the computer program describing the mathematical model is presented in appendix A. The computer program utilized a ray-tracing technique to establish radome/lens performance.

At a given look angle the incident energy traveling in a direction parallel to the look angle is traced through the radome. Since the energy strikes the radome at an infinite number of different incident angles, a quantization scheme is utilized to analyze a finite number

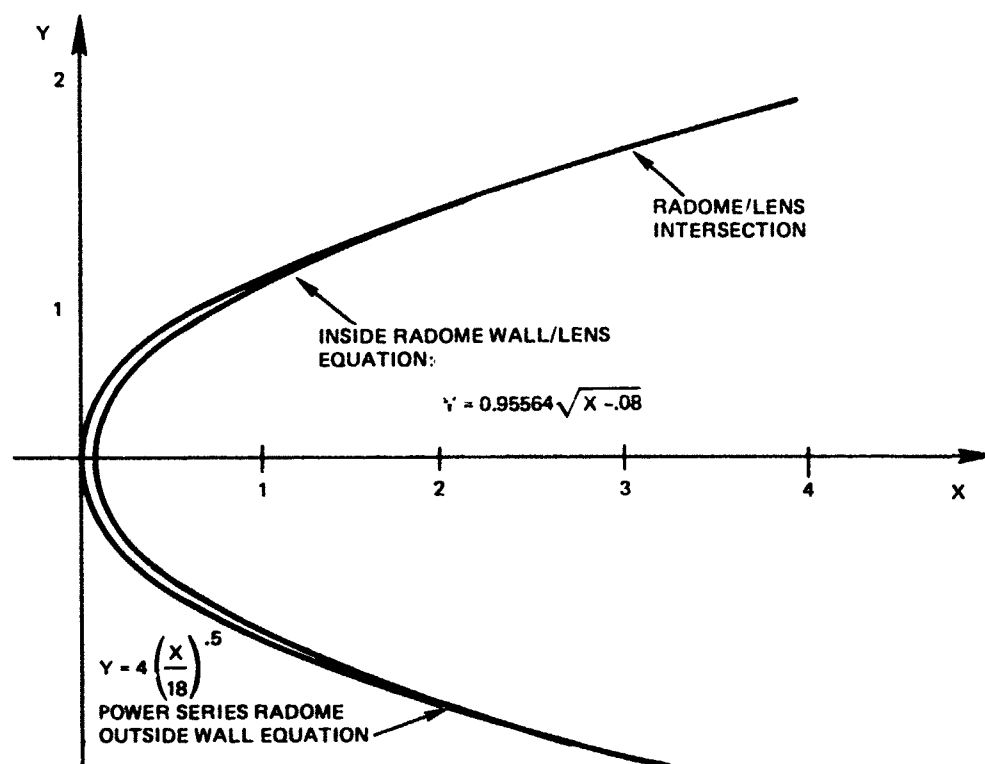


Figure 21. Power series radome with integrated parabolic lens.

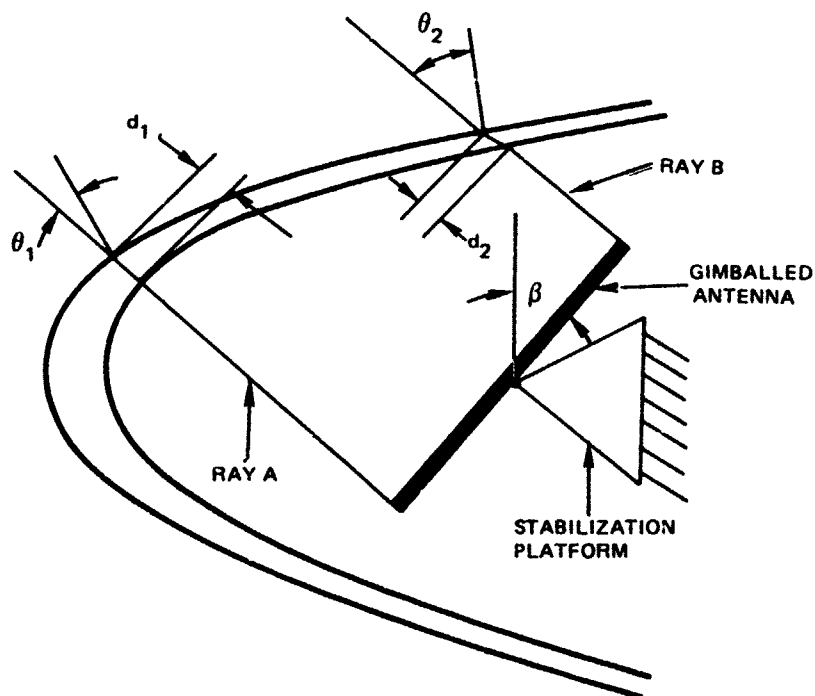


Figure 22. Radome/lens phase insertion compensation.

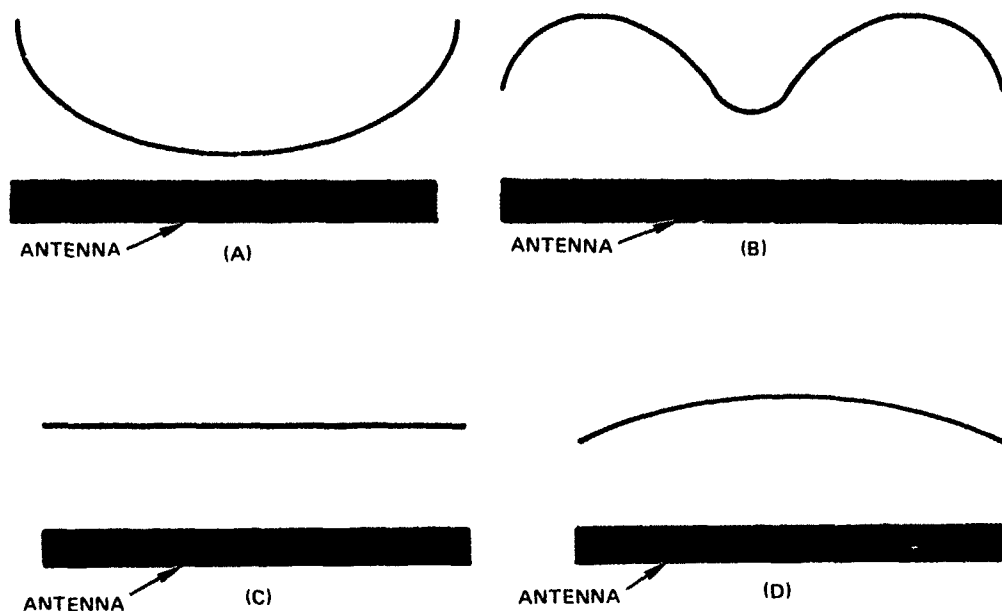


Figure 23. Examples of symmetrical phase (two dimensions) across antenna aperture.

of data points along the radome surface. Each data point is calculated by considering a single energy ray and the total wave front is made up of a finite number of incident rays or an array of data points. Each energy ray is geometrically traced through the radome and with it an associated insertion phase. An insertion phase distribution pattern is calculated across the antenna aperture. A regression technique is then used to calculate a phase tilt angle. This would be the differential refraction angle that the antenna would precess to track the apparent line of sight.

BORESIGHT ERROR DATA

Figures 24A-24C are plots of boresight error angles as a function of look angle. Figure 24A presents data at 4.0 GHz, figure 24B at 8.0 GHz, and 24C at 18 GHz. Two curves are plotted on each data sheet. These data are for the 0.5 power series radome. The antenna was placed 6 inches back from the radome nose. The antenna was a circular aperture antenna, with a diameter of 2 inches. The two curves shown on each data sheet show the uncompensated, no lens, and the compensated, integrated radome/lens, boresight error curves. It is pointed out that compensation (addition of lens) definitely reduced radome error -- in some cases by as much as a factor of 75 to 1. Figure 25 presents boresight error slope data over the 1.0 - 18.0-GHz frequency regions. From 8.0 to 18.0 GHz the boresight error slope does not exceed 0.04 degree per degree. Figures 26 through 29 present additional boresight error/boresight error slope data for alternate lenses, antenna aperture, and antenna station location. Table 5 presents the

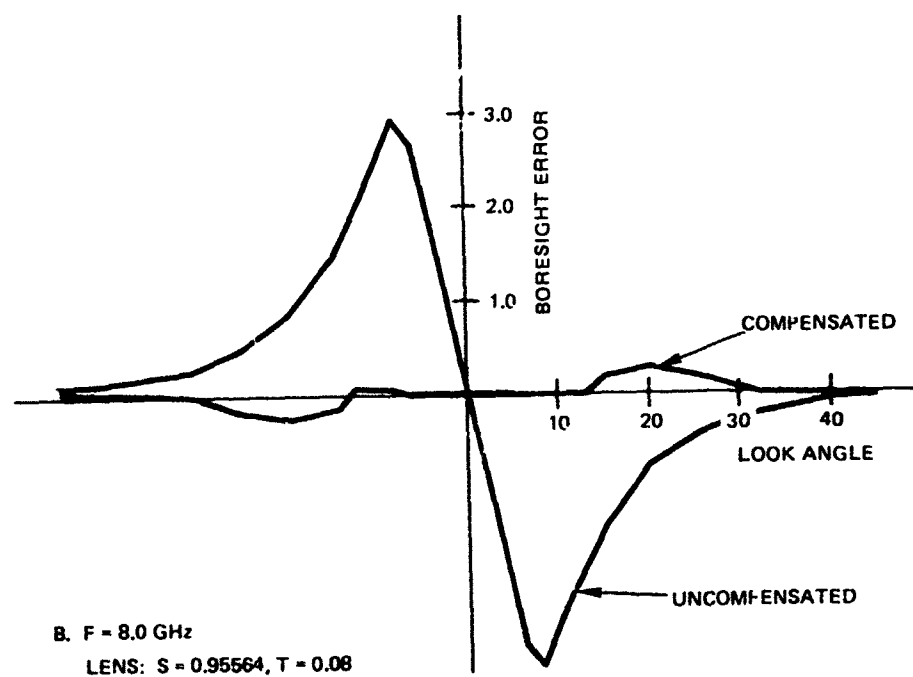
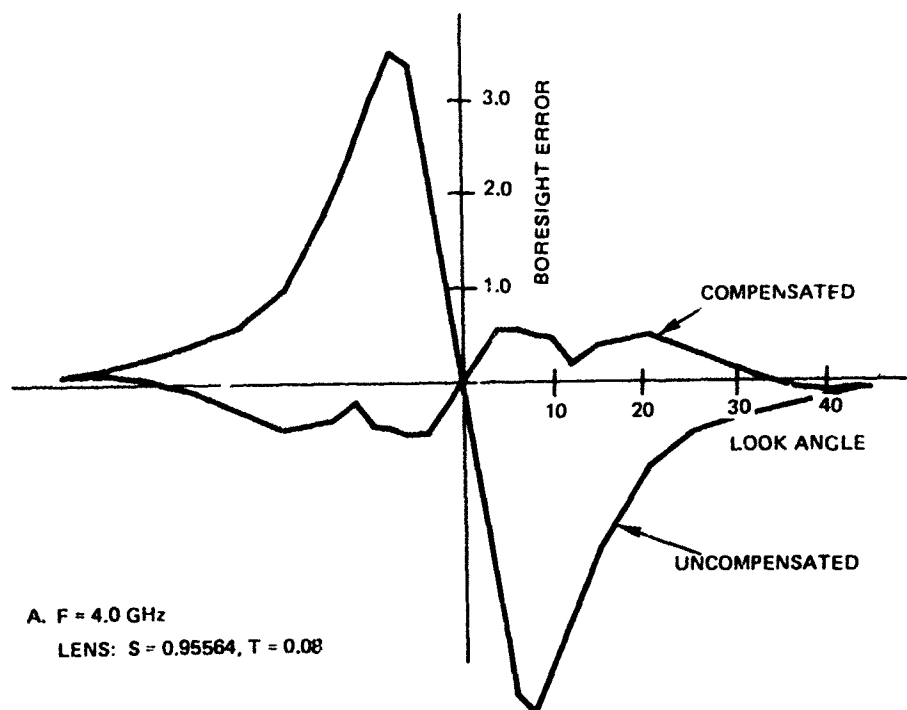


Figure 24. Boresight error data (2-in-diameter antenna at 6-in station).

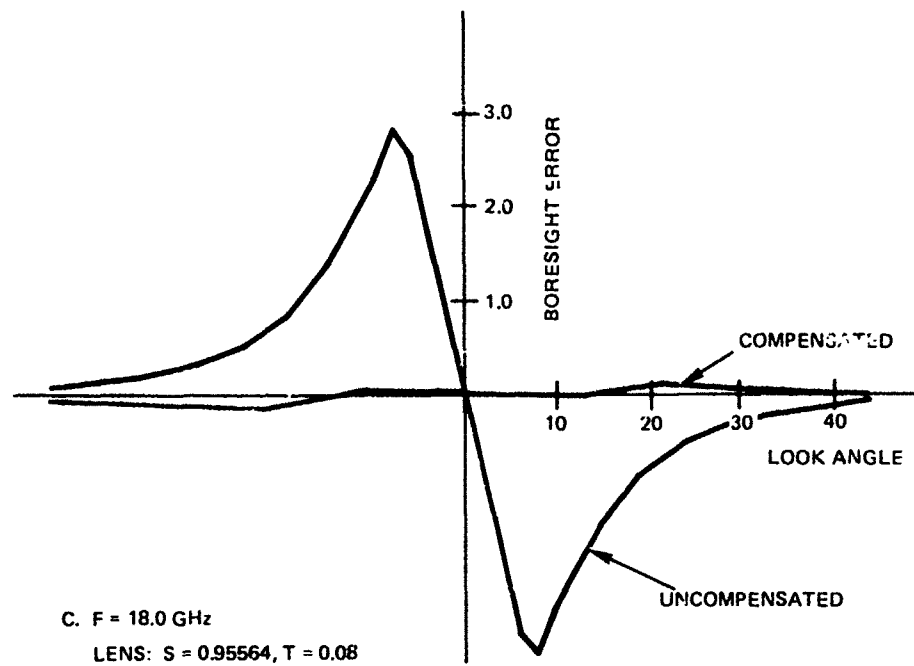


Figure 24 (Continued).

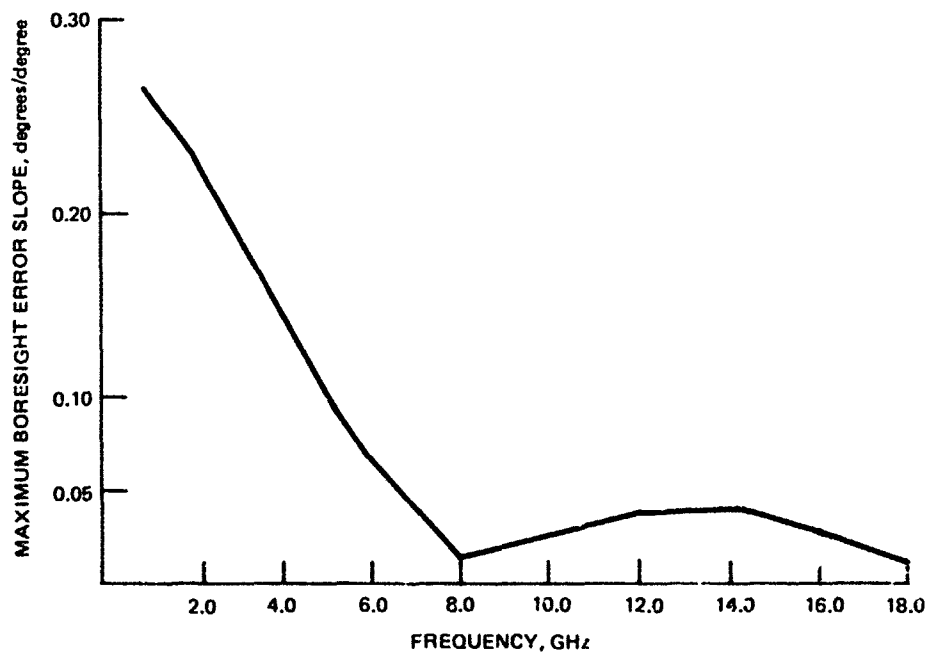


Figure 25. Boresight error slope data for a compensated radome (2-in-diameter; antenna at 6-in station).

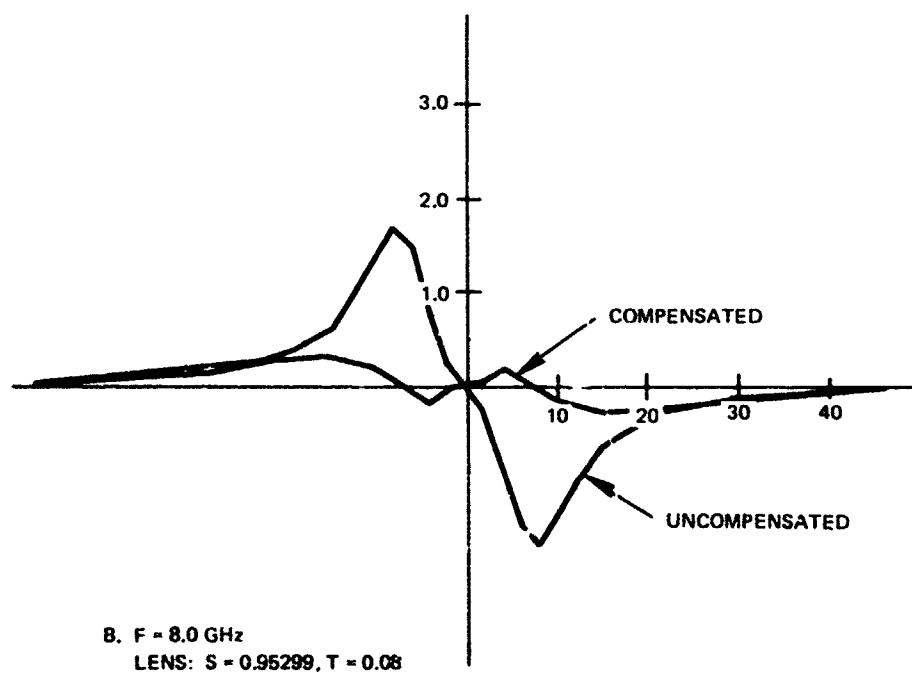
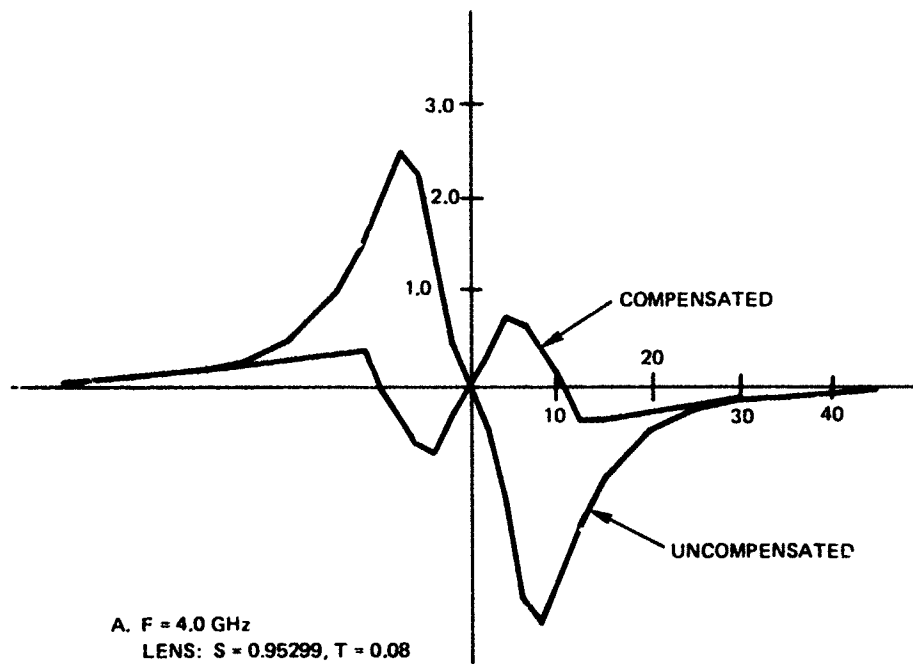


Figure 26. Boresight error data (4-in-diameter antenna at 12-in station).

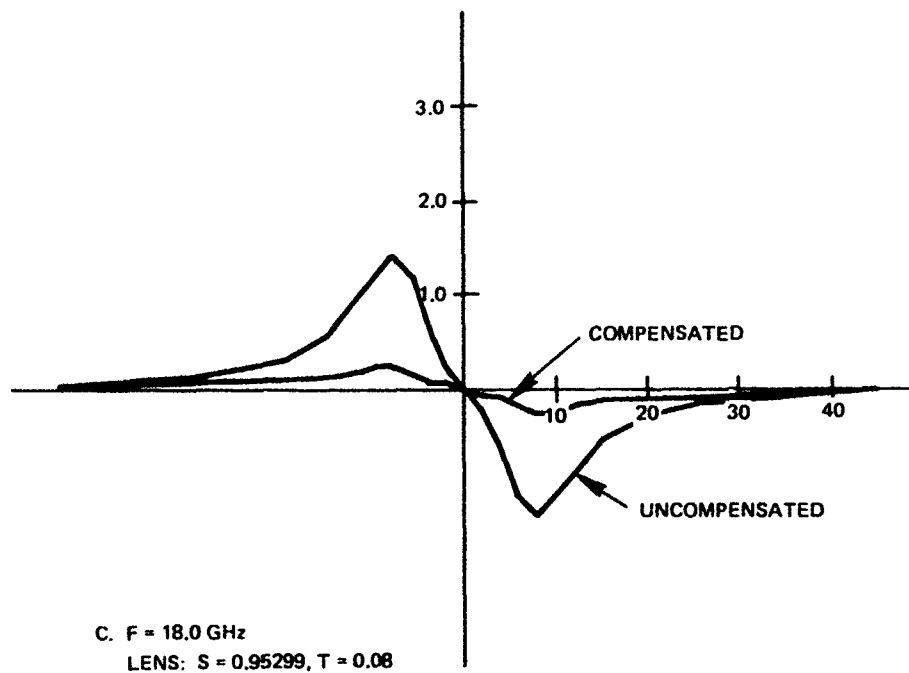


Figure 26 (Continued).

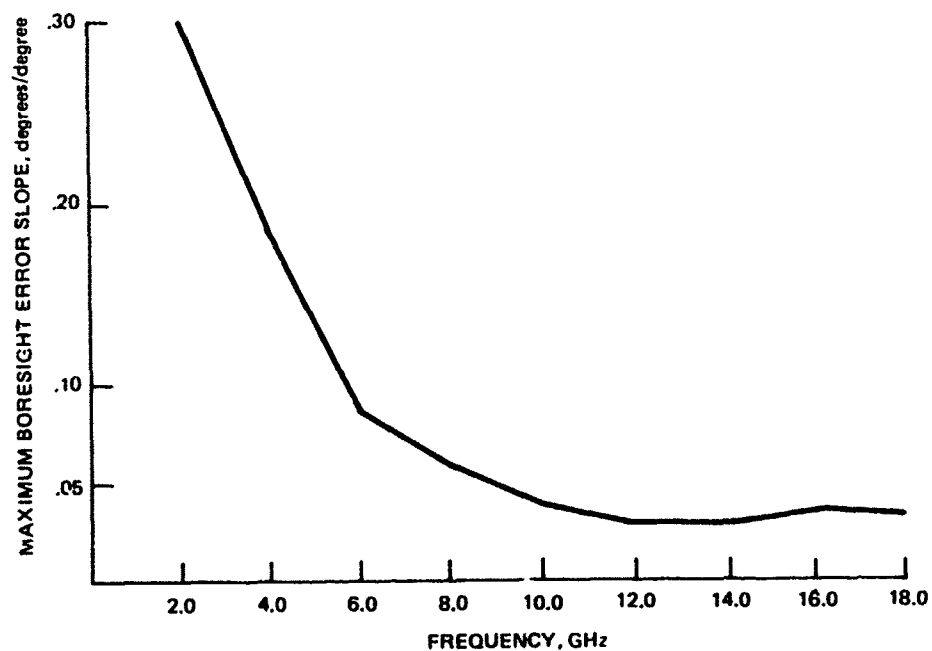


Figure 27. Boresight error slope data for a compensated radome (4-in-diameter antenna at 12-in station).

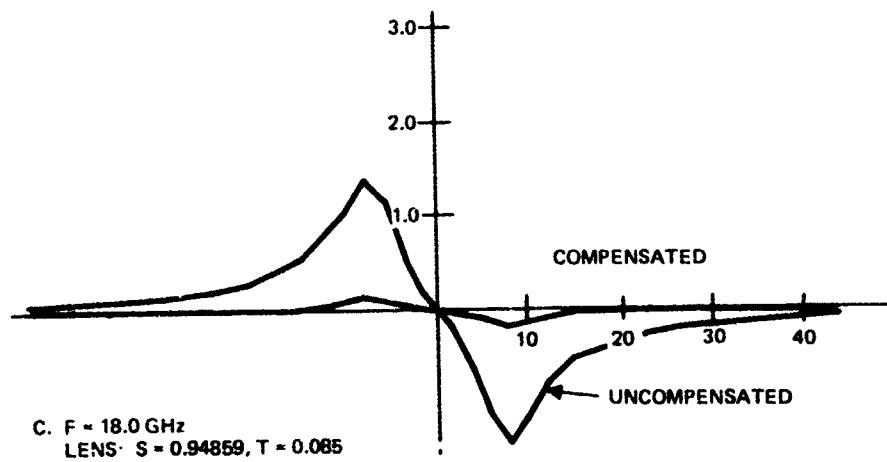
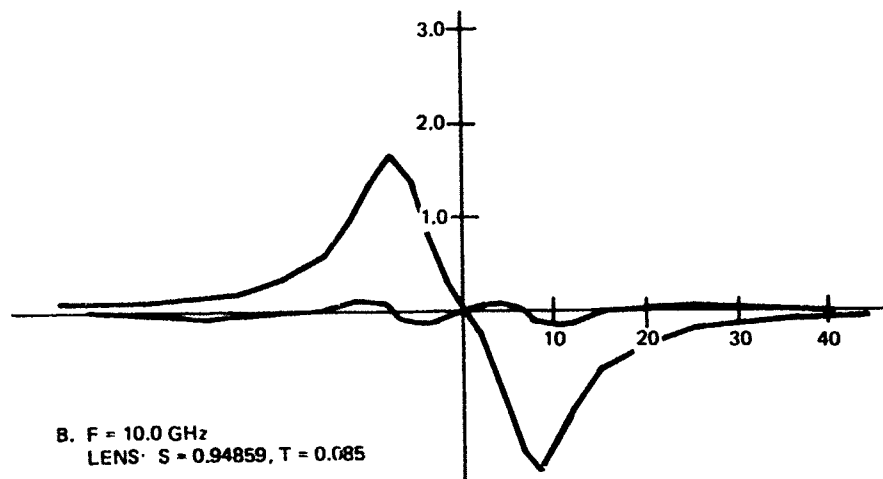
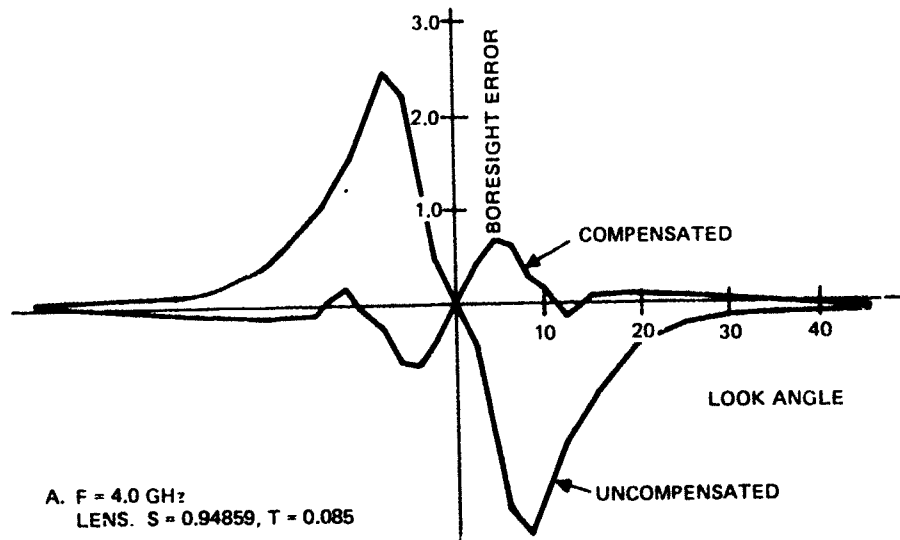


Figure 28. Boresight error data (4-in-diameter antenna at 12-in station — alternate lens).

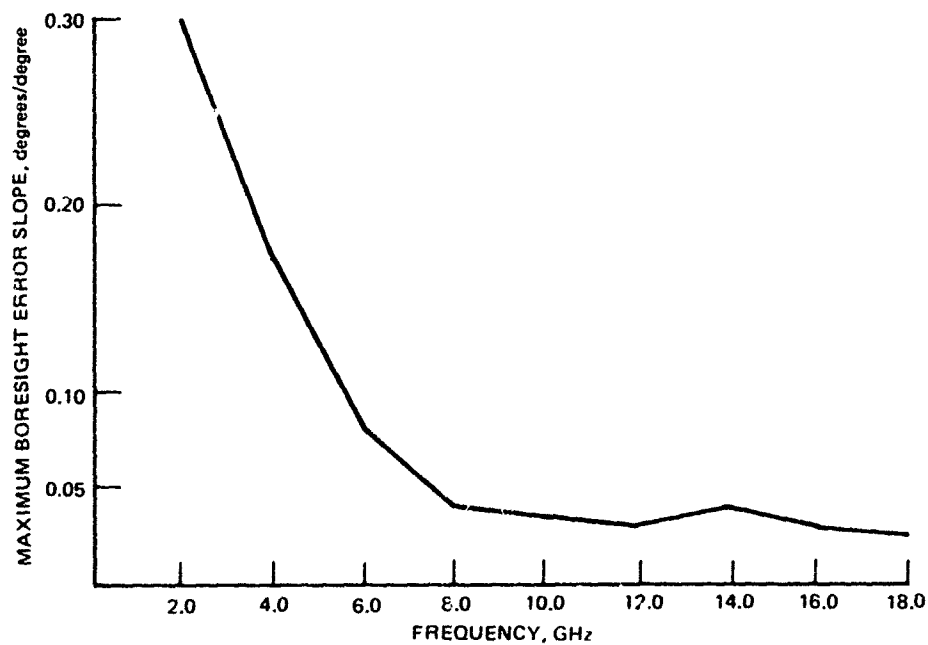


Figure 29. Boresight error slope data for a compensated radome (alternate lens for 4-in-diameter at 12-in station).

TABLE 5. BORESIGHT ERROR DATA DESCRIPTION.

Figure	Frequency (GHz)	Radome Equation $y=4(\frac{x}{18})^n$	Lens Equation (Parabolic) $y=s\sqrt{x-T}$	Lens/Radome Intercept (in)	Antenna Aperture Diameter (in)	Antenna Station (from radome nose tip, in)
24(A)	4.0	$n=0.5$	$s=0.95564$ $T=0.08$	3.0	2.0	6.0
24(B)	8.0	$n=0.5$	$s=0.95564$ $T=0.08$	3.0	2.0	6.0
24(C)	18.0	$n=0.5$	$s=0.95564$ $T=0.08$	3.0	2.0	6.0
26(A)	4.0	$n=0.5$	$s=0.95299$ $T=0.08$	4.0	4.0	12.0
26(B)	8.0	$n=0.5$	$s=0.95299$ $T=0.08$	4.0	4.0	12.0
26(C)	18.0	$n=0.5$	$s=0.95299$ $T=0.08$	4.0	4.0	12.0
28(A)	4.0	$n=0.5$	$s=0.94859$ $T=0.085$	7.0	4.0	12.0
28(B)	10.0	$n=0.5$	$s=0.94859$ $T=0.085$	7.0	4.0	12.0
28(C)	18.0	$n=0.5$	$s=0.94859$ $T=0.085$	7.0	4.0	12.0

descriptive nomenclature that corresponds to the data presented in figures 24-28. The equation of the lenses for the above configurations has the general form of

$$y = S\sqrt{x - T},$$

where T determines the lens thickness at the nose tip of the radome and S determines the lens/radome intercept. The values of T and S are recorded on each data sheet.

What is significant here is that the radome compensation for boresight error slope reduction can be accomplished by the integrated radome/lens technique. The lens must be tailored for a specific antenna aperture and antenna location to minimize the boresight error. The lenses selected in the previous data are not necessarily optimum for the antenna configuration selected. Once the antenna size and station within the radome and wall construction are finalized, the lens can be optimized by the variation-of-parameter technique previously mentioned. Those parameters that would be varied would be lens dielectric constant, lens thickness at nose tip of radome, and lens/radome intercept. A considerable volume of boresight error data was generated for several antenna/antenna station combinations associated with various radome/lens configurations. The antennas ranged from 2 inches in diameter up to 4.5 inches in diameter at various stations. Circular as well as parabolic lenses were analyzed.

Appendix B presents some of the data generated for the various antenna/location and radome/lens combinations. Some of the more important findings are listed in the conclusion section of this report.

MISSILE SYSTEM PERFORMANCE

SEEKER/RADOME MODEL

The electrical performance of the radome has a direct impact on missile performance. This overall interrelation, however, between radome error (as a function of look angle) and missile performance is a complex, nonlinear functional relationship which cannot be evaluated by using classical analysis techniques. This is because of the nonlinear aspect of the radome error. Techniques, however, have been formulated using a linearized analysis to approximate the effect of radome error and specifically radome error slope (rate of change of error with look angle) on overall missile performance.

LINEARIZED SEEKER MODEL

Figure 30 presents a definition of the angles relating the seeker-radome/missile-target geometry. The seeker tracker system is described by the block diagram of figure 31. This block diagram is representative of a missile utilizing a stabilized seeker system. In this block diagram $T_1(S)$ represents the sensor signal processor.

$$T_1(S) = \frac{K_1}{S + \tau_1} \quad (1)$$

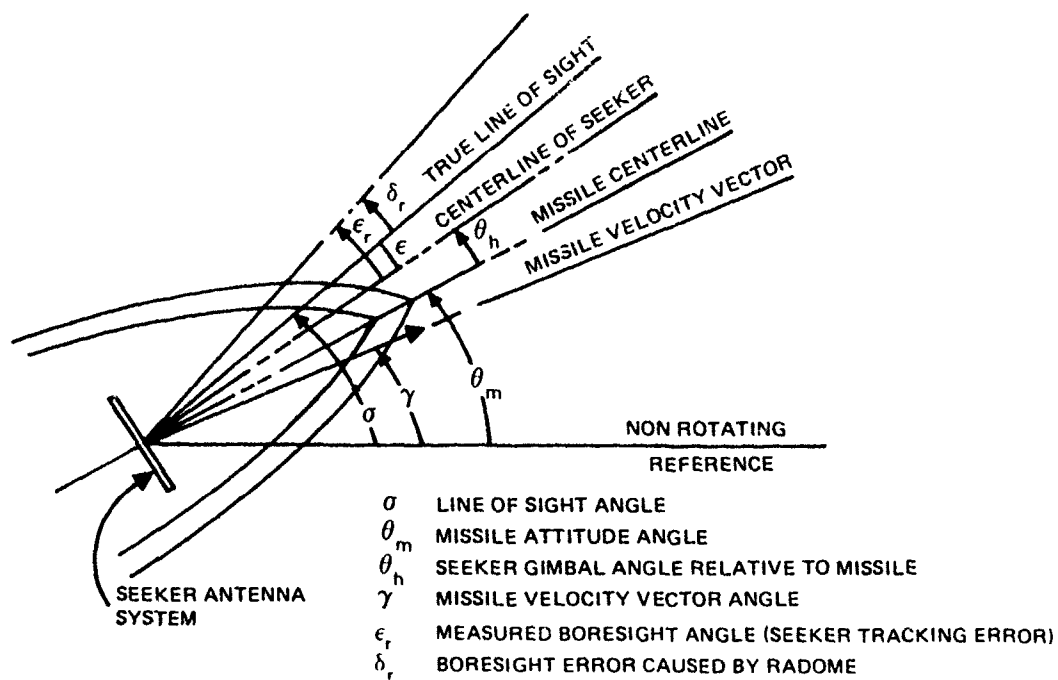


Figure 30. Sensor/missile/target angular relationship.

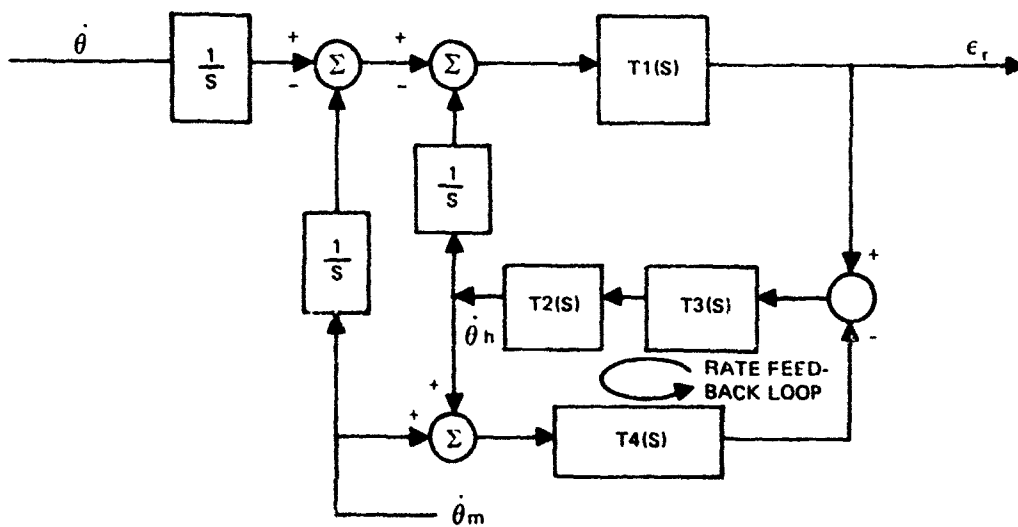


Figure 31. Seeker tracker system block diagram.

$T_2(S)$ is the mechanical drive system for the gimbal system. This can be represented as the transfer function of a second-order system:

$$T_2(S) = \frac{K_2}{1 + \frac{2\delta S}{\omega^2} + \frac{S^2}{\omega_2^2}} \quad (2)$$

$T_3(S)$ is the electrical compensation network which may be represented by a transfer function of the following form:

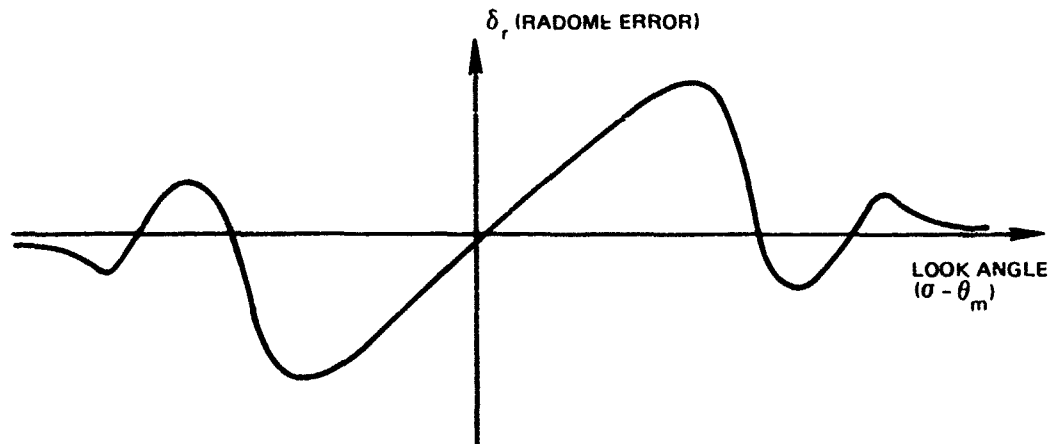
$$T_3(S) = \frac{K_3 (1+\alpha_3 S)^2 (1+\beta_3 S)^2}{(1+\tau_3 S)^2 (1+\tau'_3 S)^2} \quad (3)$$

$T_4(S)$ is the rate sensing gyro which can be represented by second-order transfer function:

$$T_4(S) = \frac{K_4}{1 + \frac{2\delta_4 S}{\omega_4^2} + \frac{S^2}{\omega_4^2}} \quad (4)$$

Figure 31 can be redrawn to illustrate more clearly the stabilization loop and the path by which body motion is coupled into the guidance information. This is shown in figure 32.

The effects of the radome on missile guidance can be included by modifying the seeker subsystem block diagram to include the antenna cover (radome). A typical radome error as a function of look angle is shown below.



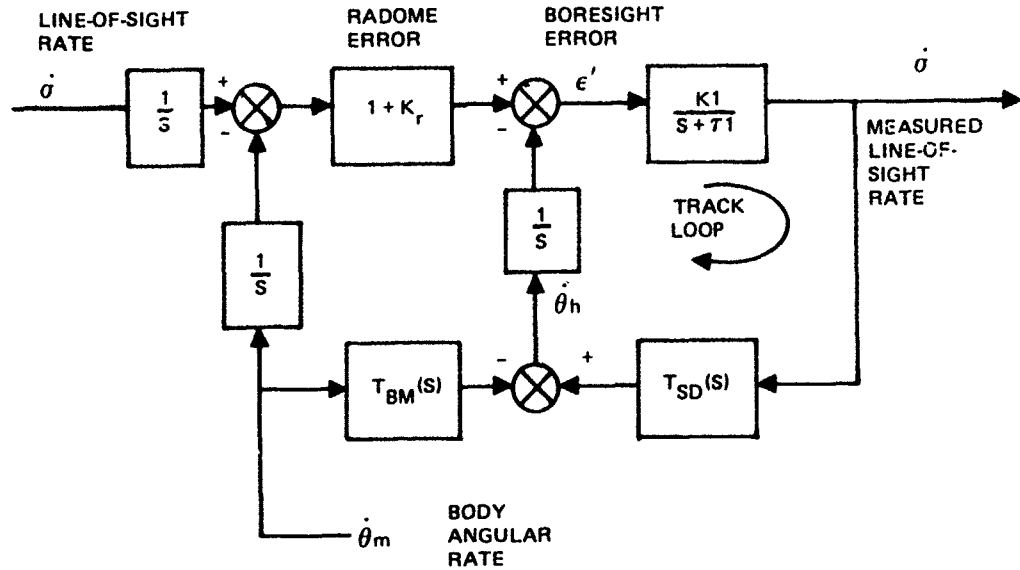


Figure 32. Radome/seeker subsystem block diagram.

This angular error caused by the radome is a nonlinear function of the look angle, and in order to use classical stability and control evaluation techniques – ie, Bode, Nyquist, Routh, etc – the error function must be linearized by some approximation technique. Using a Taylor series approximation of the function where only the first two terms of the series are included

$$\delta_r \approx \delta_{rb} + (\sigma - \theta_m)K_r \quad ; \quad (5)$$

and further specifying that the first term, δ_{rb} , the bias term, is zero, the boresight error caused by the radome can be defined as

$$\delta_r \triangleq (\sigma - \theta_m)K_r \quad (6)$$

Using the linearized definition of the radome error, the seeker tracking error, ϵ_r , can then be defined,

$$\epsilon_r = \delta_r + \epsilon \quad (7)$$

$$\epsilon_r = \delta_r + \sigma - \theta_m - \theta_h \quad (8)$$

or

$$\epsilon_r \approx (1 + K_r)(\sigma - \theta_m) - \theta_h \quad (9)$$

A combined block diagram showing the effects of radome error is presented in figure 32. To isolate the effects of radome error on missile performance to the effect caused by body motion coupling into the guidance signals, the body motion coupling term, $T_{BM}(S)$, will be assumed to be 1. This is true if the rate feedback loop (stabilization loop) shown in figure 31, has a high loop gain; ie,

$$T_2(S) T_3(S) T_4(S) \Big|_{SS} \gg 1. \quad (10)$$

Also, it will be assumed that the stabilization dynamics are high-frequency terms with unity gain, and that there is no filtering within the sensor signal processor; ie,

$$K_{DS} = 1, \quad (11)$$

and the transfer function of the signal processor is K .

Thus, for no radome error contribution,

$$\hat{\dot{\sigma}} = \frac{K_1}{S+K_1} \dot{\sigma} ; \hat{\dot{\sigma}} \text{ is the estimate of line of sight rate.} \quad (12)$$

However, when radome error is added, then the measure line-of-sight rate, $\hat{\dot{\sigma}}$, is defined as

$$\hat{\dot{\sigma}} = \frac{(1+K_r) K_1}{S+K_1} \dot{\sigma} - \frac{K_r}{S+K_1} \dot{\theta}_m, \quad (13)$$

where by examination of (13) it is noted that the measure LOS rate, $\hat{\dot{\sigma}}$, has been corrupted by the added term containing body motion rate.

STABILITY CRITERION FOR LINEAR MODEL

A block diagram describing the seeker/tracker and autopilot airframe is presented in figure 33. This block diagram depicts the parasitic feedback loop wherein body motion rates are feeding into the missile guidance signals, where

τ_F = noise filter time constant

τ_A = autopilot time constant

$\tau_{\dot{\psi}}$ = missile turning rate time constant

N = guidance gain

$$N = \frac{\lambda V_c}{V_{mr}} ; V_c = \text{closing velocity,}$$

$$r = \frac{V_c}{V_{mr}}$$

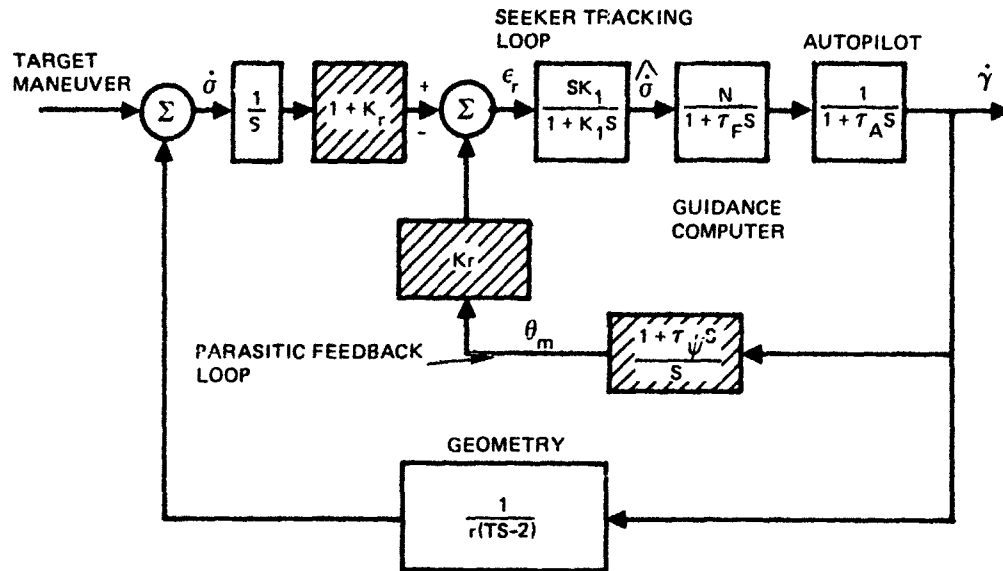


Figure 33. Missile guidance block diagram -- with radome error.

$$V_{mr} = V_m \cos(\sigma - \alpha_m)$$

$$V_m = \text{missile velocity}$$

λ is a constant

$$K_r = \text{radome boresight error slope}$$

T = time-to-go

$$= \frac{R}{V_R}; V_R = -\dot{R}$$

The block diagram of figure 33 can be simplified, where the geometry loop is neglected, as illustrated in figure 34. The characteristic equation for the control system of figure 34 is given by

$$A S^3 + B S^2 + C S + D = 0, \quad (14)$$

where

$$A = \tau_1 \tau_F \tau_A$$

$$B = \tau_1 \tau_F + \tau_A \tau_F + \tau_1 \tau_A$$

$$C = \tau_1 + \tau_F + \tau_A + \tau_\psi N K_r$$

$$D = K_r N + 1$$

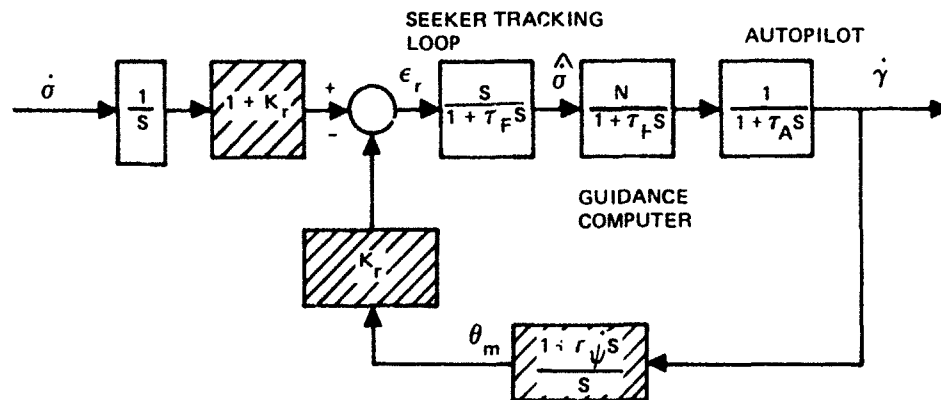


Figure 34. Simplified missile guidance diagram including effects of radome error parasitic feedback loop.

Examination of the characteristic equation will specify the stability properties of the system. A convenient way to examine stability is to use Routh's criterion. System stability requires that (1) no coefficients are missing, (2) all coefficients have same sign, and (3) Routh's array is satisfied. Application of this stability criterion yields the following stability requirements:

$$\tau_i + \tau_F + \tau_A = \tau_\psi NK > 0 \quad (15)$$

or

$$|K_r| < \frac{\tau_i + \tau_F + \tau_A}{N\tau_\psi} \quad (15)$$

and

$$K_r N + 1 > 0$$

or

$$|K_r| < \frac{1}{N} \quad (16)$$

and

$$|K_r| < \frac{(\tau_1 + \tau_F + \tau_A)(\tau_1 \tau_F + \tau_A \tau_F + \tau_1 \tau_A) - \tau_1 \tau_F \tau_A}{N(\tau_1 \tau_F + \tau_A \tau_F + \tau_1 \tau_A) \tau_{\dot{\psi}} - \tau_1 \tau_F \tau_A}$$

If τ_1 and $\tau_F \ll \tau_A$, then the above reduces to

$$|K_r| < \frac{\tau_1 + \tau_F + \tau_A}{N \tau_{\dot{\psi}}},$$

which is identical to (15).

Equation (15) is interesting in that it clarifies the dominant factors affecting stability; ie, the missile turning rate, $\tau_{\dot{\psi}}$, is a function of missile altitude, and the missile-target closing velocity, N , is a function of closing velocity. It is readily seen that the missile tends toward instability for high-velocity intercepts at high altitudes. The important factor to keep in mind about (15) is that it is based on a linearized model. The true relationship of missile instability can be formalized only by using a nonlinear model. The nonlinear model does not lend itself to classical analysis techniques; thus, another approach must be investigated.

NONLINEAR SEEKER MODEL

The analysis and design of physical systems are concerned directly or indirectly with the differential equations of the system and their solutions. If the equations are linear, then the characteristic equations of the system are said to have roots, and these roots define the transient response of the system. Furthermore, if the differential equations are linear, then the principle of superposition applies and the Fourier integral gives a formal relation between the time domain and the frequency domain, thus justifying the use of frequency-response methods of analysis and design.

The key idea of the linear system is that superposition applies. Once the response is known for a given set of initial conditions and input, the references for other inputs and initial conditions are known. Examination of (15) in the previous section points out this principle of superposition in that stability is characterized over a range of conditions (variation in system time constant, altitudes, and intercept velocities).

On the other hand, if there are nonlinear elements within the total system, then the describing differential equations are nonlinear equations and the basic tools for the analysis of linear systems are no longer valid.

For nonlinear systems the concept of a root is not defined, and thus numbers defining the transient performance of a nonlinear system are not readily available. In addition, the principle of superposition is not applicable, and there is no formal mathematical relationship between the time domain and the frequency domain. Thus, if frequency-response methods are used to predict system transient performance, the correlations are empirical rather than mathematical and usually are the result of assumptions which tend to represent the system by some linear equivalent.

The existence of a nonlinearity with resulting nonlinear differential equation does not necessarily result in a transient response that differs radically from the response of a similar

linear system, but it usually does require a great deal of additional mathematical labor in calculating the transient response, and the final result is often unsatisfactory. To elaborate on this, note that a completely analytic solution of a nonlinear differential equation frequently cannot be obtained, and numerical methods must be used to provide a specific solution for assumed (or known) numerical parameters and an assumed disturbance. While these methods result in a specific solution which may be completely satisfactory for some purposes, the usual engineering problem involves a study of the effect of parameter variations and a range of disturbances in order to arrive at an optimum, or nearly optimum, set of conditions which may be interpreted in terms of redesign or adjustment of the system, and the single transient curve obtained by a numerical solution of the system equations is not sufficient for this.

The approach taken here for the analysis of the missile system as a function of a nonlinear element (boresight error as a function of look angle) within the missile system is the parametric variation concept. The initial conditions as well as the nonlinear radome function are varied over a wide range of variables in an organized approach to the parameter variation study. A block diagram of the missile seeker system is presented in figure 35.

The radome boresight error data used in the simulation analysis are shown in figures 36A through 36G. Initial conditions for the representative runs of the missile target encounters are presented in table 6. The data presented are for nonmaneuvering targets. Additional data are being generated for maneuvering targets over a range of launch aspect angles, altitudes, and velocities. Figures 37A through 37C present linearized boresight error data of the corresponding actual data. The miss distance was used as a measure of performance for the missile system performance analysis. Figures 38A through 38I present the results of the simulation in terms of miss distance as a function of the linear model radome error data and the actual radome error data. It is seen in all the curves that the linearized data resulted in much higher miss distances than the actual nonlinear radome boresight error data after which the linearized data were modeled. From the data presented, it appears that miss distances of 20 feet or less would result if the maximum absolute radome boresight error slope for actual nonlinear data over the $\pm 45^\circ$ of look angles (even at altitudes up to 60k feet) were held to 0.12 degree per degree averaged over a 5° look window.

It must be pointed out, however, that this conclusion is based on a small sample of simulation runs. Data are currently being generated that will look at a broader base of launch aspect angles and maneuvering target cases. The one conclusion that has emerged from the study of this matter thus far, however, is that the linearized approximation of the radome error does not present a realistic picture from which to bound the radome boresight error slope requirements!

Also of significance is the fact that radome error affects missile performance to a lesser degree if the boresight error as a function of look angle does not have long linear segments. The more the error is nonlinear and oscillates back and forth from positive to negative, the less the impact on missile performance.

These results amplify similar findings obtained by Army Missile Command, Code (DRSMI-RE) Huntsville, Alabama.

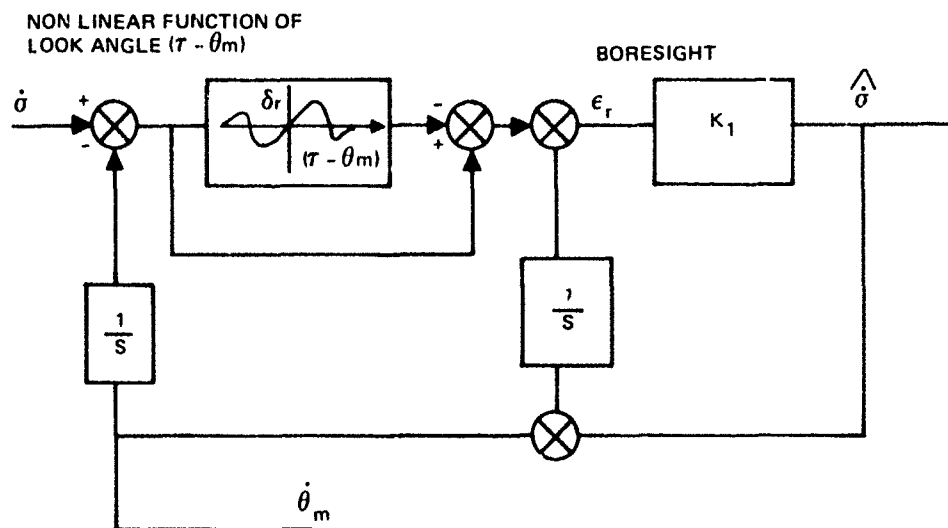


Figure 35. Nonlinear radome/seeker subsystem block diagram.

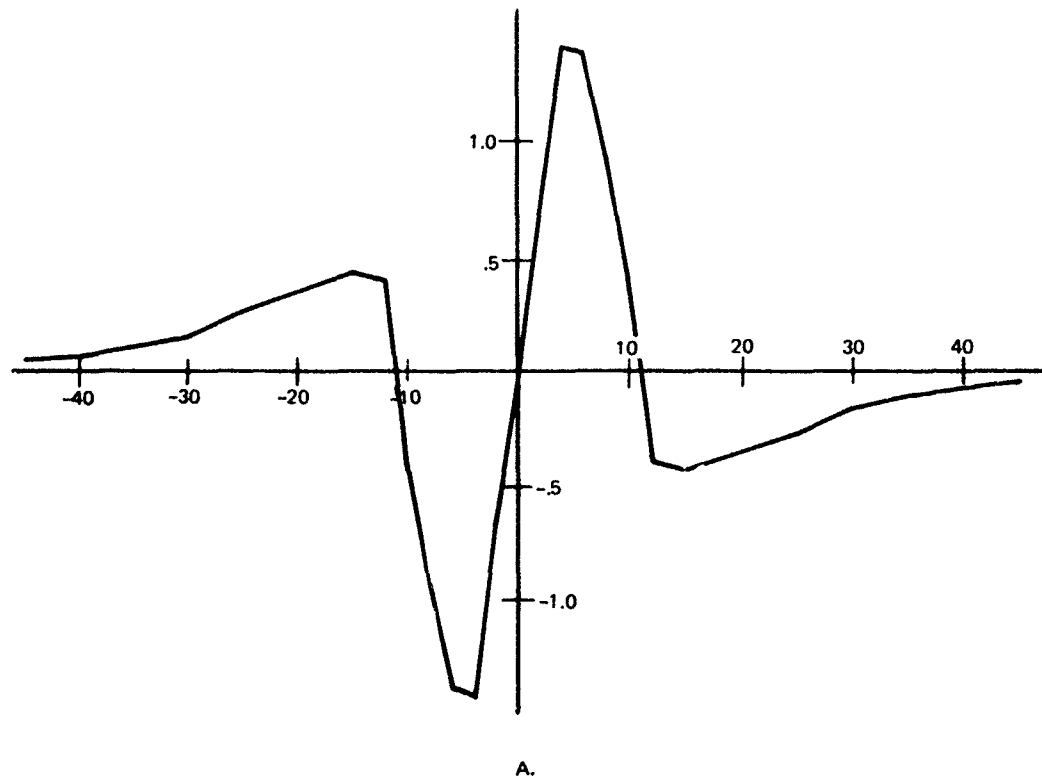


Figure 36. Radome error vs look angle.

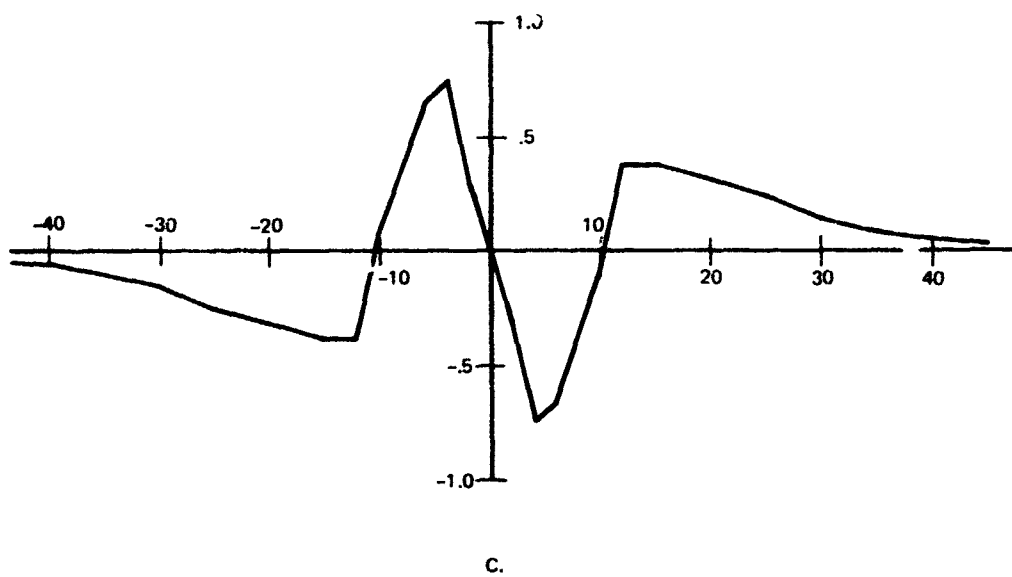
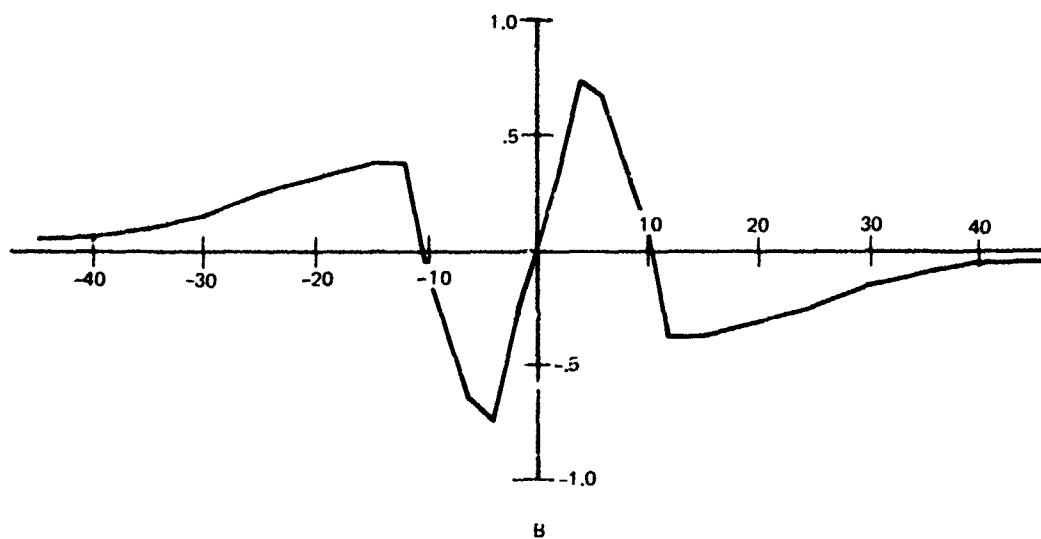
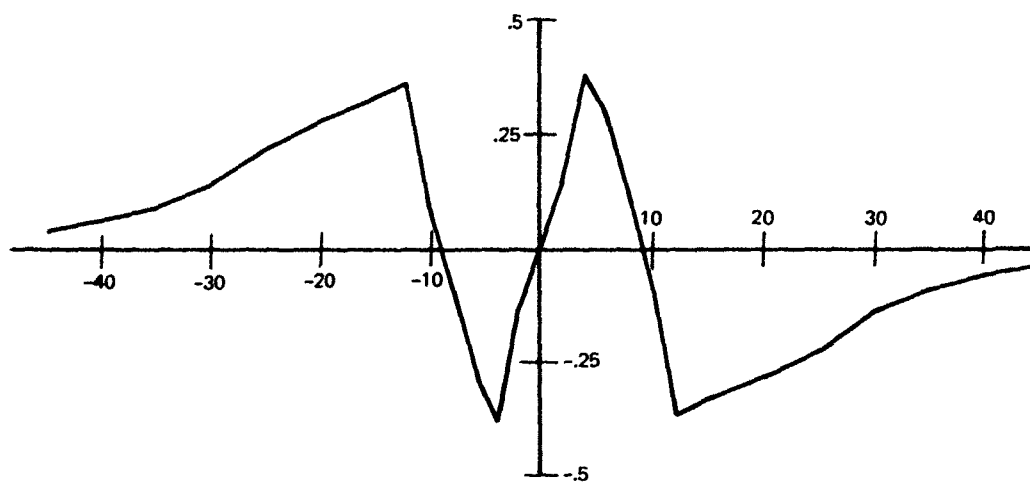
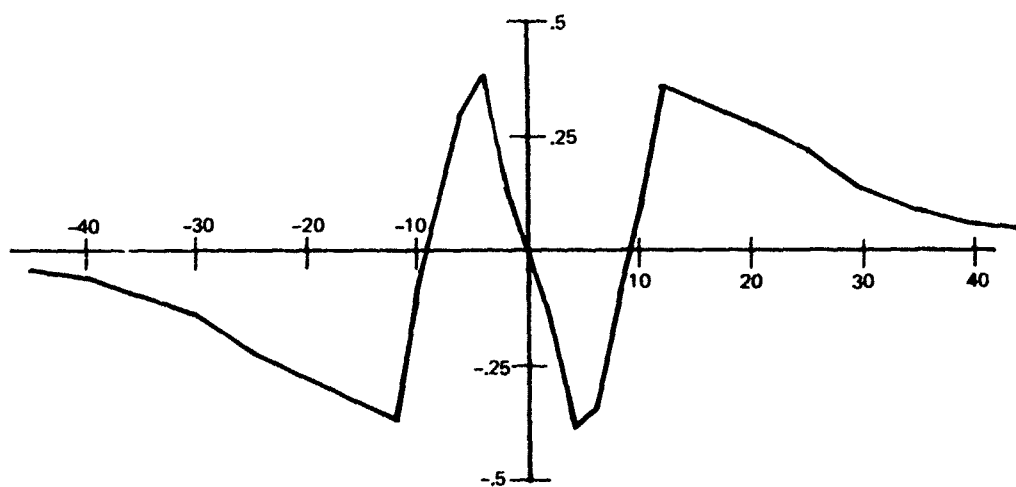


Figure 36 (Continued).

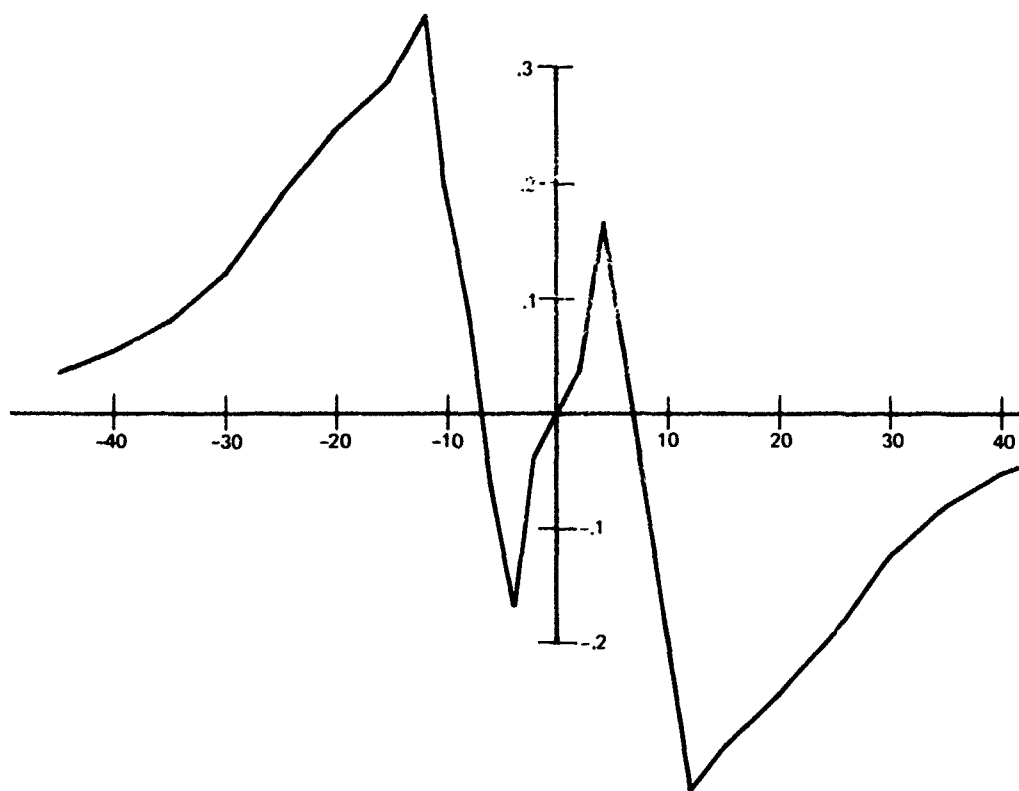


D.

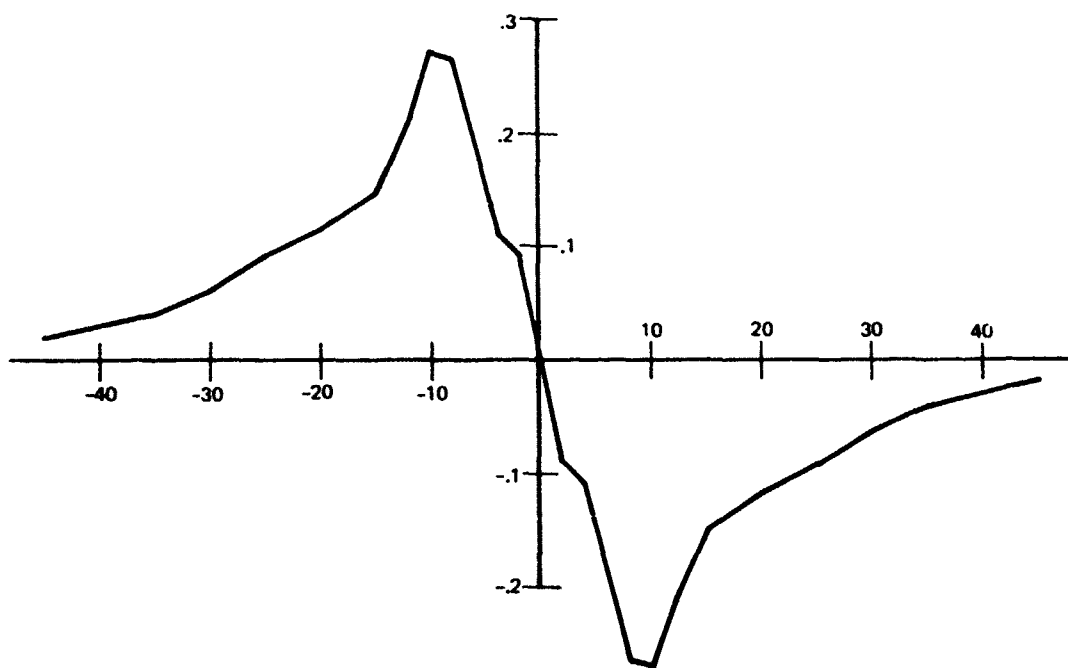


E.

Figure 36 (Continued).



F.



G.

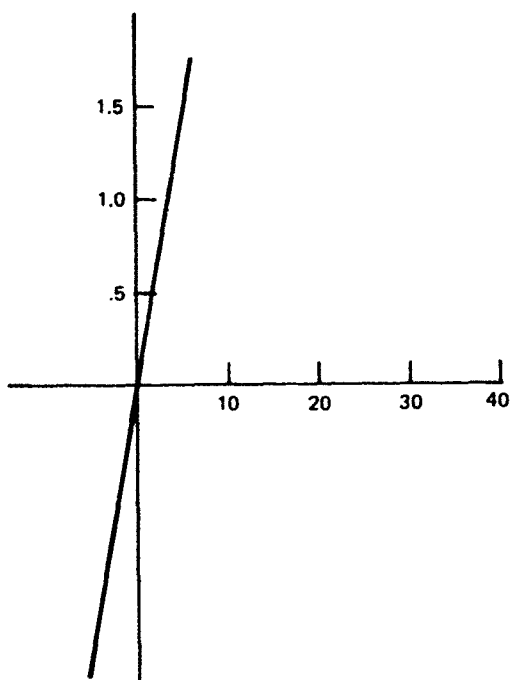
Figure 36 (Continued).

TABLE 6. REPRESENTATIVE RUNS OF MISSILE-TARGET ENCOUNTERS.

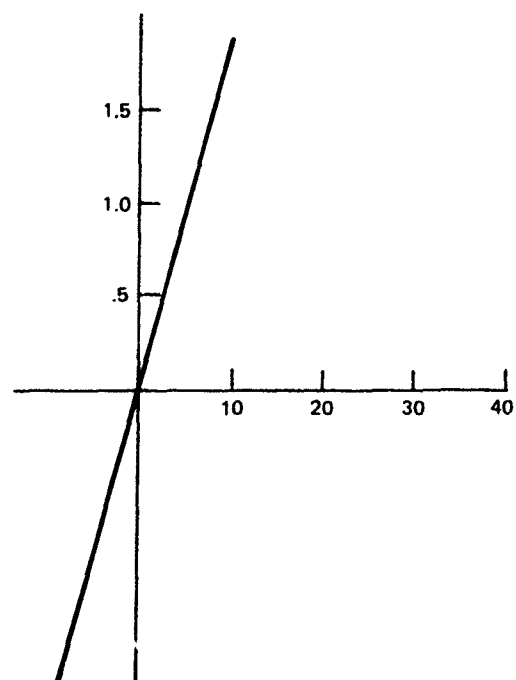
Launch Altitude, ft		Launch Velocity-Mach no		Radome Error Data	Launch Aspect Angle	Miss Distance, ft
Missile	Target	Missile	Target			
20k	20k	.9	.8	fig 36F	head-on 4° offset	1.97
35k	35k	.9	.8	fig 36F	head-on 4° offset	4.96
65k	65k	.9	.8	fig 36F	head-on 4° offset	5.6
20k	20k	.9	.8	fig 36F	head-on 20° offset	4.9
35k	35k	.9	.8	fig 36F	head-on 20° offset	4.4
60k	60k	.9	.8	fig 36F	head-on 20° offset	7.1
20k	20k	.9	.8	fig 36A	head-on 4° offset	27.7
35k	35k	.9	.8	fig 36A	head-on 4° offset	21.6
60k	60k	.9	.8	fig 36A	head-on 4° offset	49.2
20k	20k	.9	.8	fig 36A	head-on 20° offset	90.2
35k	35k	.9	.8	fig 36A	head-on 20° offset	41.7
60k	60k	.9	.8	fig 36A	head-on 20° offset	114.16
20k	20k	.9	.8	fig 36G	head-on 4° offset	8.9
35k	35k	.9	.8	fig 36G	head-on 4° offset	2.9
60k	60k	.9	.8	fig 36G	head-on 4° offset	6.7
20k	20k	.9	.8	fig 36G	head-on 20° offset	2.8
35k	35k	.9	.8	fig 36G	head-on 20° offset	6.6
60k	60k	.9	.8	fig 36G	head-on 20° offset	19.7
20k	20k	.9	.8	fig 36B	head-on 4° offset	11.8
35k	35k	.9	.8	fig 36B	head-on 4° offset	12.6
60k	60k	.9	.8	fig 36B	head-on 4° offset	31.96
20k	20k	.9	.8	fig 36B	head-on 20° offset	8.02
35k	35k	.9	.8	fig 36B	head-on 20° offset	4.6
60k	60k	.9	.8	fig 36B	head-on 20° offset	28.9
20k	20k	.9	.8	fig 36D	head-on 4° offset	5.80
35k	35k	.9	.8	fig 36D	head-on 4° offset	8.81
60k	60k	.9	.8	fig 36D	head-on 4° offset	14.5
20k	20k	.9	.8	fig 36D	head-on 4° offset	6.0
35k	35k	.9	.8	fig 36D	head-on 4° offset	2.5
60k	60k	.9	.8	fig 36D	head-on 4° offset	7.15
35k	35k	.9	.8	-1 * 4 GHz	4°	5.0259
60k	60k	.9	.8	-1 * 4 GHz	4°	19.7233
35k	35k	.9	.8	constant error slope = -0.1875	4°	5.4709
60k	60k	.9	.8	constant error slope = -0.1875	4°	23.0367

TABLE 6 (Continued).

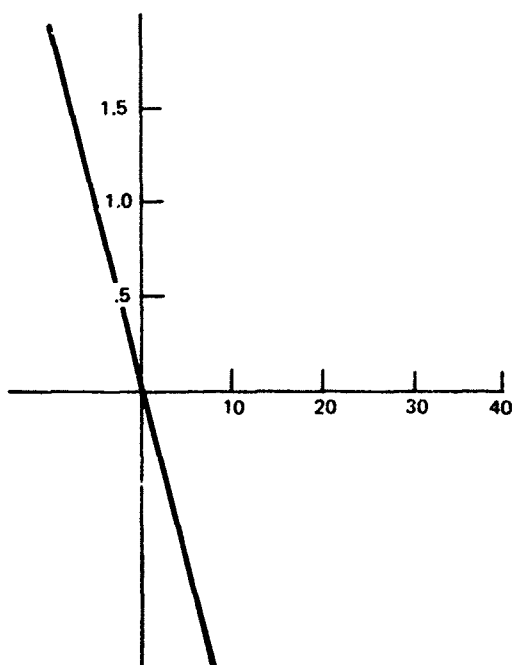
Launch Altitude, ft		Launch Velocity-Mach no		Radome Error Data	Launch Aspect Angle	Miss Distance, ft
Missile	Target	Missile	Target			
35k	35k	.9	.8	-1 * 6 GHz	4°	3.4799
60k	60k	.9	.8	-1 * 6 GHz	4°	9.5927
35k	35k	.9	.8	constant error slope = -0.095	4°	4.5133
60k	60k	.9	.8	constant error slope = -0.095	4°	12.5377
35k	35k	.9	.8	-1 * 4 GHz	head-on 20° offset	4.44
60k	60k	.9	.8	-1 * 4 GHz	head-on 20° offset	36.34
35k	35k	.9	.8	constant slope -0.1875	head-on 20° offset	28.301
60k	60k	.9	.8	constant slope -0.1875	head-on 20° offset	103.79
35k	35k	.9	.8	-1 * 6 GHz	head-on 20° offset	2.34
60k	60k	.9	.8	1 * 6 GHz	head-on 20° offset	13.88
35k	35k	.9	.8	constant slope -0.095	head-on 20° offset	28.297
60k	60k	.9	.8	constant slope -0.095	head-on 20° offset	52.98



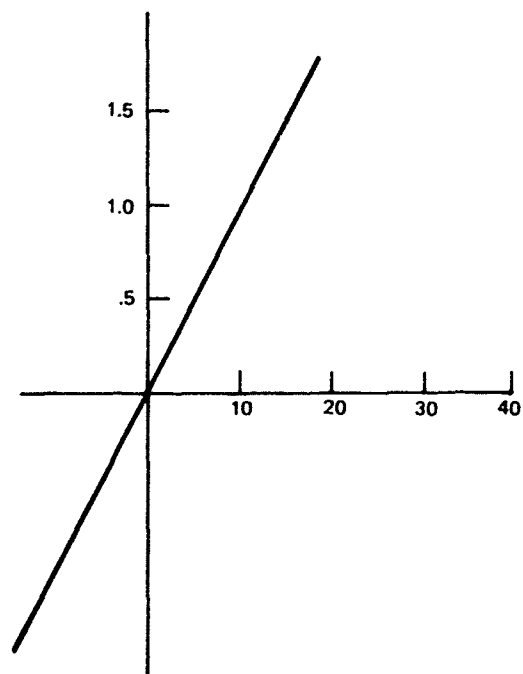
A. ERROR OF FIG 36A
SLOPE = 0.3



B. ERROR OF FIG 36B
SLOPE = 0.1875

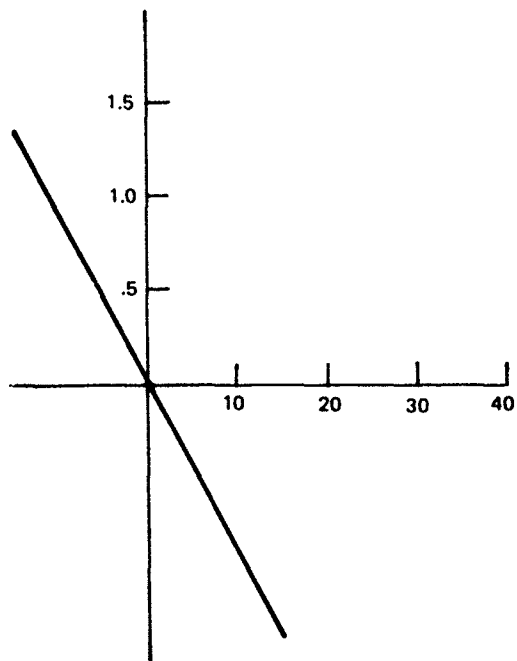


C. ERROR OF FIG 36C
SLOPE = -0.1875

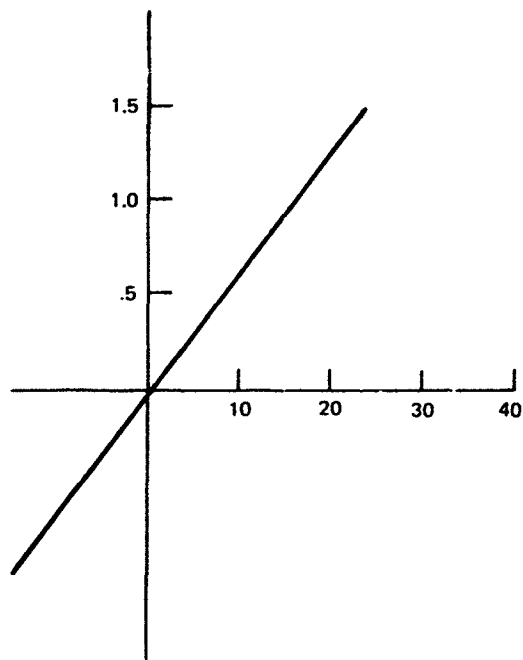


D. ERROR OF FIG 36D
SLOPE = 0.095

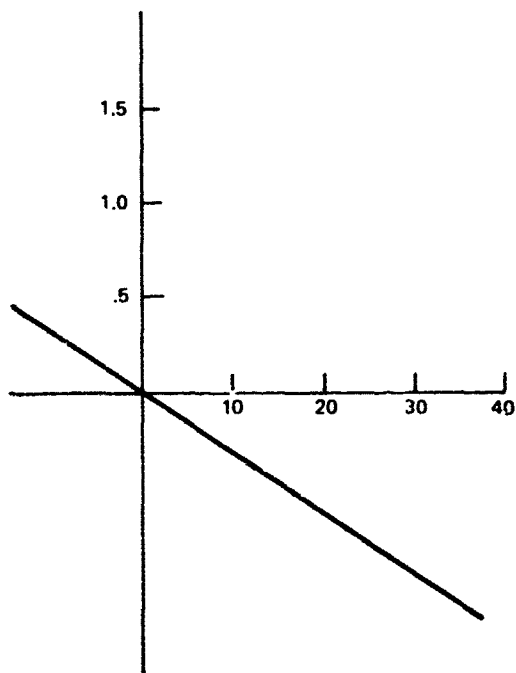
Figure 37. Linear models of boresight errors.



E. ERROR OF FIG 36E
SLOPE = -0.095



F. ERROR OF FIG 36F
SLOPE = 0.0625



G. ERROR OF FIG 36G
SLOPE = -0.03125

Figure 37 (Continued).

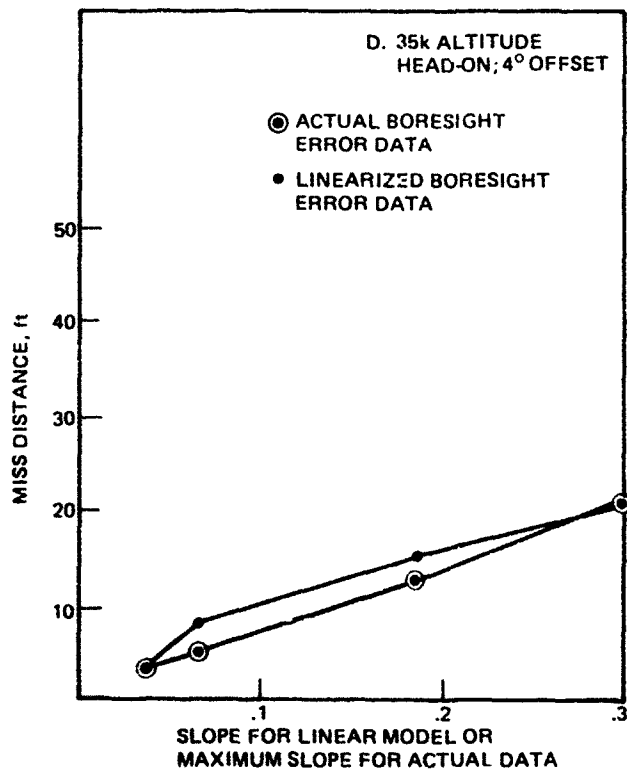
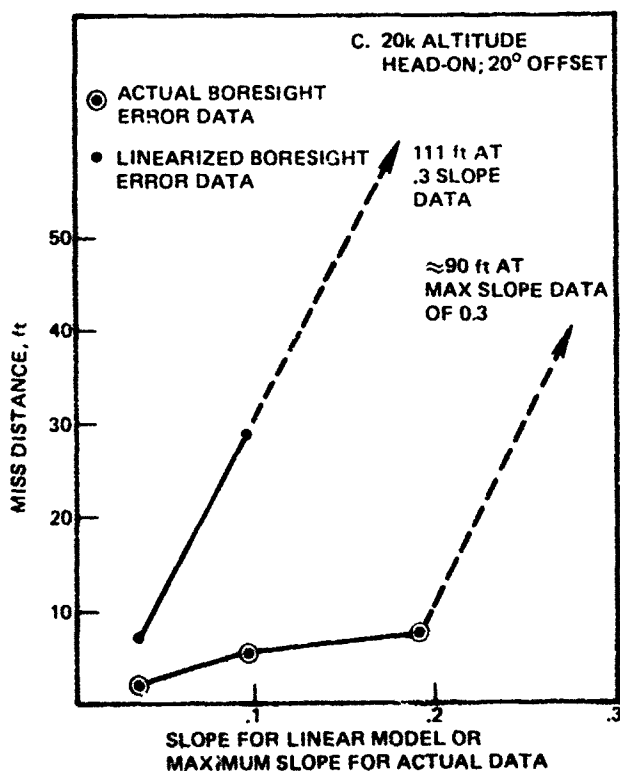
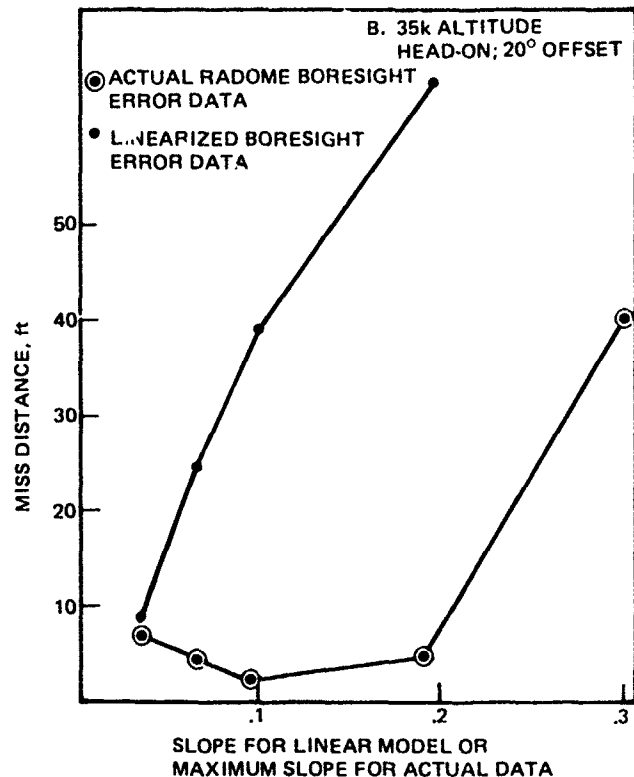
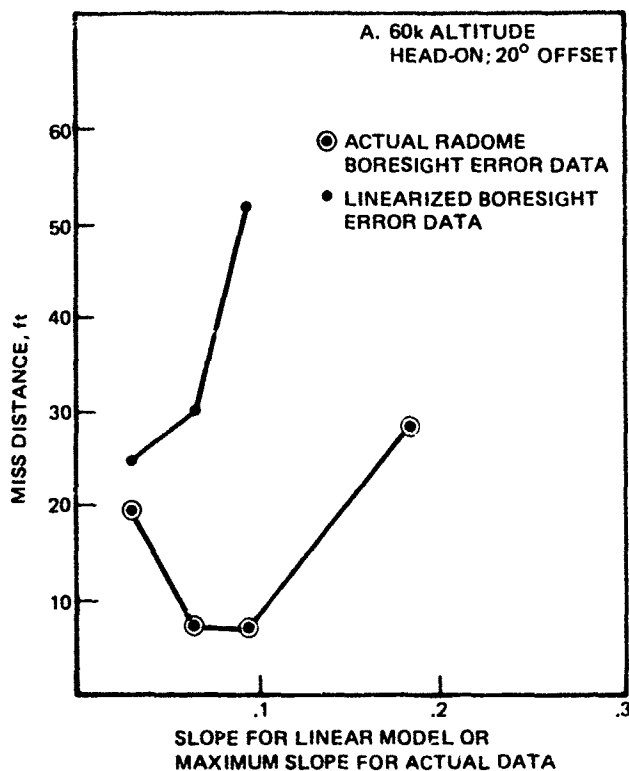


Figure 38. Miss distance as a function of radome error/error slope.

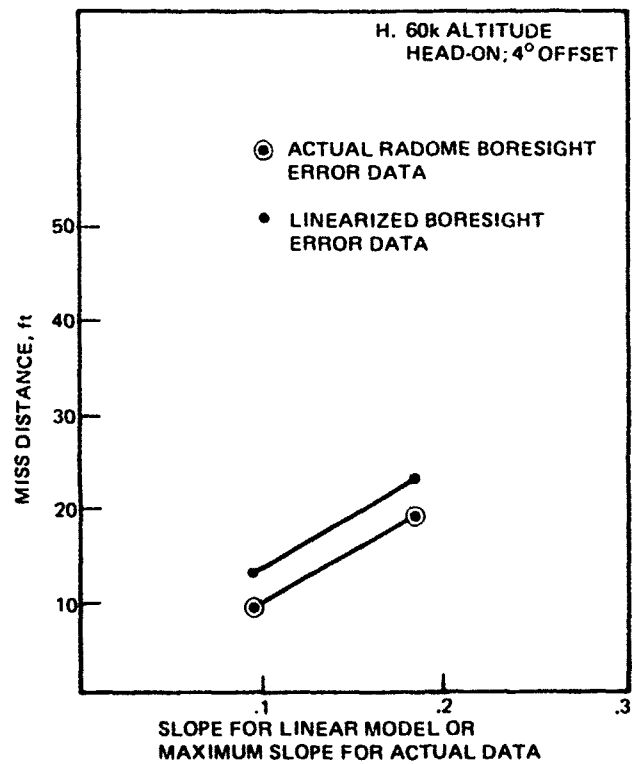
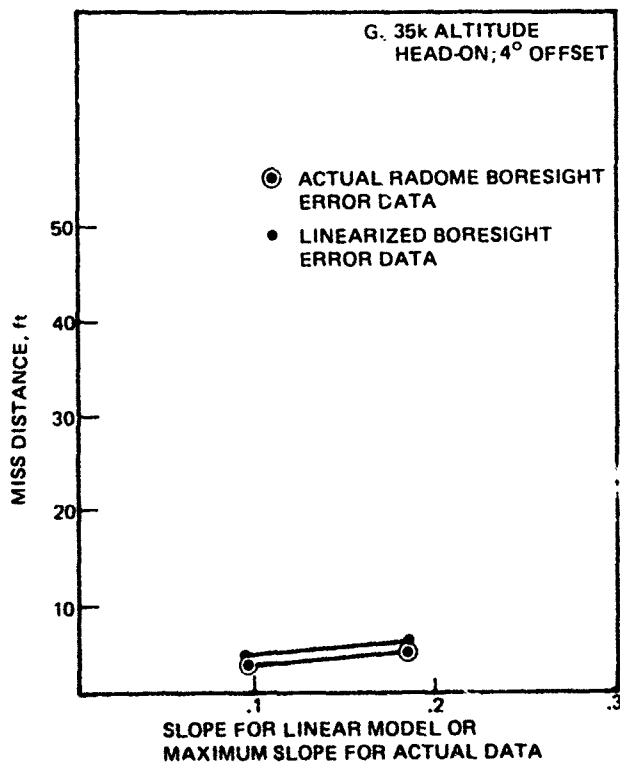
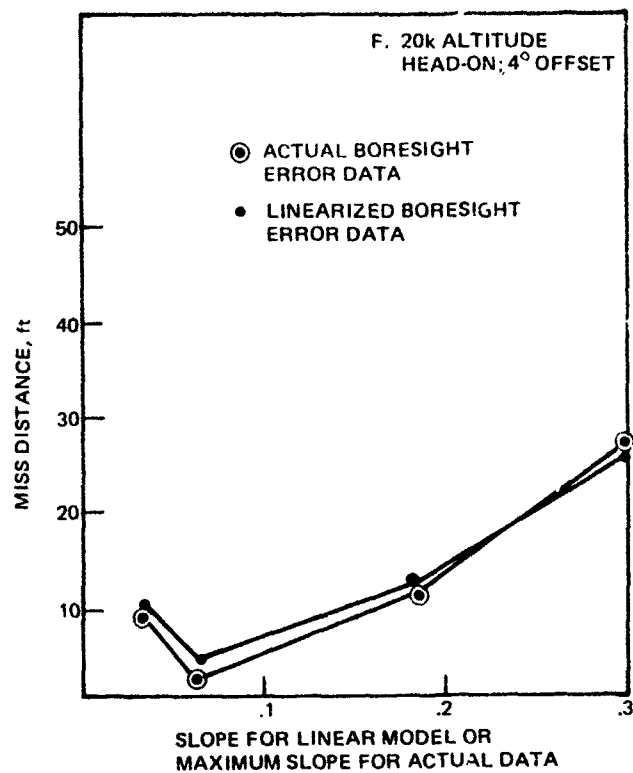
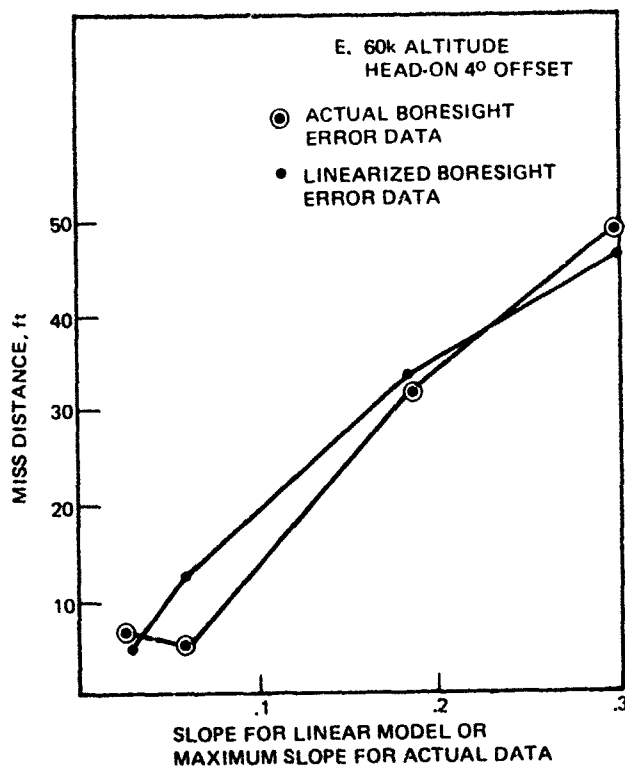


Figure 38 (Continued).

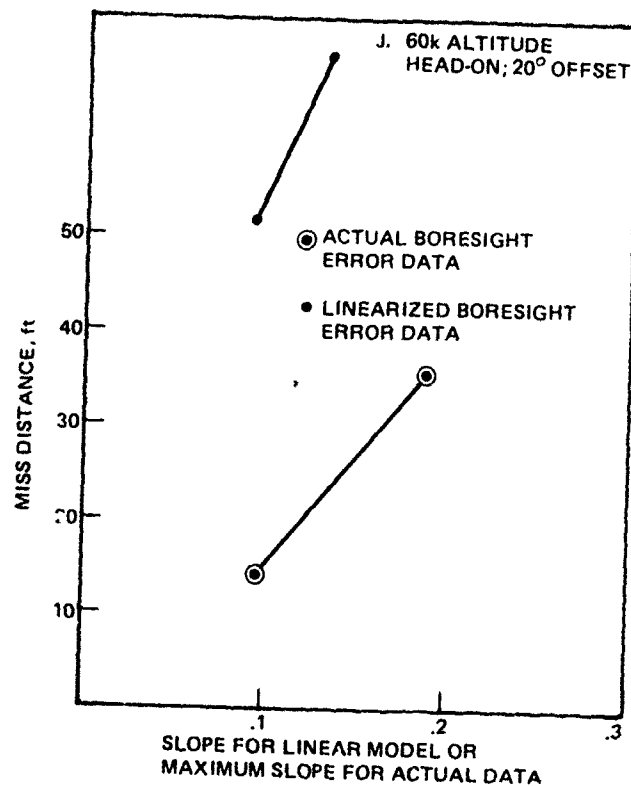
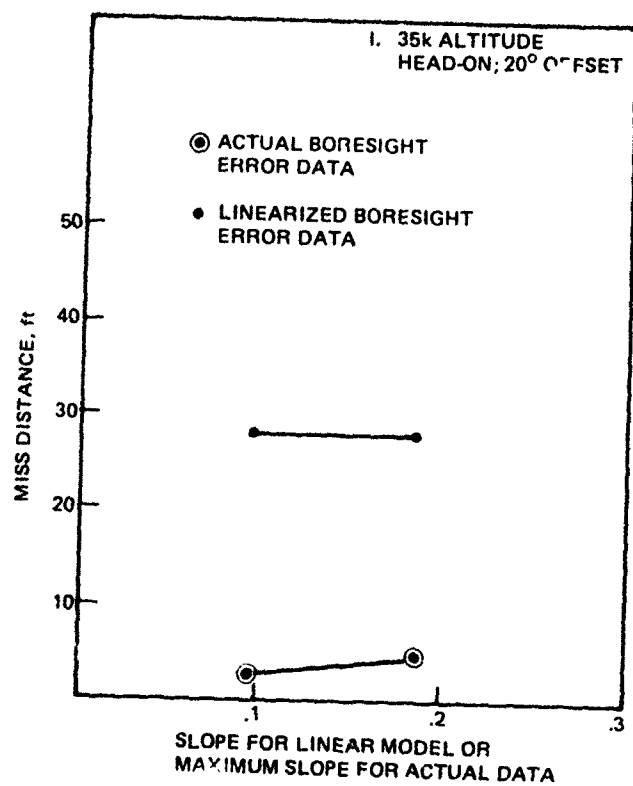


Figure 38 (Continued).

CONCLUSION

It was concluded that a lensed radome can be developed to operate over a multioctave band of frequencies that satisfies the drag and electrical performance requirements. This approach presents a method for meeting system performance requirements with an inexpensive process. It is anticipated that radomes can be manufactured at hundreds of dollars per unit copy as compared to the thousands of dollars per unit copy presently in effect. The analysis indicates that maximum boresight error and, more important, boresight error slope, do not degrade missile performance. The radome lends itself to a multiple rf sensor application (passive/active). For missile trajectory profiles of flight times of 60 seconds at speeds of mach 2.5, and at altitudes of 5000 feet or more, the materials will survive the thermal and rain erosion environments. The radome lends itself to being manufactured by means of an inexpensive molding process.

AERODYNAMIC CONSIDERATIONS

DRAG

The primary aerodynamic consideration was drag. A shape was determined that has good aerodynamic drag performance yet is flexible enough to allow compensation for good electrical performance. It was concluded that the shape that would best meet these criteria was a power series defined by the relationship

$$y = R \left(\frac{x}{L} \right)^n.$$

where

R is the base radius

L is the overall length

n is the power coefficient

For the 18-inch radome with an 8-inch base diameter, the 0.5 power series was determined to yield overall best drag with greatest potential for electrical boresight error compensation. The drag of the 0.5 power series radome was 4% less than the equivalent tangent ogive drag.

RAIN EROSION

A rain erosion sled test was performed on a hemispherical ogive (hemi-ogive) radome constructed of a rain-resistant material built by AVCO. The radome survived the

800 feet of rain at an average velocity of 2535 feet per second. Calculations were performed to estimate the maximum limits of rain erosion that the hemi-ogive radome could withstand. Traveling at an average velocity of 2500 ft/s, the radome could withstand 3600 feet of rain; at 3500 ft/s, 1850 feet of rain; and at 4500 ft/s, 1125 feet of rain. These are estimates for the hemi-ogive configuration; for the 0.5 power series the rainfield could be greater in length at all the above velocities.

THERMAL

Thermal structure limits on radome materials vary widely, as do electrical properties. Materials for this effort were chosen for the ease with which they could be shaped in a manufacturing process. The goal was to find a material that meets electrical and thermal requirements yet can be easily manufactured into the desired shape at minimum cost. The primary materials selected for the layered radome concept were AVCOAT 8027 and a fiber glass substructure.

The AVCOAT is a noncharring ablative material that ablates at a constant temperature; thus, at high temperatures the heat is carried away from the radome surface during the ablative process. The AVCOAT does not present a thermal problem for current projected flight profiles. The material in question is the fiber glass substructure. The question is whether the fiber glass will fail thermally under projected flight profiles.

A calculation was carried out for a 60-second flight at an average speed of mach 2.5 at 5000 feet of altitude. The fiber glass surface achieved a 400°F temperature (204°C). This is below thermal limits of the material. The time required for the substructure to reach thermal limits is beyond the projected flight characteristics.

ELECTRICAL PERFORMANCE

The two areas of electrical performance that were addressed were transmissivity and boresight error.

TRANSMISSIVITY

Transmission requirements were analyzed for several classes of missiles (passive, active, and semiactive). Most of the effort, however, was for the passive and active categories. It was pointed out that, in general, passive systems have much longer operating ranges than active systems; and that transmission radome losses on the order of 3 or 4 dB do not pose a serious problem, as a 3-dB loss is approximately a 30% operating range reduction. For the active system, a radome loss is not serious if transmitter power is easily attainable. However, if the state of the art limits transmitting power and maximum ranges are required, then radome losses become more serious.

It is interesting that the combination of a passive and active system does not place stringent operating range requirements on the terminal (active) portion of the system.

With a 3 - 5-nmi (5.4 - 9.0-km) range requirement, and 50 watts of average transmitting power available, the radome losses have less impact. A 3-dB loss will cut the range by

approximately 30%. A 4.68-nmi operating range is cut to 3.11 nmi when radome loss is included. For a terminal seeker only, the relative difference between 4.68 and 3.11 nmi is not significant.

The lensed radome over a 1 - 20-GHz frequency band had insertion losses of less than 4 dB for incident angles of 50° or less. A window for an active system was available at the higher end of the frequency band (see fig 15).

BORESIGHT ERROR

Boresight error is caused by the addition of insertion phase to the incident electromagnetic energy as it passes through the radome wall. The insertion phase varies along the radome wall due to radome curvature. A technique for compensating the radome was to vary the inner wall curvature (different from the outer wall curvature) in such a way that a reverse insertion phase effect was achieved. By doing this, boresight error could be reduced by as much as 75 to 1. Boresight error is a function of many variables, the more predominant being:

- Shape
- Frequency
- Antenna station
- Antenna aperture size
- Lens shape

Three classes of radome shapes were analyzed. In all cases the boresight error as a function of frequency (over an operating band of frequencies) decreased at the higher end of the frequency band. The tangent ogive performed better for a medium-size antenna stationed farther back in the radome than for a smaller antenna placed in the nose of the radome. Just the opposite was noted for the unlensed power series radome. Its best performance was for smaller antennas located close to the nose of the radome. The best performance of all shapes considered was for the lensed power series radome. The lens had to be tailored for the specific antenna at a given location. If the antenna size or location varied, a specific lens had to be tailored to fit the circumstances. Performance over the 8 - 18-GHz frequency band in terms of boresight error slope could be held to less than 0.05 degree per degree. This was true for smaller antennas in the nose of the radome and also for larger antennas farther back.

MISSILE PERFORMANCE

Missile performance was analyzed as a function of boresight error in terms of boresight error slope. The analysis was done parametrically on the digital computer with a six-degree-of-freedom missile simulation for nonlinear boresight error functions for the radome model. The results were compared to the linearized boresight error model of the nonlinear boresight error function.

In all cases the missile performance was far better (performance was a measure of miss distance) for the nonlinear boresight error model of the radome. The analysis was done for varying aspect angles of a head-on intercept over a range of altitudes varying from 20 000 to 60 000 feet. In all cases, if the maximum boresight error slope was less than 0.12 degree

per degree over a 5° window in look angle over the -45° to $+45^\circ$ look angle range, missile performance was within limits (miss distances less than 20 feet). The one important feature pointed out was that the linearized approximation did not yield representative missile performance from which to bound the radome error slope requirements. The linearized analysis technique for generating radome boresight error slope limit bounds places severe manufacturing specifications on the radome at exorbitant cost to the government. The preliminary results obtained in this report indicate that a new look is required at techniques for specifying radome error slope requirements.

SUMMARY

The objectives of the radome design were (1) provide an aerodynamic shape that will not degrade missile performance, (2) define a wall construction and materials design that will provide transmission over a broad frequency range plus satisfy the rain erosion and thermal heating requirements, and (3) provide required electrical boresight error performance. A power series shaped radome with an integrated lens was selected as the basis for the design. This shape provides drag characteristics equivalent to those of conventional state-of-the-art low-drag radomes. Multilayer-wall construction was elected. The outside layer, a low-dielectric-constant material, provides protection from subsonic rain erosion. The second layer is a noncharring ablative material with good supersonic rain erosion properties. The third layer is a fiber glass substructure. By selecting appropriate dielectric in each layer, a good impedance match from air to succeeding layers is obtained. An integrated lens provides compensation for variation in insertion phase, which results in good electrical boresight error performance.

RECOMMENDATIONS

In the radome analysis described by this effort a number of important areas were addressed relative to radome development and requirement specifications. The drag considerations were analyzed by theoretical means and compared to actual wind tunnel data. Further efforts in this area are not required. The rain erosion data presented in this effort are for a hemispherical ogive shape. It is recommended that a number of sled tests be performed to obtain rain damage assessment for the power series radome.

The thermal considerations were established solely by analytical means. It is recommended that actual thermal testing be initialized to evaluate the radome materials and establish actual thermal limits. Transmissivity was also established solely by analytical means and actual measurements to verify these analytical predictions should be conducted. Boresight error was established solely by analytical means. It is recommended that measurements be made to verify the boresight error prediction estimates. Missile performance as a function of radome error was analyzed via parametric analysis. Only air-to-air was investigated at what was considered worst-case intercept conditions for a nonmaneuvering target. It is recommended that the effort be expanded to include maneuvering targets at a wide range of launch aspect angles. It is also recommended that air-to-ground encounter be evaluated.

REFERENCES

1. Chin, SS, "Missile Configuration Design," McGraw Hill Book Co, 1961
2. USAF Stability and Control DATCOM, vol 2, DE Ellison, September 1970
3. "Techniques for Airborne Radome Design," Dr TE Tice, editor-in-chief (vol 1 and 2)
4. "Tactical Missile Ablative Radomes," GW Christiansen and JP Ott, The Tenth Symposium on Electro Magnetic Windows, Georgia Institute of Technology, July 1970

BIBLIOGRAPHY

1. Antenna Engineering Handbook, Jasik, Editor, McGraw Hill Book Co, 1961
2. Final Technical Report, David CF Wu, and RC Rudduck, The Ohio State University Electro Science Laboratory, Final Report 2969-4, March 1971
3. Hughes Aircraft Company, Technical Memorandum 235, Summary Report, Guidance and Control. LL Bailin et al
4. Mathis, HF, "Transmission Characteristics of Sandwiches," IRE Transactions, Microwave Theory and Techniques, October 1955
5. Nathanson, FE, "Radar Design Principles," McGraw Hill Book Co, 1969
6. Puckett, A. and Ramo, S, "Guided Missile Engineering," McGraw Hill Book Co, 1959
7. Ramo, S, Whinnery, JR, and Van Duzer, T, "Fields and Waves in Communication Electronics," John Wiley and Sons, Inc, New York, 1967
8. Truxal, JG, "Control Systems Synthesis," McGraw Hill Book Co, 1955

APPENDIX A: BORESIGHT ERROR PROGRAM MODEL

A derivation of the ray-tracing method used in the boresight error analysis program is given in this appendix along with a flow chart of the program. It is assumed that the antenna is tilted at some gimbal angle β , and that a plane electromagnetic wave, traveling perpendicularly to the antenna, is incident on the radome. Rays are then taken from points along the outer radome surface and traced to the antenna. The insertion phase delay for each ray is computed, thus giving a phase front across the antenna. From this phase front the boresight error is calculated.

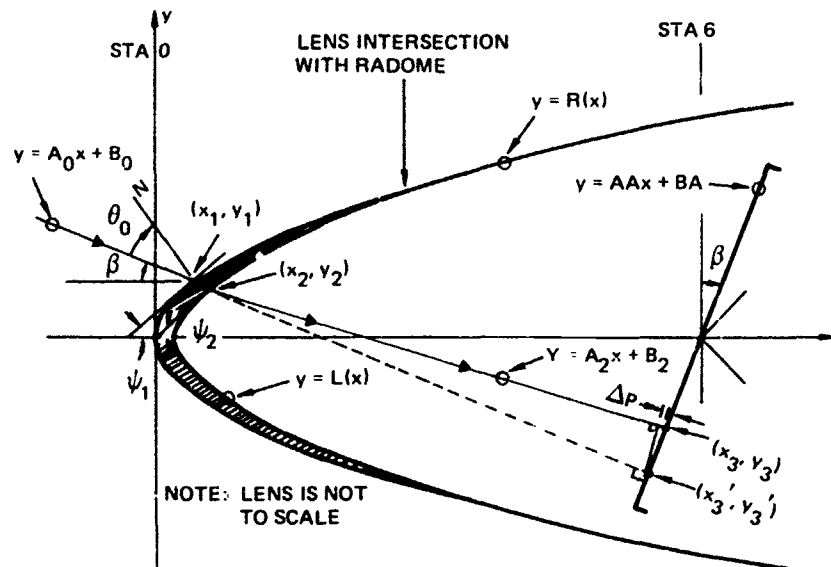


Figure A1. Radome/antenna geometry.

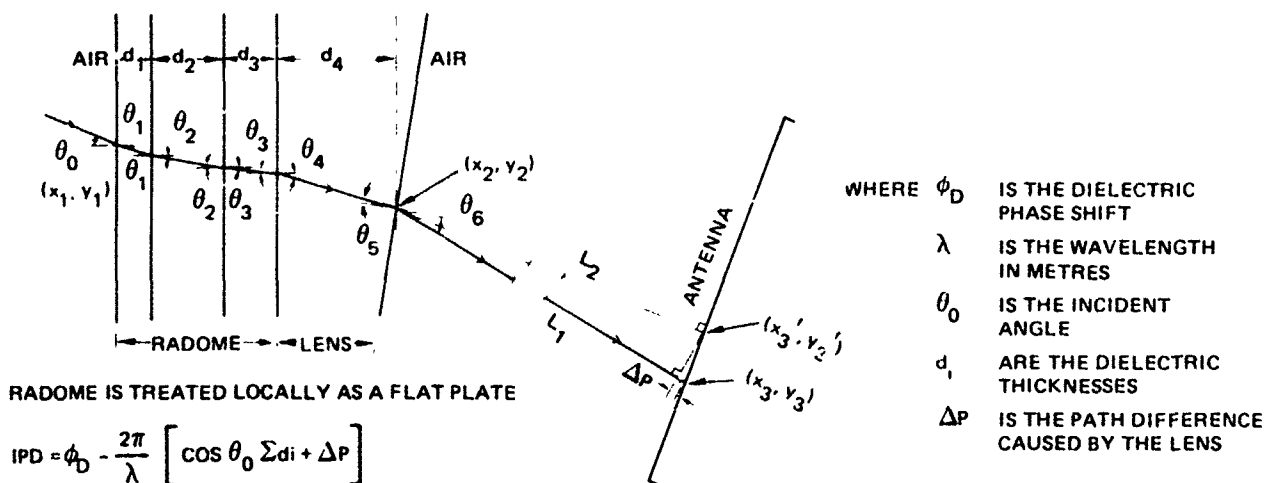


Figure A2. Ray-tracing geometry.

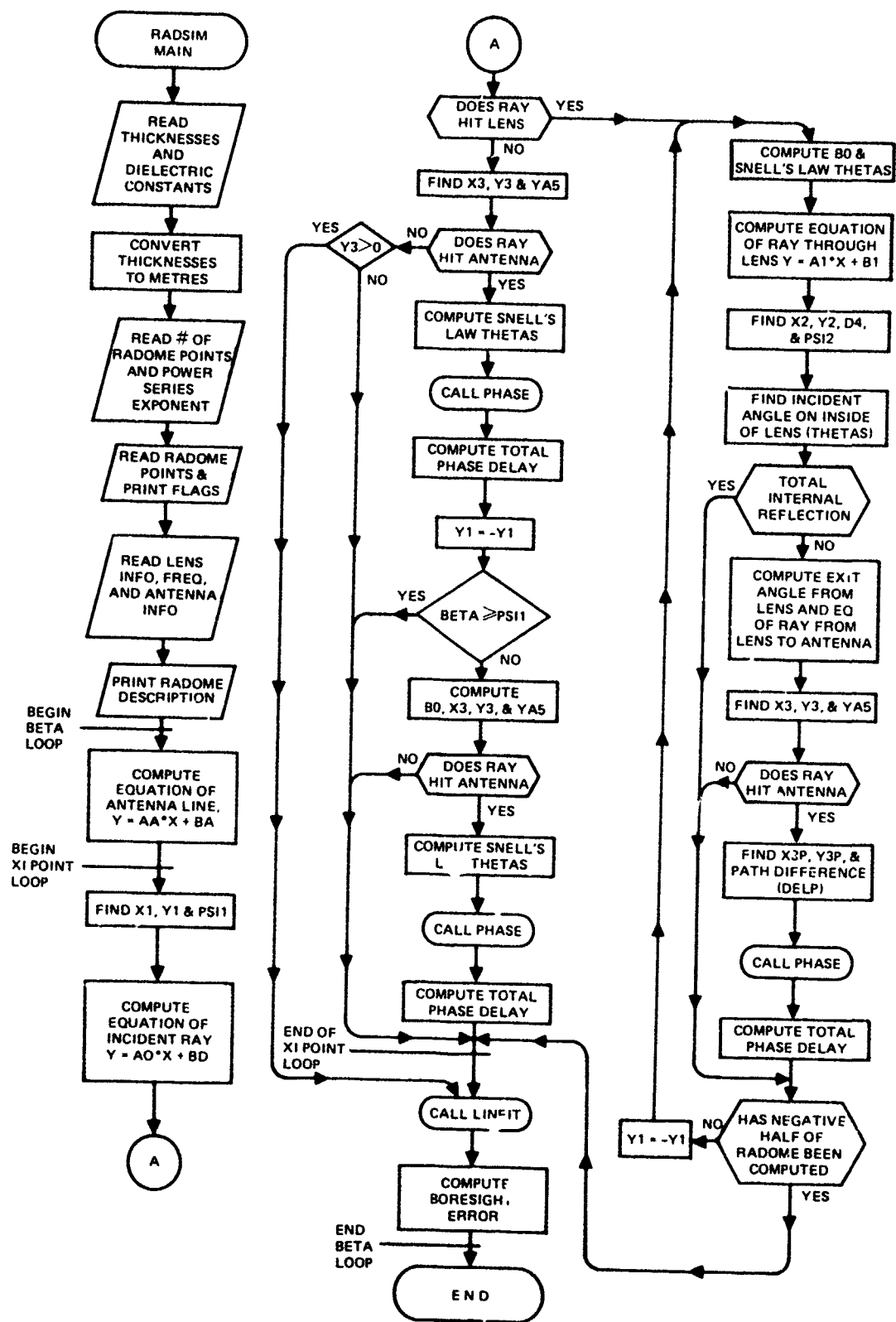
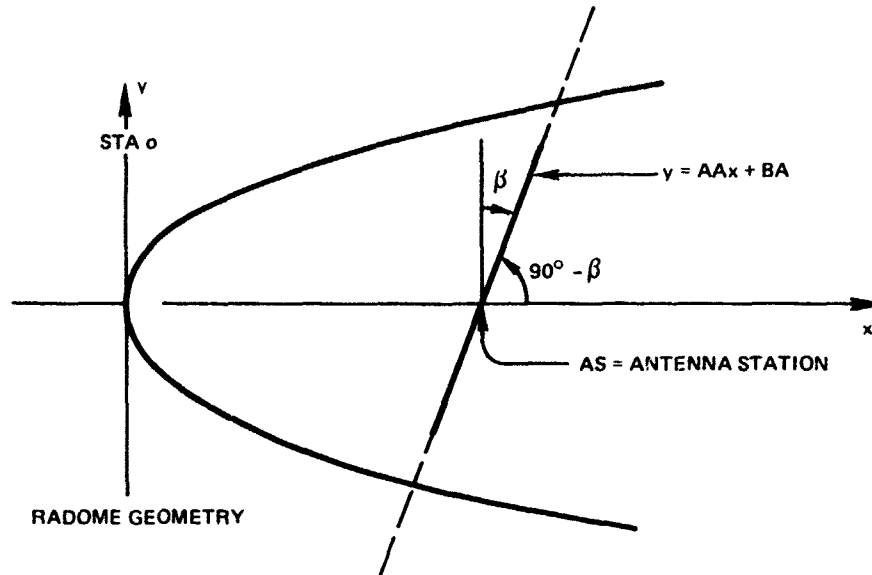


Figure A3. Program flow chart.

RADOME SIMULATION GEOMETRY

I. GENERAL GEOMETRY FOR CLEAN RADOME (NO LENS)

A. Computation of antenna line equation, $y = AA * X + BA$, given β (gimbal angle)

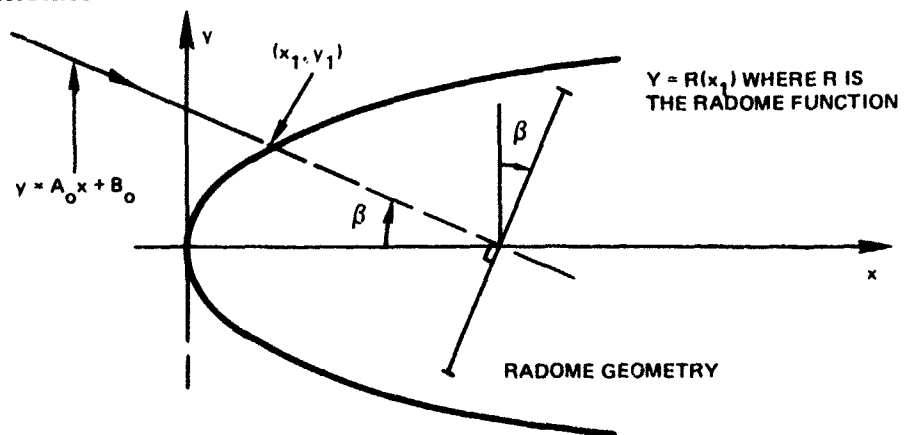


$$\text{Slope} = AA = \tan(90^\circ - \beta) = \frac{1}{\tan \beta},$$

$$(y-o) = \frac{1}{\tan \beta} (x-AS) = \frac{x}{\tan \beta} - \frac{AS}{\tan \beta}.$$

$$\text{So } AA = \frac{1}{\tan \beta}, \quad BA = -\frac{AS}{\tan \beta}.$$

B. Computation of equation of incident ray line, $y = A_o x + B_o$, given β and point (x_1, y_1) of incidence



Slope = $A_0 = -\tan \beta$.

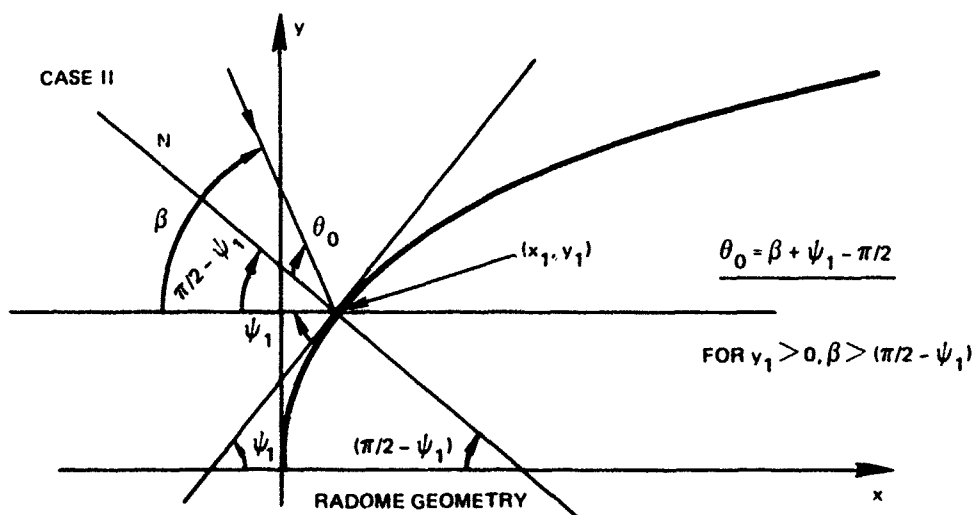
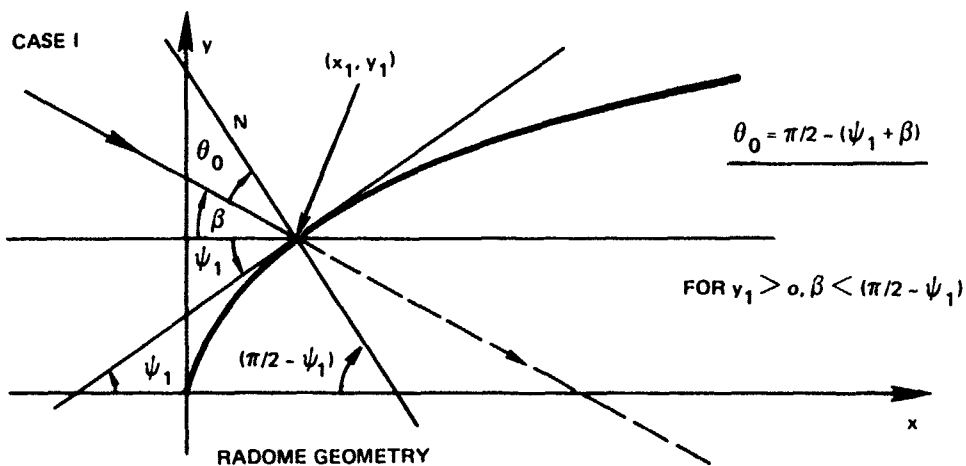
Using point (x_1, y_1) ,

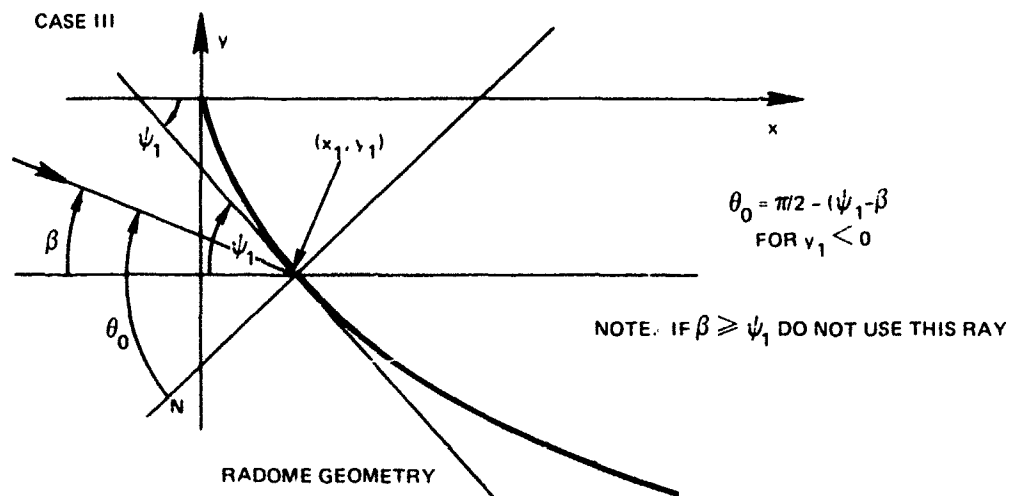
$$y - y_1 = A_0 (x - x_1)$$

$$y = A_0 x - A_0 x_1 + y_1.$$

$$\therefore A_0 = -\tan \beta, B_0 = y_1 - A_0 x_1 = y_1 + x_1 \tan \beta$$

C. Computation of incident angle θ_0 , given gimbal angle, β , and ψ_1 , the slope angle of the radome equation at point (x_1, y_1) [$\psi_1 = \tan^{-1} (R'(x_1))$]. Note: θ_0 is always a positive angle. N indicates the normal line.



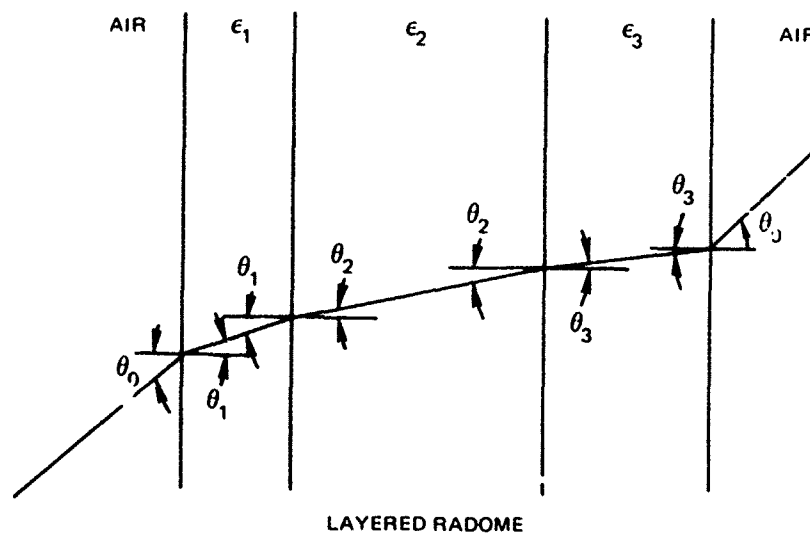


Summary for θ_0

$$\theta_0 = \begin{cases} \text{abs}(\pi/2 - (\psi_1 + \beta)) & \text{for } y_1 > 0 \text{ Cases I \& II} \\ \pi/2 - (\psi_1 - \beta) & \text{for } y_1 < 0 \text{ Case III} \end{cases}$$

Note: x_1 will never be 0 $\Rightarrow y_1 \neq 0$.
also, $\theta_0 = 0.0$ if $\beta = \pi/2 - \psi_1$.

D. Computation of Snell's Law Thetas



By Snell's Law, $\frac{\sin \theta_i}{\sin \theta_{i-1}} = \sqrt{\frac{\epsilon_{i-1}}{\epsilon_i}}$.

Then $\theta_i = \sin^{-1} \left(\sqrt{\frac{\epsilon_{i-1}}{\epsilon_i}} \sin \theta_{i-1} \right)$, $i = 1, 2, 3$.

E. If ray does not hit lens, do the following; if ray does hit lens, go to sec II, Lens Geometry.

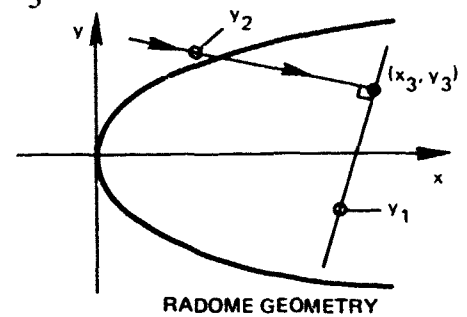
Computation of point at which ray hits antenna (x_3, y_3)

1. Equation of antenna line $y_1 = AA \cdot x + BA$

2. Equation of ray line $y_2 = A_o \cdot x + B_o$

$$AA \cdot x_3 + BA = A_o \cdot x_3 + B_o$$

$$x_3 = \frac{B_o - BA}{AA - A_o}, \quad y_3 = AA \cdot x_3 + BA$$



F. Finally the phase due to path difference (ϕ_p) is given by

$$\phi_p = 2\pi/\lambda (D1 + D2 + D3) \cos \theta_0,$$

where λ is the wavelength in metres

D_i are the various layer thicknesses in metres

and the total insertion phase is given by

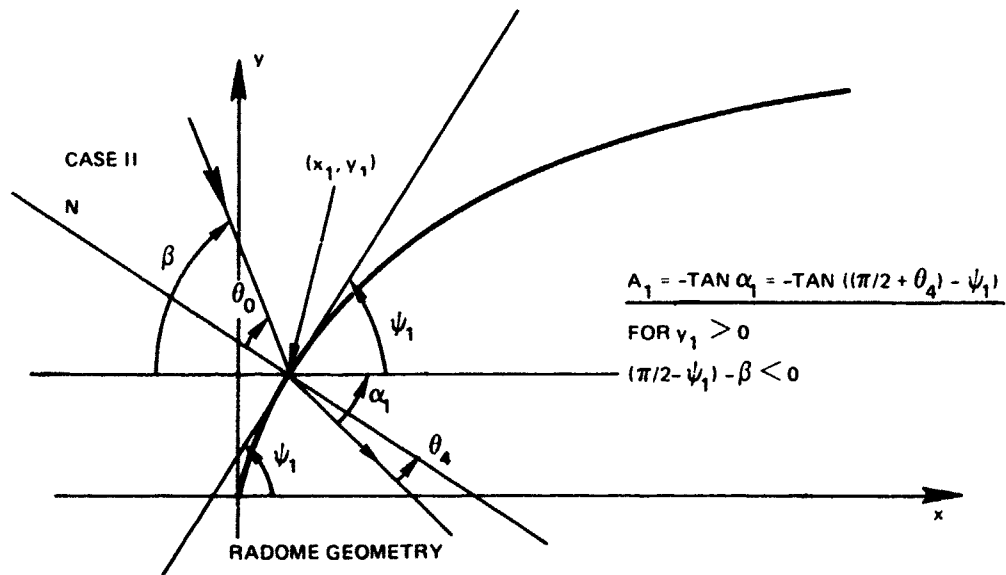
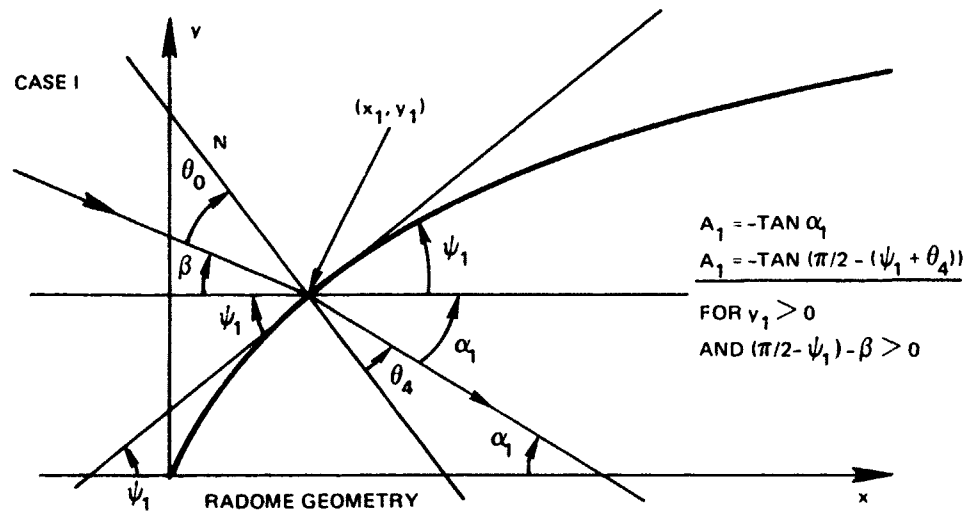
$$\phi = \phi_D - \phi_p,$$

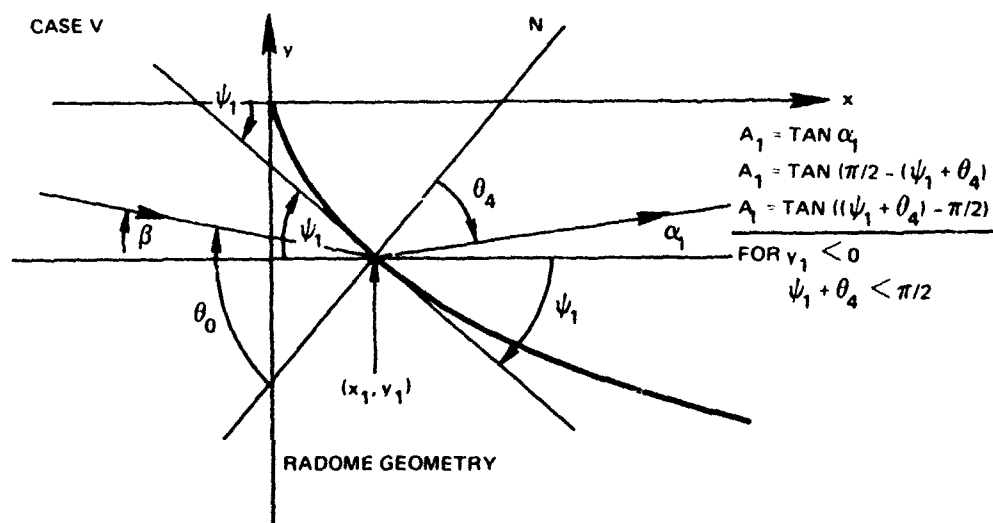
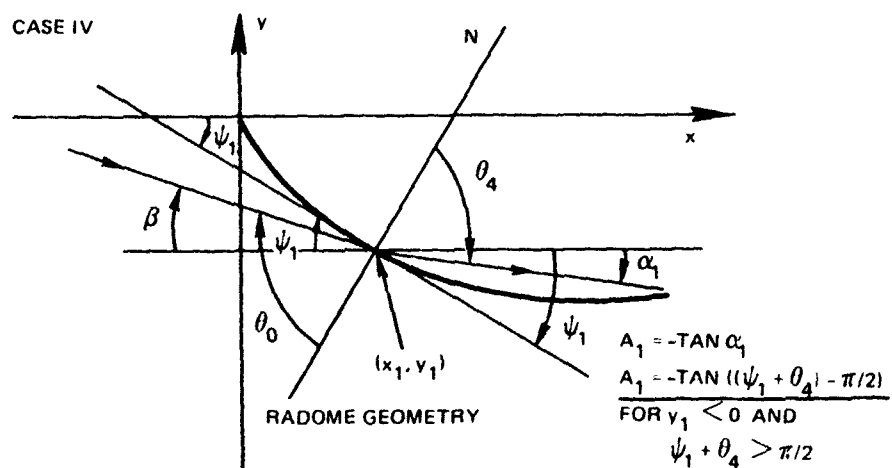
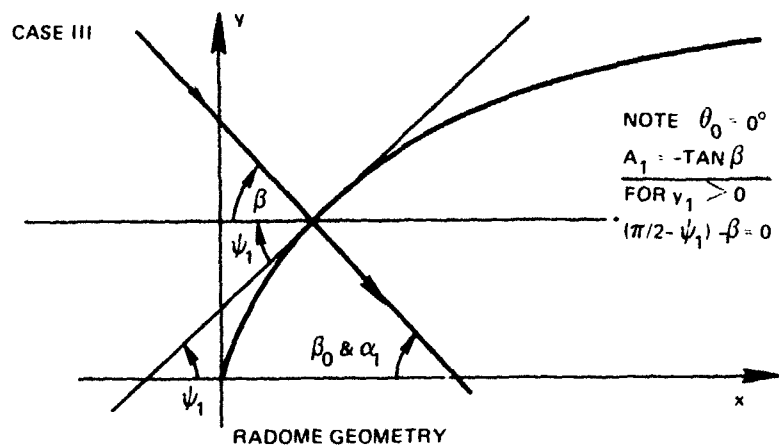
where ϕ_D is phase due to dielectric (computed in a subroutine)

II. LENS GEOMETRY (SEE FIG A2)

- A. Given β and x_1 , compute $y_1, \theta_0 - \theta_3$ and ψ_1 as before.
- B. Computation of A_1 - slope of ray through lens. ($\alpha_1 = \tan^{-1} A_1$)

$$\theta_4 = \sin^{-1} \left(\sqrt{\frac{\epsilon_3}{\epsilon_1}} \sin \theta_3 \right) \quad \text{by Snell's Law}$$





Summary for A_1

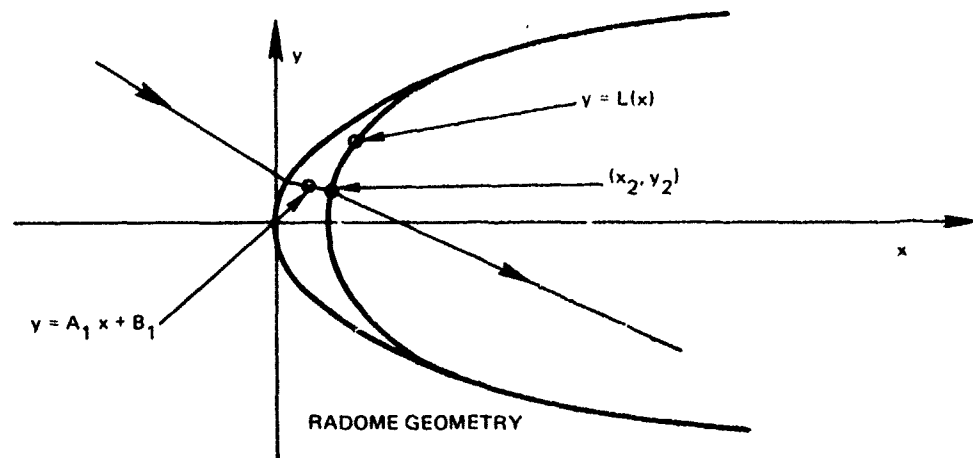
$$A_1 = \left\{ \begin{array}{ll} -\tan [\pi/2 - (\psi_1 + \theta_4)] & \text{Case I } (\pi/2 - \psi_1) - \beta > 0 \\ -\tan [(\pi/2 + \theta_4) - \psi_1] & \text{Case II } (\pi/2 - \psi_1) - \beta < 0 \\ -\tan \beta & \text{Case III } (\pi/2 - \psi_1) - \beta = 0 \\ -\tan [(\psi_1 + \theta_4) - \pi/2] & \text{Cases IV \& V } y_1 < 0 \end{array} \right\} \quad y_1 > 0$$

Then the equation of the line for the ray passing through the lens is:

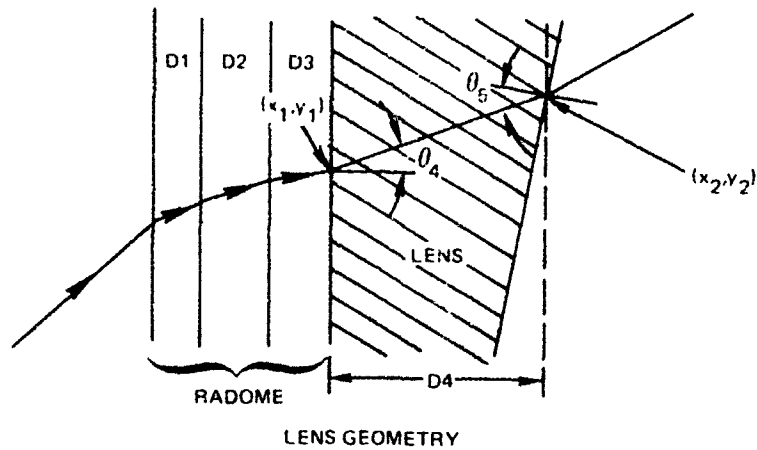
$$y = A_1 x + B_1 \quad \text{where } B_1 = y_1 - A_1 x_1.$$

C. Computation of point where ray hits inner face of lens, point (x_2, y_2)

Coordinate x_2 is found by solving simultaneously the equation for the line of the ray through the lens ($y = A_1 x + B_1$) and the lens equation ($y = L(x)$). In the program this will be done by a function routine. Then $y_2 = A_1 x_2 + B_1$



D. Computation of apparent thickness of lens, D4.



$$D4 = \sqrt{(x_2 - x_1)^2 + (y_2 - y_1)^2} * \cos \theta_4.$$

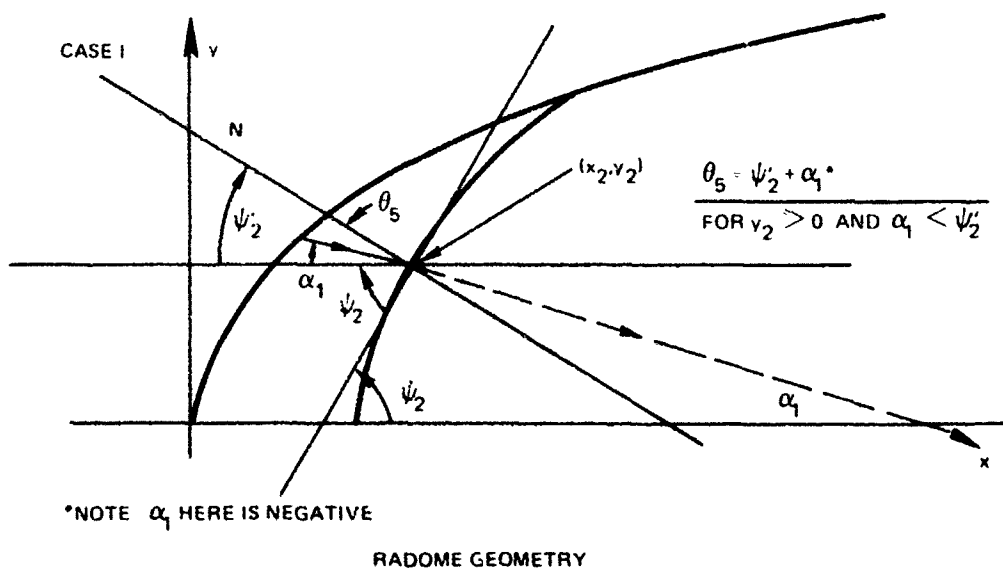
E. Computation of incident angle on inner face of lens, θ_5 .

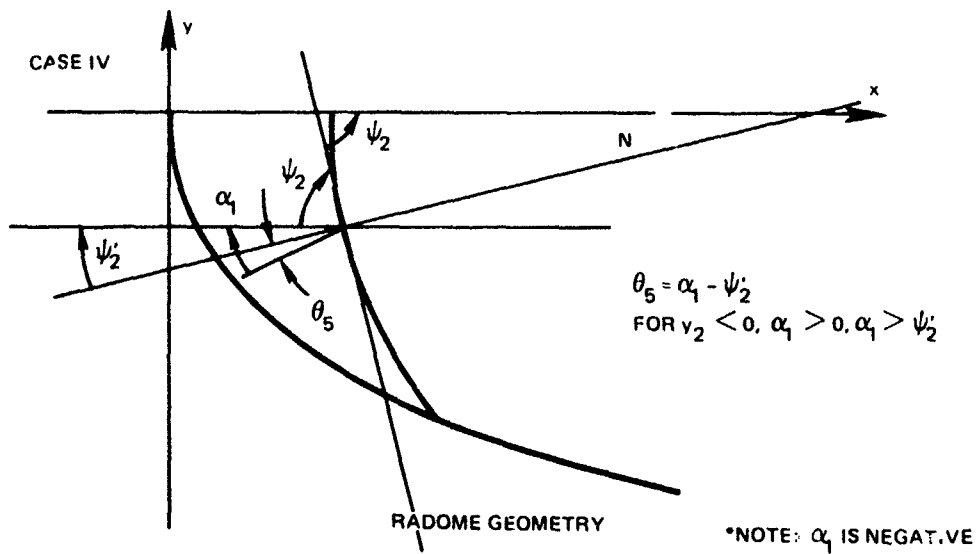
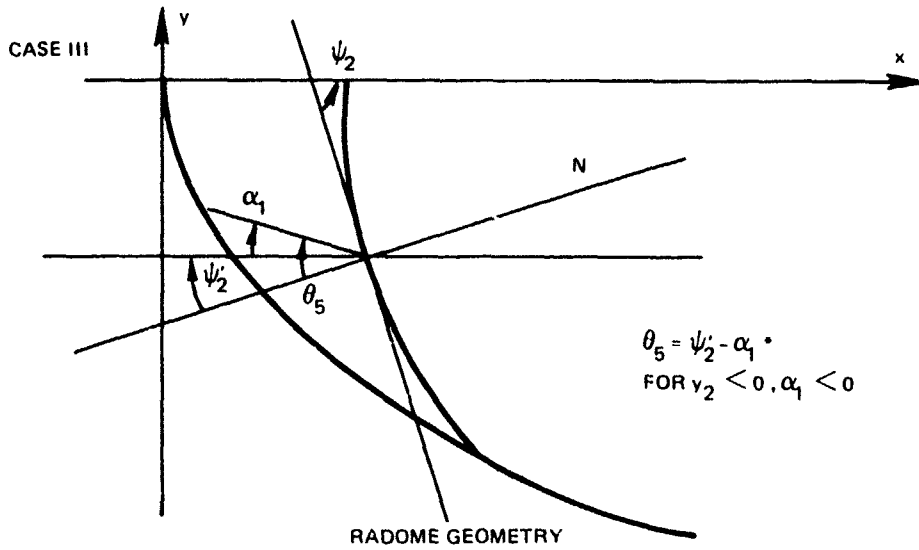
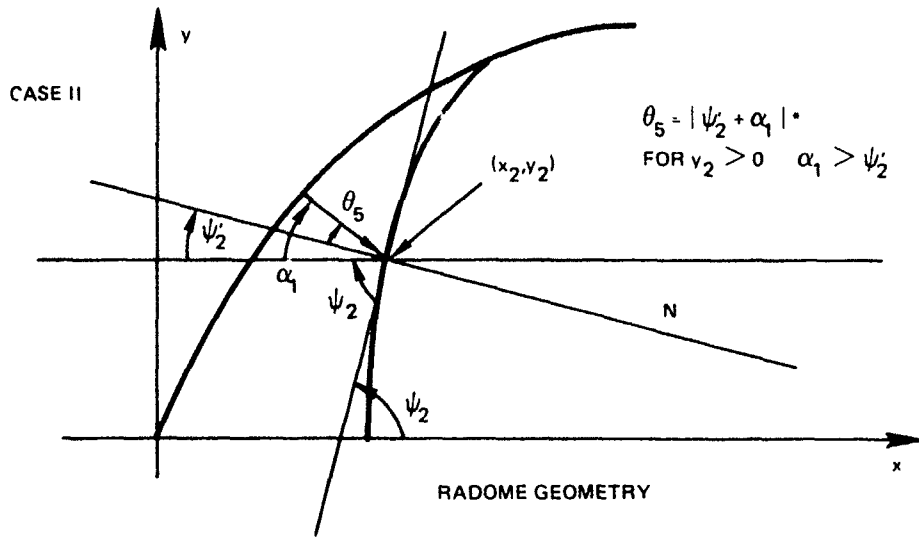
Note: θ_5 is always positive

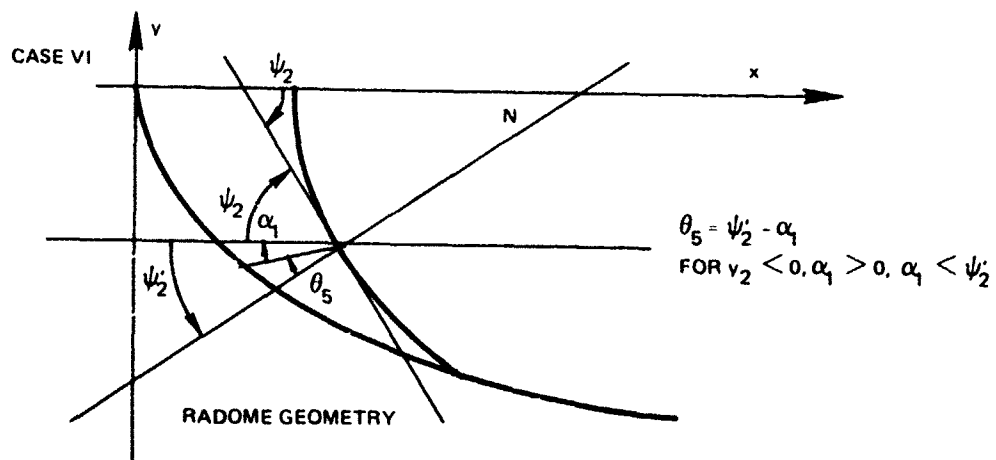
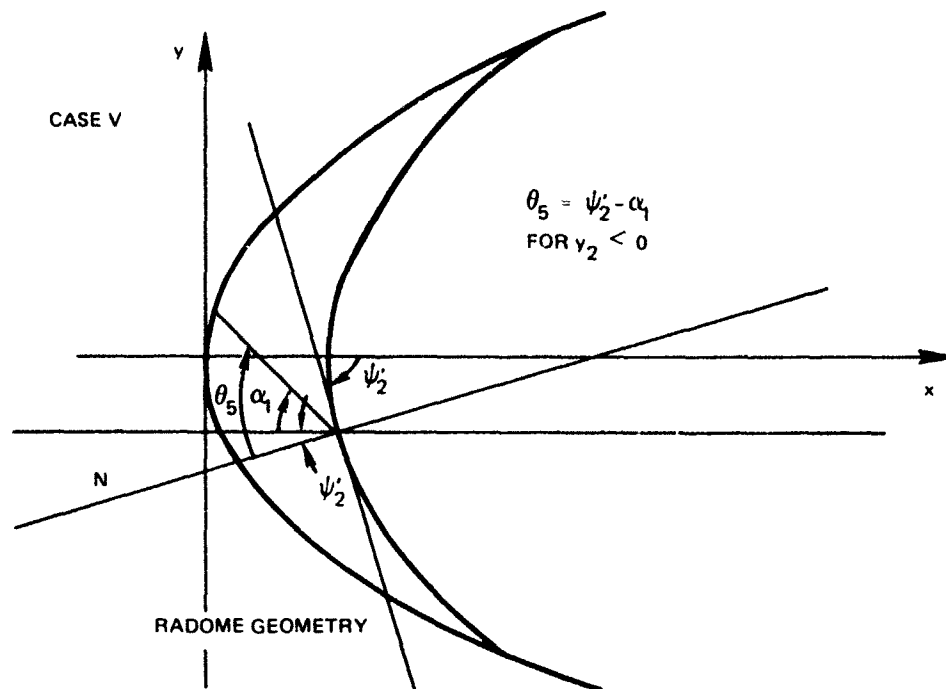
First, compute the slope angle (ψ_2) of the lens equation at point (x_2, y_2) :

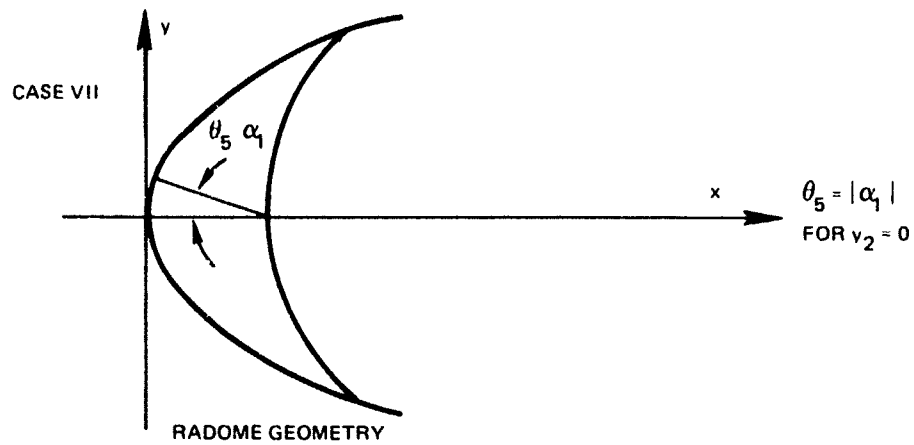
$$\psi_2 = \tan^{-1} L'(x_2)$$

$$\text{let } \psi'_2 = \pi/2 - \psi_2.$$









Summary for θ_5

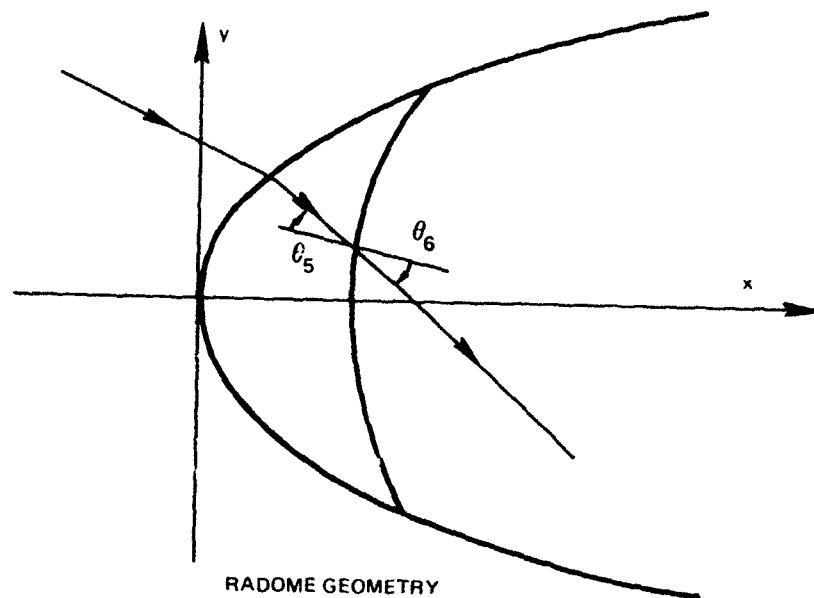
$$\theta_5 = \begin{cases} \text{abs}(\psi'_2 + \alpha_1) & \text{Cases I \& II} & y_2 > 0 \\ \text{abs}(\alpha_1) & \text{Case VII} & y_2 = 0 \\ \text{abs}(\psi'_2 - \alpha_1) & \text{Cases III, IV, V \& VI} & y_2 < 0 \end{cases}$$

Note: The above cases also take into account the case in which the ray is normally incident on the inside of the lens ($\theta_5 = 0$).

E. Computation of exit angle from lens, θ_6

By Snell's Law: $\theta_6 = \sin^{-1} \left(\sqrt{\epsilon_{\text{lens}}} \sin \theta_5 \right)$.

Note that total internal reflection occurs if $\sqrt{\epsilon_{\text{lens}}} \sin \theta_5 \geq 1.0$. In this case ignore this ray.



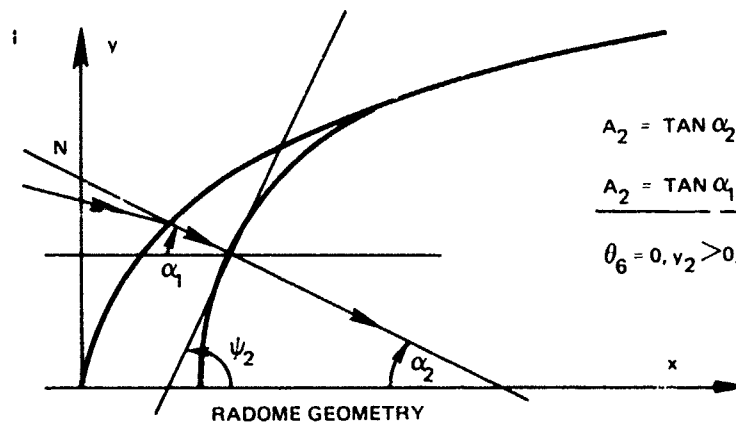
F. Computation of equation of ray line from lens to antenna: $y = A_2 x + B_2$

NOTE: ALL ANGLES ARE SIGNLESS EXCEPT α_1 AND α_2

$\alpha > 0 \Rightarrow$ POSITIVE SLOPE

$\alpha < 0 \Rightarrow$ NEGATIVE SLOPE

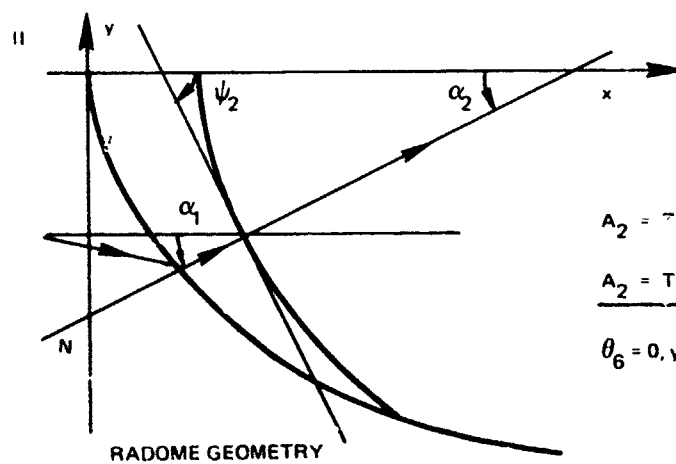
$$\psi'_2 = \pi/2 - \psi_2$$



$$A_2 = \tan \alpha_2$$

$$A_2 = \tan \alpha_1$$

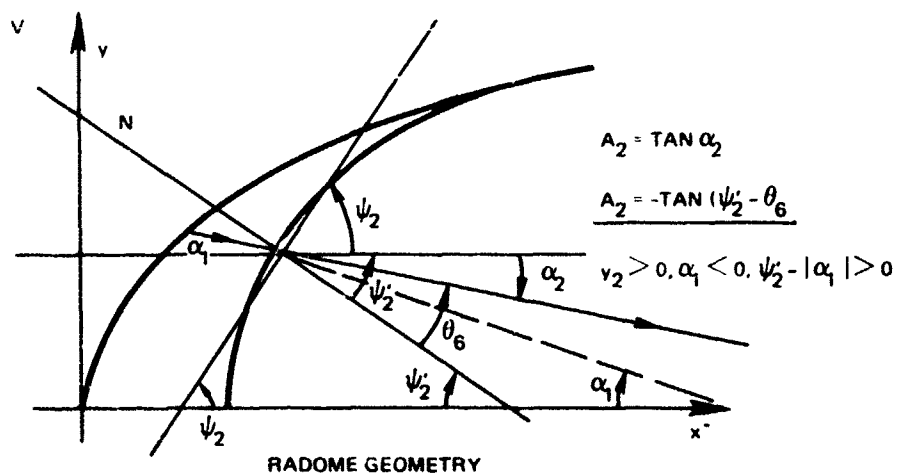
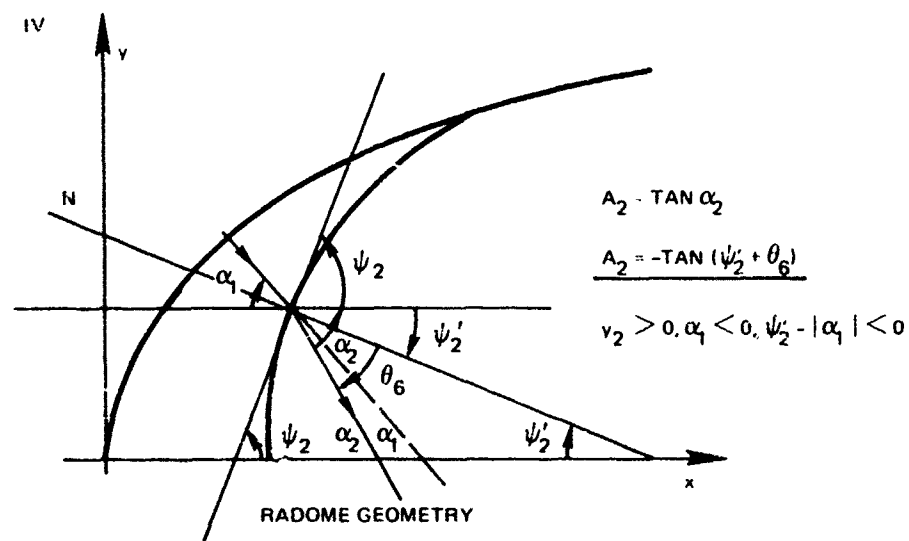
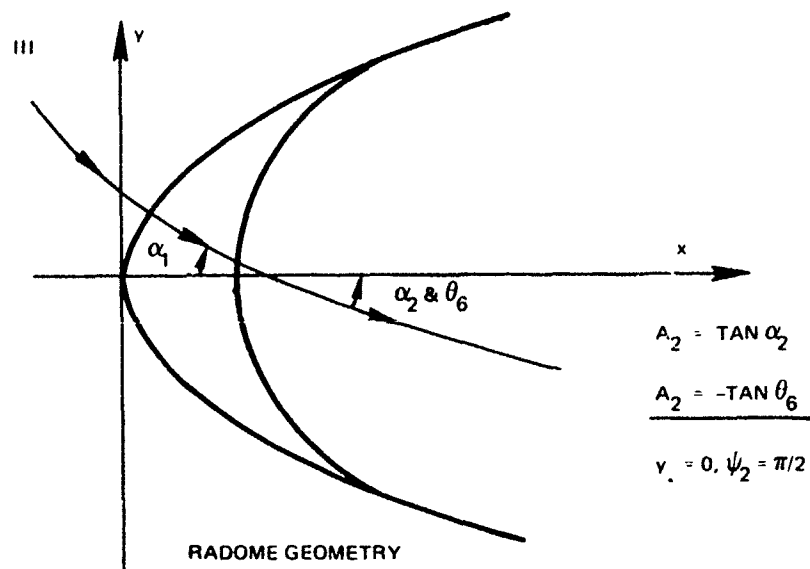
$$\theta_6 = 0, v_2 > 0, \alpha_1 < 0, \psi'_2 - |\alpha_1| = 0$$

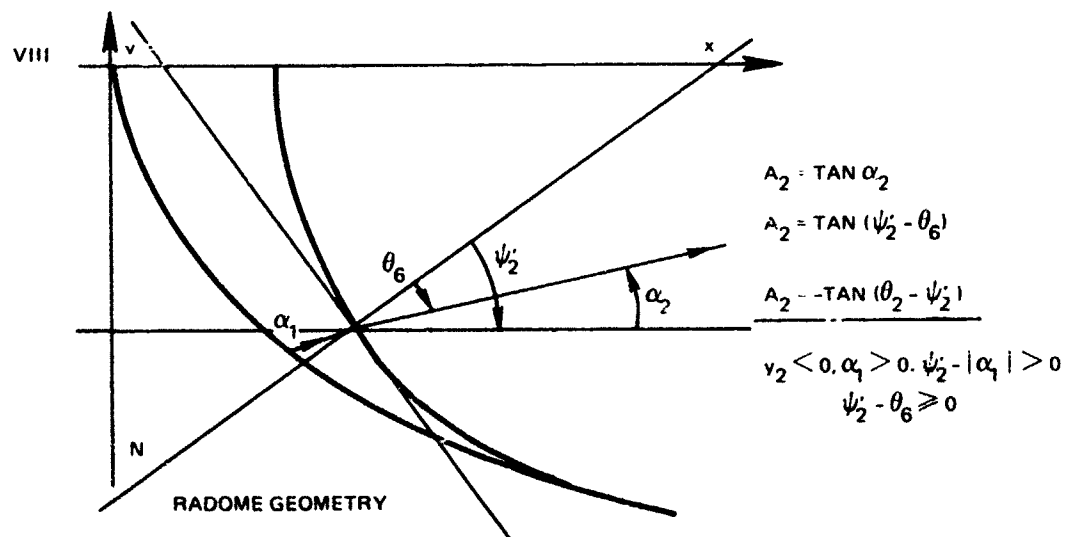
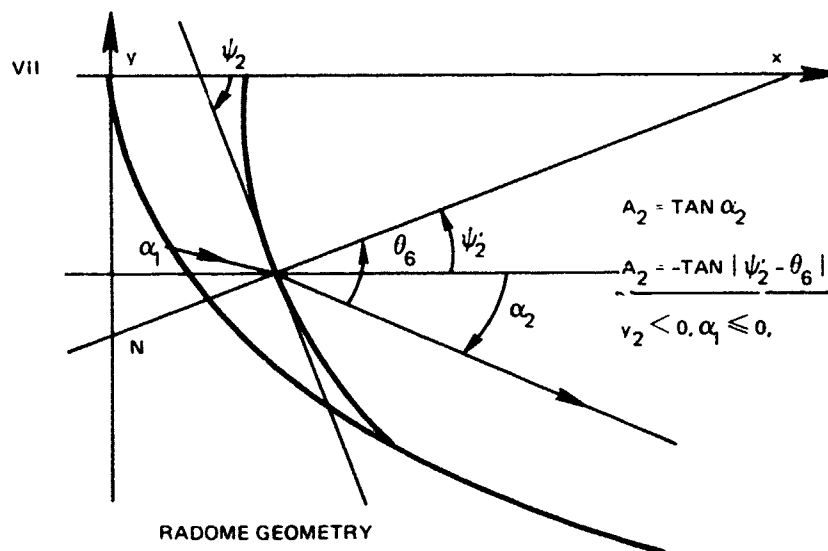
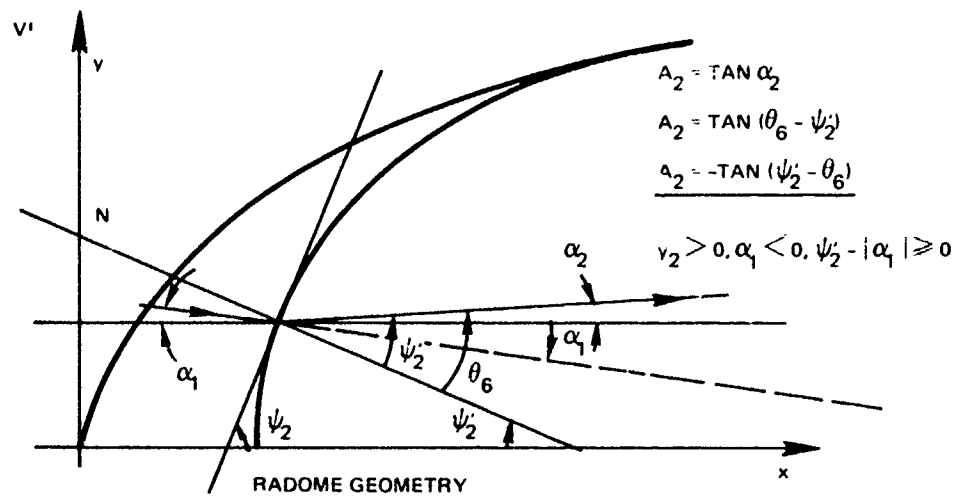


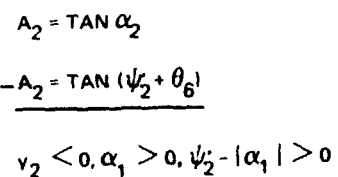
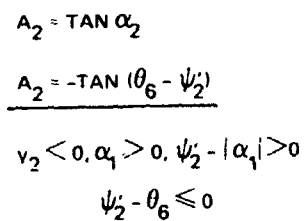
$$A_2 = -\tan \alpha_2$$

$$A_2 = \tan \alpha_1$$

$$\theta_6 = 0, v_2 < 0, \alpha_1 > 0, \psi'_2 - |\alpha_1| = 0$$







$$A_2 = \begin{cases} \text{I} & \tan \alpha_2 & y_2 > 0, \alpha_1 < 0, \psi'_2 - |\alpha_1| = 0, \theta_6 = 0 \\ \text{II} & \tan \alpha_2 & y_2 < 0, \alpha_1 > 0, \psi'_2 - |\alpha_1| = 0, \theta_6 = 0 \\ \text{III} & -\tan \theta_6 & y_2 = 0, \alpha_2 < 0, \psi_2 = \pi/2 \\ \text{IV} & -\tan(\psi'_2 + \theta_6) & y_2 > 0, \alpha_1 < 0, \psi'_2 - |\alpha_1| < 0 \\ \text{V} & \tan(\theta_6 - \psi'_2) & y_2 > 0, \alpha_1 < 0, \psi'_2 - |\alpha_1| > 0 \\ \text{VI} & \tan(\theta_6 - \psi'_2) & y_2 > 0, \alpha_1 < 0, \psi'_2 - |\alpha_1| \geq 0 \\ \text{VII} & -\tan|\psi'_2 - \theta_6| & y_2 < 0, \alpha_1 \leq 0 \\ \text{VIII} & \tan(\psi'_2 - \theta_6) & y_2 < 0, \alpha_1 > 0, \psi'_2 - |\alpha_1| > 0, \psi'_2 - \theta_6 \geq 0 \\ \text{IX} & \tan(\psi'_2 - \theta_6) & y_2 < 0, \alpha_1 > 0, \psi'_2 - |\alpha_1| > 0, \psi'_2 - \theta_6 \leq 0 \\ \text{X} & \tan(\psi'_2 + \theta_6) & y_2 < 0, \alpha_1 > 0, \psi'_2 - |\alpha_1| < 0 \end{cases}$$

$$A_2 = \begin{cases} \tan \alpha_2 & \theta_6 = 0 & \text{Cases I \& II} \\ -\tan \theta_6 & y_2 = 0 & \text{Case III} \\ -\tan|\psi'_2 - \theta_6| & y_2 < 0, \alpha_1 \leq 0 & \text{Case VII} \\ \operatorname{sgn}(\alpha_1) \tan(\psi'_2 + \theta_6) & \psi'_2 - |\alpha_1| < 0 & \text{Cases IV \& X} \\ \tan(\psi'_2 - \theta_6) & \psi'_2 - |\alpha_1| \geq 0, y_2 < 0 & \text{Cases VIII \& IX} \\ \tan(\theta_6 - \psi'_2) & \psi'_2 - |\alpha_1| \geq 0, y_2 > 0 & \text{Cases V \& VI} \end{cases}$$

$$\text{Then } B_2 = y_2 - A_2 * x_2.$$

G. Computation of point at which ray hits antenna (x_3, y_3)

$$1. \text{ Equation of antenna line } y_1 = AA * x + BA$$

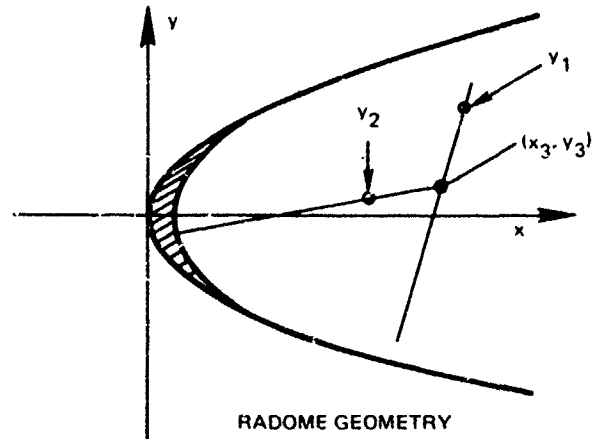
2. Equation of ray from lens to antenna

$$y_2 = A_2 * x + B_2$$

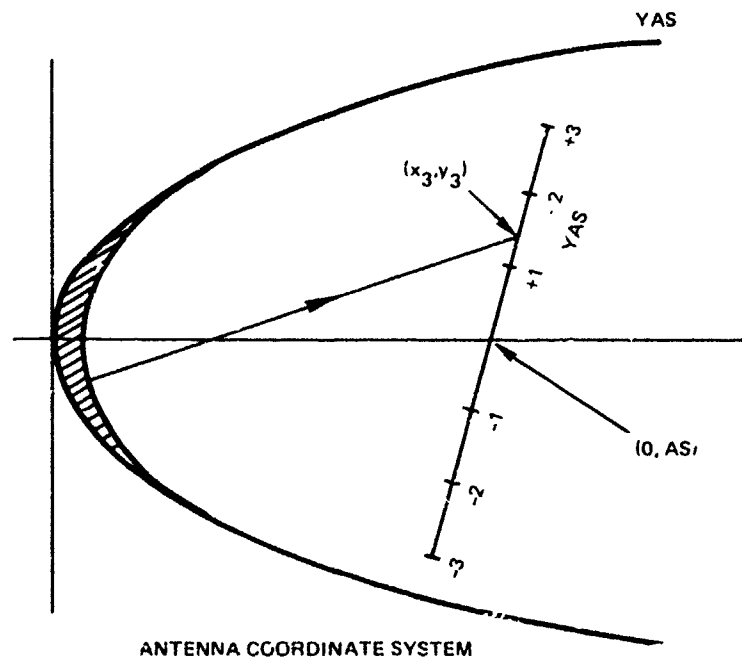
$$\therefore AA x_3 + BA = A_2 x_3 + B_2$$

$$x_3 = \frac{(BA - B_2)}{(A_2 - AA)}$$

$$y_3 = AA x_3 + BA$$



H. Computation of antenna coordinate YAS



$$YAS = \text{sgn}(y_3) \sqrt{(x_3 - AS)^2 + y_3^2}$$

I. Computation of ray path difference, ΔP (see fig A2)

$$x'_3 = \frac{(x_2/AA + y_2 - BA)}{(AA + 1/AA)}$$

$$y'_3 = AA * x'_3 + BA$$

$$L_1 = \sqrt{(x_2 - x_3)^2 + (y_2 - y_3)^2}$$

$$L_2 = \sqrt{(x_2 - x'_3)^2 + (y_2 - y'_3)^2}$$

$$\Delta P = (L_1 - L_2) * \text{INTM (converted to metres).}$$

J. Computation of total phase delay ϕ

1. Compute phase due to dielectric, ϕ_D , from subroutine.

2. Compute phase due to path difference, ϕ_P

$$\phi_P = \left(\frac{2\pi}{\lambda} \right) \left(\sum d_i \right) (\cos \theta_o) + \Delta P$$

Then $\phi = \phi_D - \phi_P$.

APPENDIX B: BORESIGHT ERROR DATA

This appendix presents a representative set of boresight error data obtained from the NELC two-dimensional ray-tracing radome program. All radomes modeled were 8 inches in diameter (d) and 18 inches long (L). Two radome shapes were used, the tangent ogive and the power series type. The equations used for the two shapes were as follows:

$$\begin{aligned} \text{Tangent ogive} \quad y &= (R^2 - (L-x)^2)^{1/2} - a \\ \text{where } R &= \frac{L^2}{d} + \frac{d}{4} \quad \& \quad a = \frac{L^2}{d} - \frac{d}{4} \\ \\ \text{Power series} \quad y &= d/2 (x/L)^{1/2} \end{aligned}$$

The equations for the lenses used in power series radomes were of the form

$$y = s(x-t)^{1/2},$$

where

t is the thickness at the nose

and

s dictates the distance from the nose to the edge of the lens.

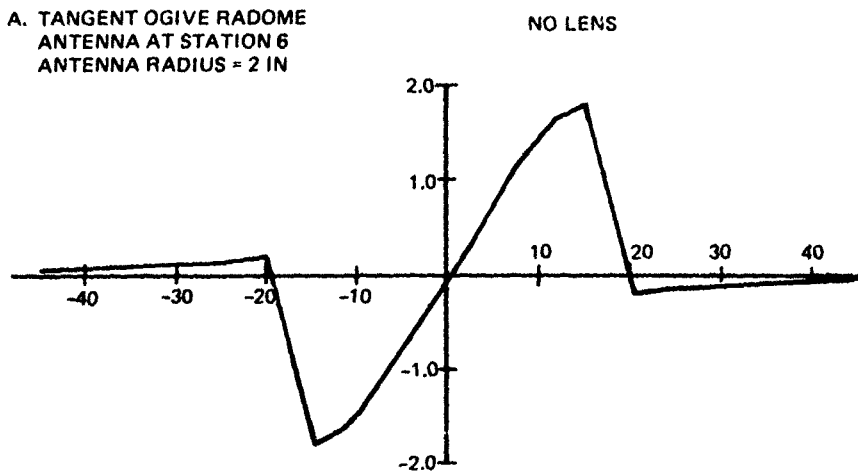
In all cases the radome was of three-layer construction with the following parameters:

	Thickness (in)	Dielectric Constant
Layer 1 (outer)	0.012	2.7
Layer 2	0.040	2.9
Layer 3	0.025	4.2

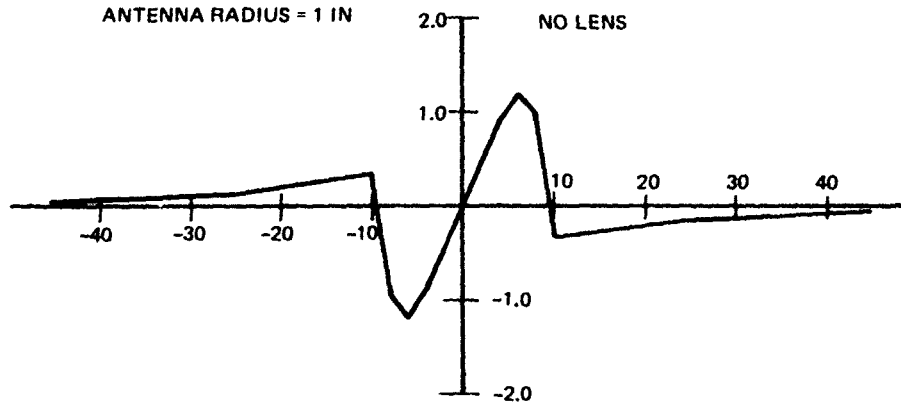
These parameters were chosen to give the broadest frequency band while maintaining structural reliability.

There are three sets of data - tangent ogive, power series, and phase compensated or lensed power series. It was found that the tangent ogive radome had better boresight error characteristics with the antenna placed toward the base of the radome. The power series radome performed better with the antenna placed closer to the nose. With a lensed power series radome the shape of the lens depended on the antenna configuration. However, with the proper lens, the compensated power series radome gave better performance than either the tangent ogive or the clean power series.

A. TANGENT OGIVE RADOME
ANTENNA AT STATION 6
ANTENNA RADIUS = 2 IN



B. TANGENT OGIVE RADOME
ANTENNA AT STATION 6
ANTENNA RADIUS = 1 IN



C. TANGENT OGIVE RADOME
ANTENNA AT STATION 12
ANTENNA RADIUS = 2 IN

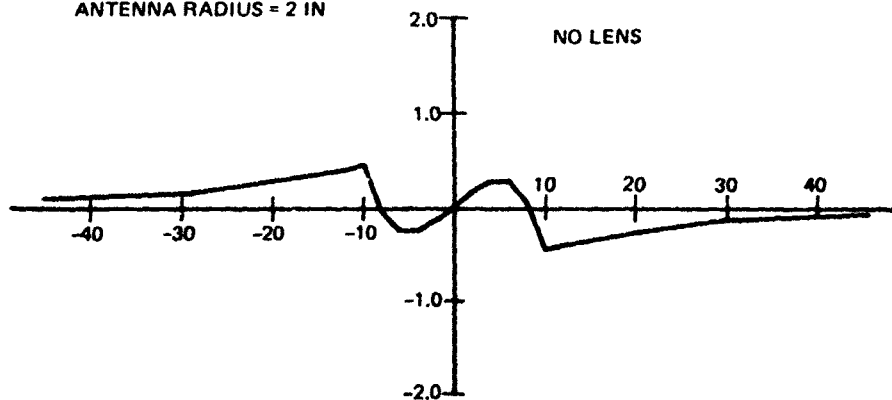


Figure B1. Boresight error (deg) vs look angle (deg) tangent ogive radome.

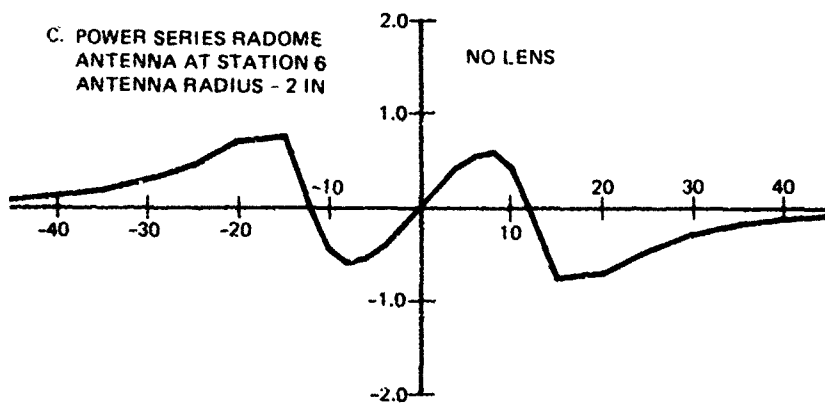
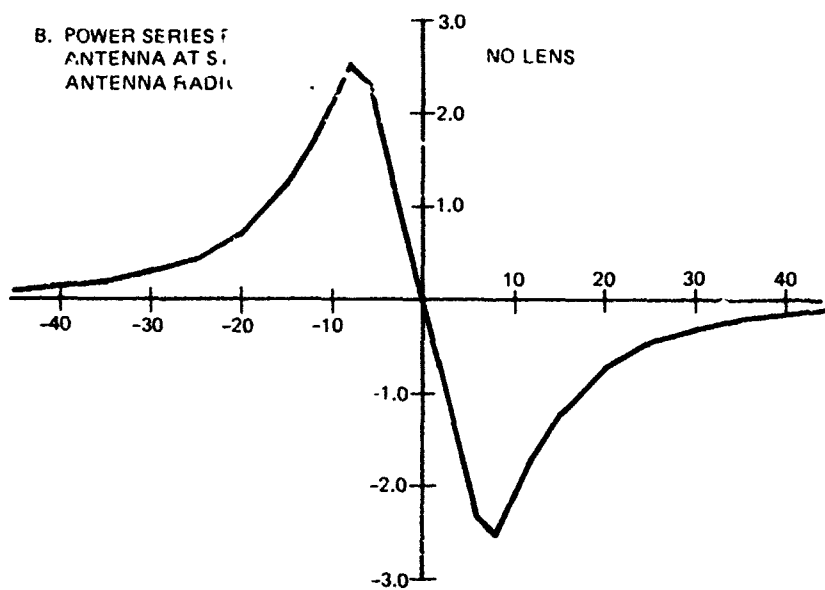
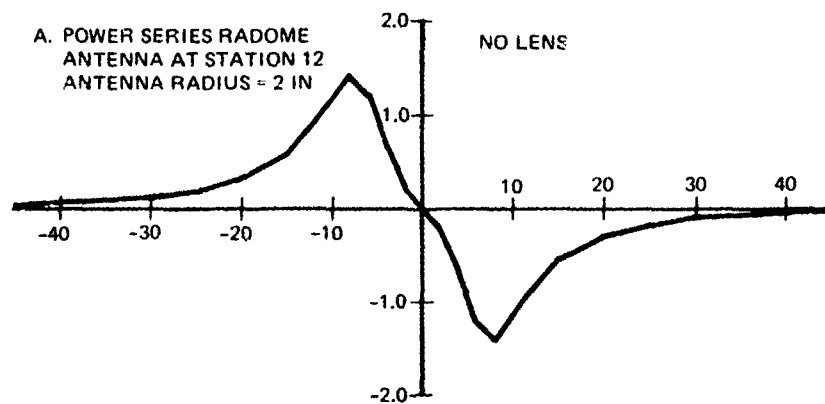


Figure B2. Boresight error (deg) vs look angle (deg), power series radome.

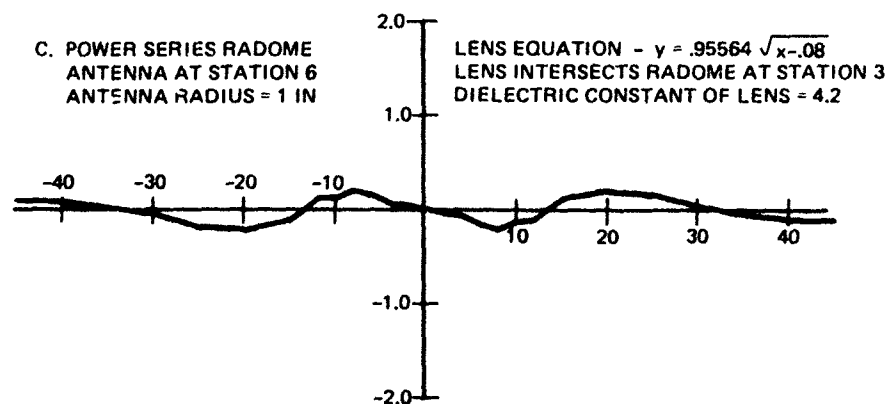
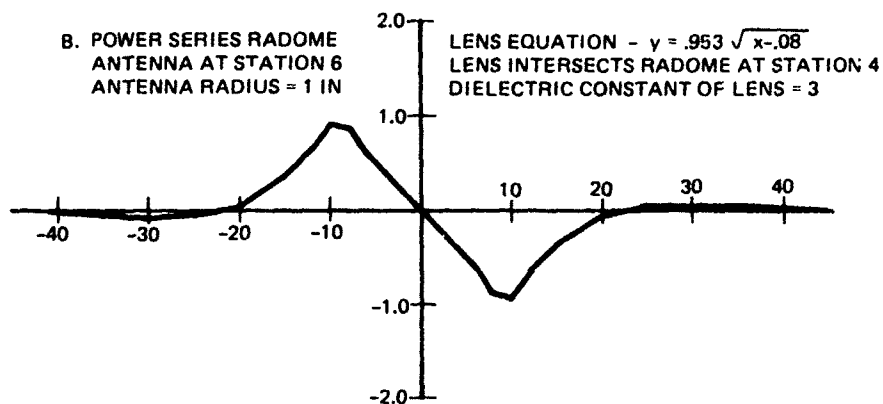
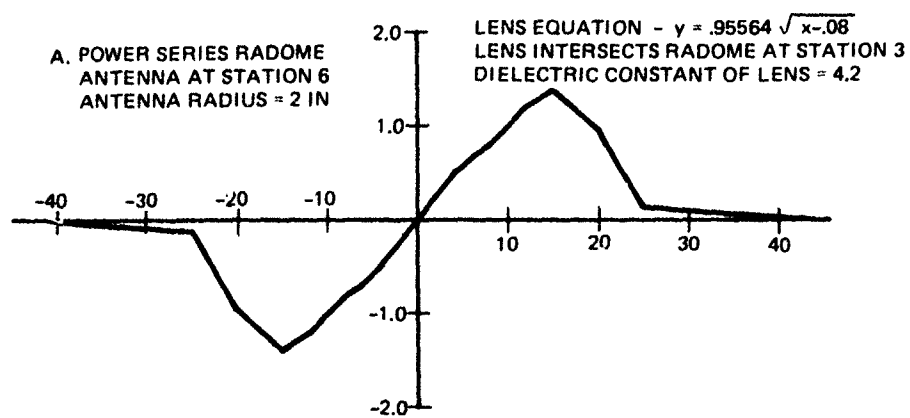


Figure B3. Boresight error (deg) vs look angle (deg), lensed radome.

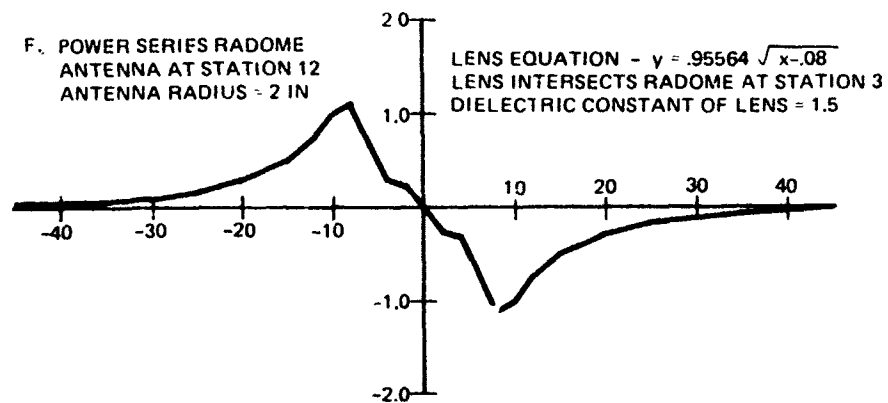
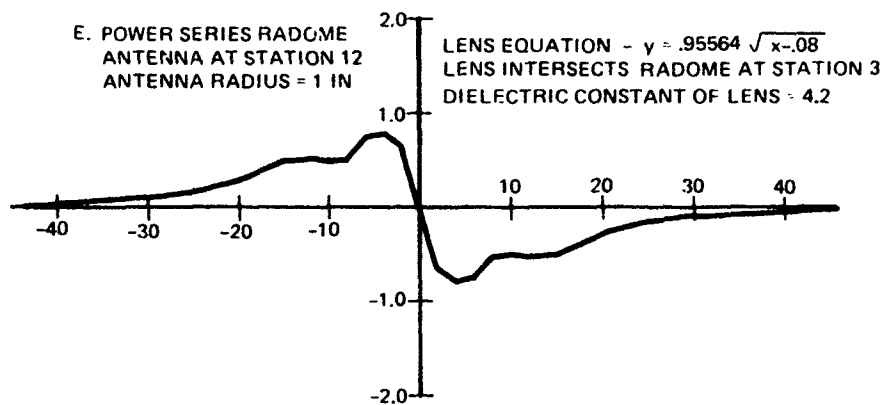
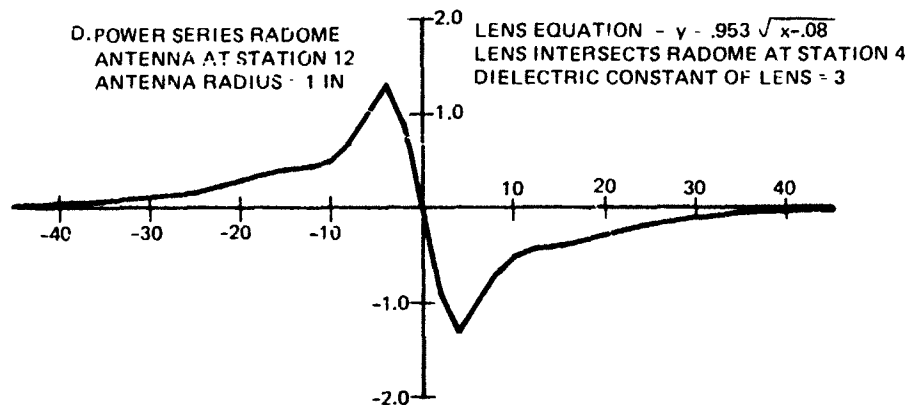


Figure B3. (Continued).

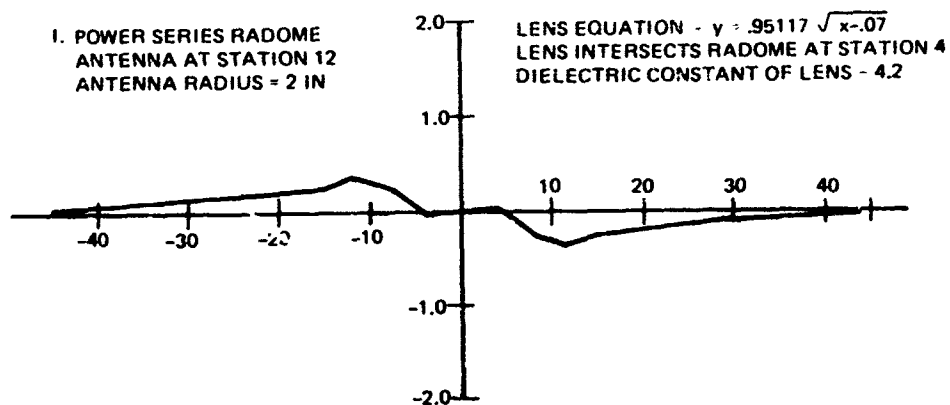
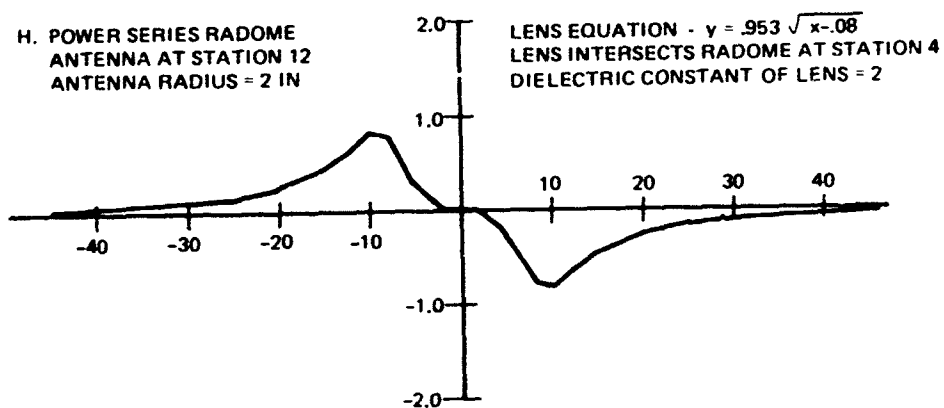
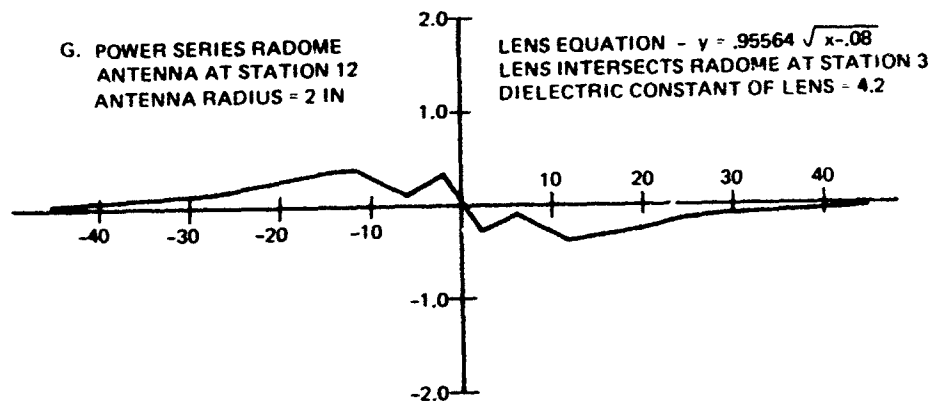
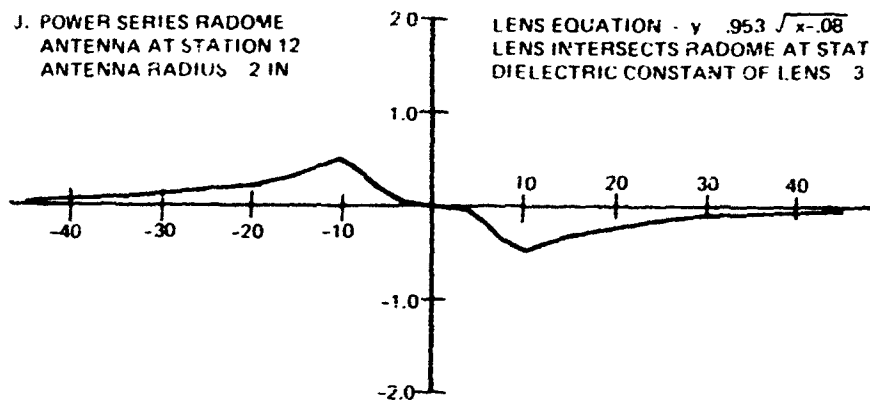


Figure B3. (Continued).

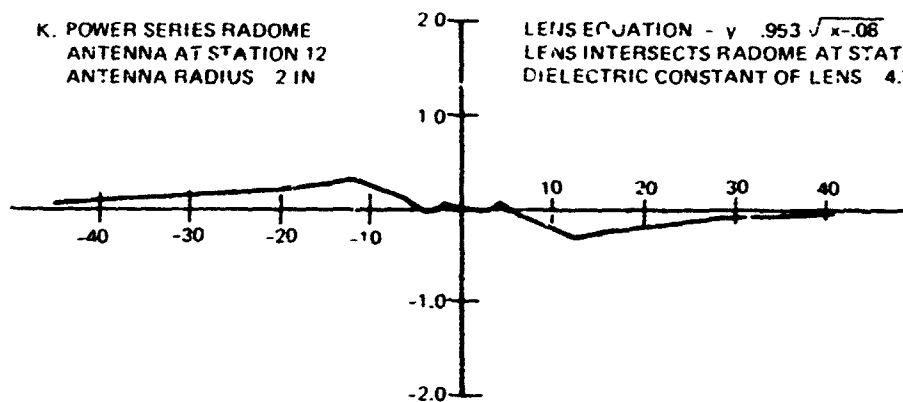
J. POWER SERIES RADOME
ANTENNA AT STATION 12
ANTENNA RADIUS 2 IN

LENS EQUATION - $y = .953 \sqrt{x-.08}$
LENS INTERSECTS RADOME AT STATION 4
DIELECTRIC CONSTANT OF LENS 3



K. POWER SERIES RADOME
ANTENNA AT STATION 12
ANTENNA RADIUS 2 IN

LENS EQUATION - $y = .953 \sqrt{x-.08}$
LENS INTERSECTS RADOME AT STATION 4
DIELECTRIC CONSTANT OF LENS 4.2



L. POWER SERIES RADOME
ANTENNA AT STATION 12
ANTENNA RADIUS 2 IN

LENS EQUATION - $y = .94859 \sqrt{x-.085}$
LENS INTERSECTS RADOME AT STATION 7
DIELECTRIC CONSTANT OF LENS 4.2

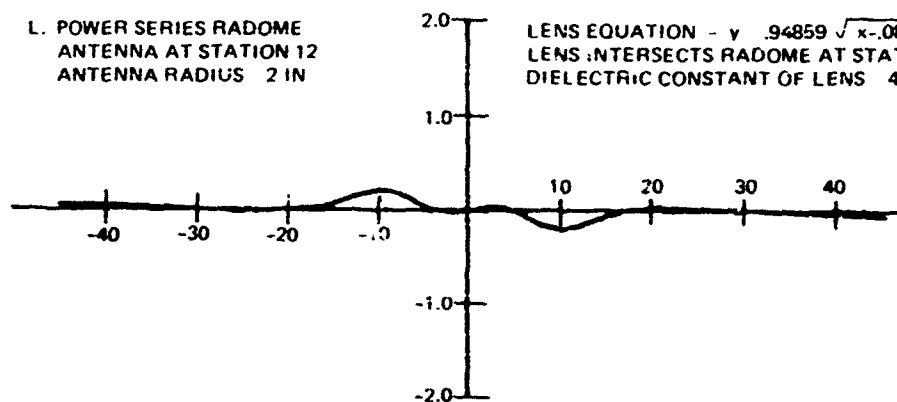


Figure B3. (Continued).

APPENDIX C: ABLATION MODEL AND TEST DATA FOR AVCOAT 8027

Ablation data for AVCOAT 8027 obtained in the AVCO Model 500 and 10 Megawatt Plasma Arc facilities are presented herein. In addition, it is shown how these data yield parameters which can be used to analytically simulate the ablative behavior of AVCOAT 8027. Table C1 gives the 10 Megawatt Arc test conditions and AVCOAT 8027 wedge specimen response data. The Model 500 Arc test data are shown in table C2. The ablation test specimen configurations are shown in figure C1.

AVCOAT 8027 is noncharring, shear insensitive, flexible epoxy resin which decomposes at a nearly constant temperature of 1200°R during ablation (see the TGA data in figure C2), to yield gaseous products. Assuming quasi-steady conditions, the surface heat balance equation describes ablation at the stagnation point:

$$\frac{\dot{q}_c (h_s - h_w)}{h_s \rho_s} = Q^* = H_d + C_p (T_a - T_o) + R (h_s - h_w) \quad (C1)$$

The nomenclature definition is given in table C3.

Q^* , the thermochemical heat of ablation, was calculated from the Model 500 and 10 Megawatt Arc test data and plotted vs the enthalpy potential, $h_s - h_w$, in figure C3. The linear fit of the Q^* data in figure C3 justifies the use of the linear model, equation (C1). (Although the 10 Megawatt Arc data show some scatter, they are still basically consistent with the Model 500 Arc test data.) From the Q^* data plot of figure C3 the effective heat of decomposition, H_d , and the transpiration coefficients η_{LS} and η_{TURB} may be obtained. Specifically, H_d is obtained by setting the right side of equation (C1) equal to the Q^* intercept at $h_s - h_w = 0$.

$$\begin{aligned} Q^*(h_s = h_w) &= H_d + C_p (T_a - T_o) \\ 1100 &= H_d + .41 (1200 - 540) \\ H_d &= 829 \text{ Btu/lbm} \end{aligned}$$

The increasing Q^* values with increasing $(h_s - h_w)$ are due to the blocking effect of the ablation products. This effect is proportional to the transpiration coefficient, η . The laminar stagnation transpiration coefficient, η_{LS} , may be obtained directly as the slope of the laminar Model 500 Arc test data and has a value of 0.45. Although the turbulent flat plate flow coefficient, η_{TURB} , cannot be obtained from the 10 Megawatt Arc turbulent wedge test data (due to the data scatter over the narrow range of enthalpies tested), η_{TURB} can be defined as a function of the laminar coefficient by the following equations (ref C1).

$$\eta_{LS} = 0.603 \left(\frac{m_a}{m_i} \right)^{1/3} \quad (C2)$$

and

$$\eta_{TURB} = 0.344 \left(\frac{m_a}{m_i} \right)^{1/3} \quad (C3)$$

Combining these equations yields

$$\eta_{\text{TURB}} = 0.473 (\eta_{\text{LS}})^{.3} = 0.34 \quad (\text{C4})$$

REFERENCE

- C1. Munson, TR. et al. "An Advanced Analytical Program For Charring Ablators." AVSSD-0172-67-RR, vol 1

TABLE C1. 10-MEGAWATT ARC TURBULENT WEDGE TEST DATA
OF AVCOAT 8027-B SPECIMENS.

10 MW Arc Run	Material Density (lb/ft ³)	Calorimeter Heat Flux (Btu/ft ² s)	Stagnation Enthalpy (Btu/lbm)	Shear Stress (lb/ft ²)	Surface Temp (°R)	Time Test (s)	Ablation Rate		Q*-Thermo- chemical Heat of Ablation (Btu/lbm)
							Mass Loss (q/s)	Recession Surface (in/s)	
8276	75	262	1422	33	1200	5.1	1.35	0.030	1174
8277	75	264	1422	34	1200	3.1	1.61	0.035	1023
8278	75	233	1252	33	1200	5.1	1.16	0.022	1395
8281	75	156	813	32	1200	5.1	0.65	0.014	1312
8382	75	340	1760	36	1200	2.0	1.77	0.035	1375
8383	75	340	1760	36	1200	3.0	1.75	0.034	1407
8384	75	340	1760	36	1200	2.0	1.77	0.036	1314
8387	75	140	644	36	1200	4.0	0.48	0.009	1572
8388	75	140	644	36	1200	4.0	0.50	0.009	1538
8389	75	140	644	36	1200	4.0	0.45	0.009	1608

TABLE C2. MODEL 500 ARC TEST DATA OF
AVCOAT 8027 SPECIMENS.

Material Density (lb./ft. ³)	Cold Wall Heat Flux (Btu./ft. ² s)	Stagnation Enthalpy (Btu./lb)	Temperature Surface (°R)	Ablation Rate (in/s)	Thermochemical Heat of Ablation (Btu./lb)
74*	850	3864		0.044	2808
74*	1130	4238		0.055	3013
74*	1100	4942		0.049	3299
74*	1035	5085		0.043	3528
74*	1375	6497		0.050	4092
74*	1295	8239		0.043	4588
74*	1305	9934		0.036	5467
75	1186	10 080	1260	0.034	5290
75	840	4190	1260	0.048	2620
75	9648	8270	1260	0.046	4420

*2% by weight TiO₂ added

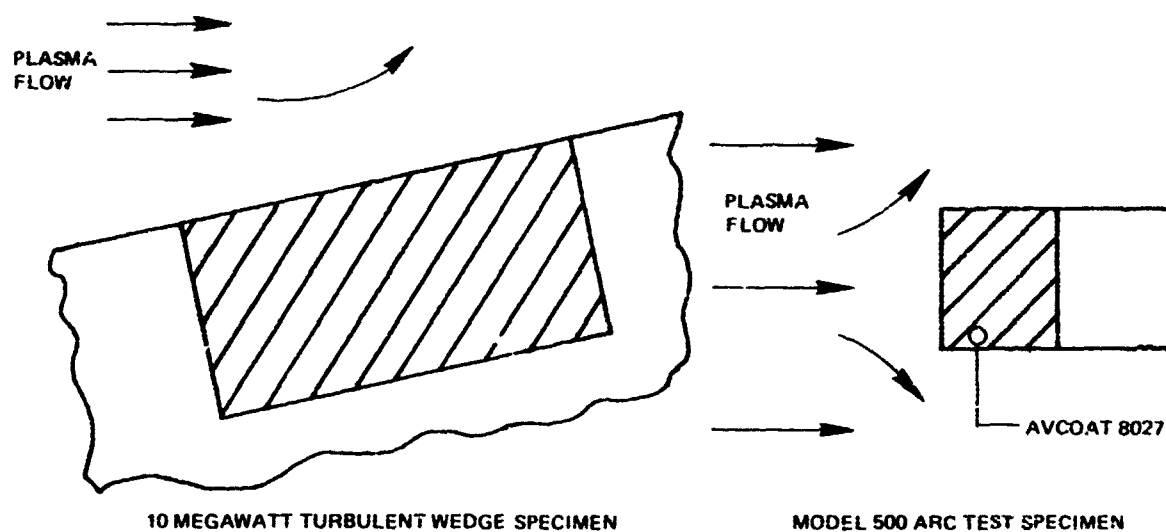


Figure C1. AVCOAT 8027 arc test specimen configurations.

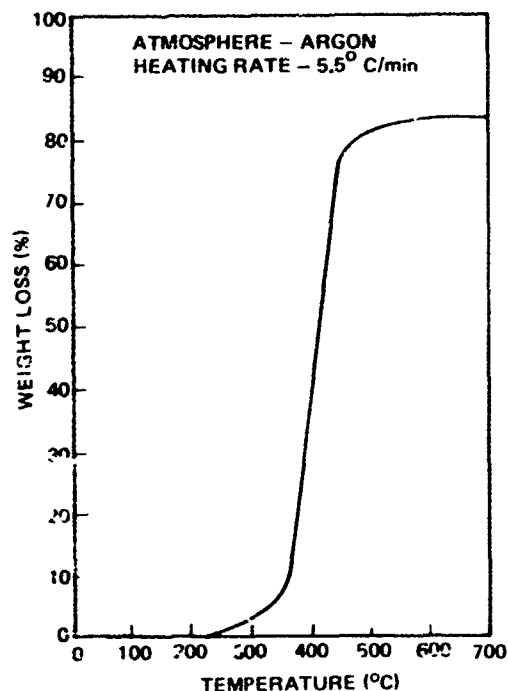


Figure C2. Thermogravimetric analysis of AVCOAT 8027.

TABLE C3.

<u>Parameter</u>		<u>Value</u>
Q^*	~ Thermochemical heat of ablation	
q_{cw}	~ Cold wall heat flux to specimen	
h_s	~ Stagnation enthalpy of plasma flow	
h_w	~ Enthalpy of plasma at the ablating surface	300 Btu/lbm
s	~ Surface recession rate of ablating specimen	τ
ρ	~ Specimen density	74 lb/ft ³
C_p	~ Specific heat of specimen	0.41 Btu/lbm [°] F
T_a	~ Ablation temperature	1200 [°] R
T_o	~ Initial temperature	540 [°] R
m_a	~ Molecular weight of air	29 lb/lb. mol
m_i	~ Molecular weight of ablated species (from Model 500 Test data)	70 lb/lb. mol
Ablation data analysis results:		
H_d	~ Effective heat of decomposition	829 Btu/lbm
η_{LS}	~ Laminar stagnation transpiration coefficient	0.45
η_{TURB}	~ Turbulent flat plate transpiration coefficient	0.34

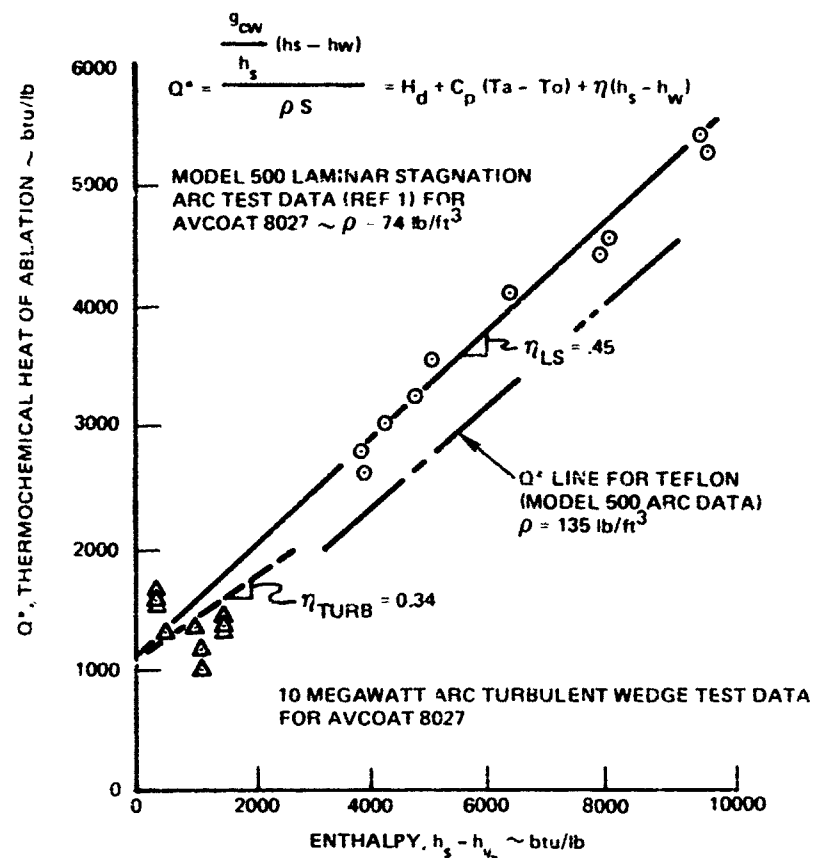


Figure C3. AVCO Model 500 and 10-megawatt plasma and ablation data on AVCOAT 8027.

INITIAL DISTRIBUTION LIST

DIRECTOR OF DEFENSE, RESEARCH
& ENGINEERING
WASHINGTON, DC 20301
C MC KINLEY
G BLACKSHAW

ASSISTANT SECRETARY OF THE NAVY (R&D)

CHIEF OF NAVAL OPERATIONS
WASHINGTON, DC 20350
NOP-506F
NOP-982E4

COMMANDER
NAVAL AIR SYSTEMS COMMAND
WASHINGTON, DC 20361
PMA-242
PMA-262
PMA-268
NAIR 360 (5)
NAIR 360F (5)
NAIR 50J2
CF BERSCH (2)

CHIEF OF NAVAL MATERIAL
WASHINGTON, DC 20360
NMAT-03
NMAT-0321

COMMANDER
NAVAL ELECTRONIC SYSTEMS COMMAND
WASHINGTON, DC 20361
PME-107

COMMANDER
NAVAL SEA SYSTEMS COMMAND
WASHINGTON, DC 20362
NSEA-65431

COMMANDER
NAVAL WEAPONS CENTER
CHINA LAKE, CA 93555
CODE 352 (BOB CORZINE)
CODE 3522 (GH WINKLER)
CODE 3522 (D SEIBEL)
CODE 3561 (D PUPCELL)

COMMANDER
NAVAL AIR DEVELOPMENT CENTER
WARMINSTER, PA 18974
JAMES R CHESNUT, CODE 20412
GEORGE TATNALL

OFFICE OF NAVAL RESEARCH
ARLINGTON, VA 20034
AM DINESS, CODE 4F1

COMMANDER
NAVAL SURFACE WEAPONS CENTER
WHITE OAK
SILVER SPRING, MD 20910
ROBERT I P VOISINET

AIR FORCE AVIONICS LABORATORY
WRIGHT-PATTERSON AFB, OH 45426
AE BLUME, DHM

AIR FORCE MATERIALS LABORATORY
WRIGHT-PATTERSON AFB, OH 45433
DONALD J EVANS

NAVAL DETACHMENT
AIR FORCE ELECTRONIC WARFARE CENTER
SAN ANTONIO, TX 78243
LCDR M OETINGER

USAF/RDQRM
WASHINGTON, DC 20330

AIR FORCE SYSTEMS COMMAND (DLCAW)
ANDREWS AFB, MD 20331

AIR FORCE ARMAMENT LABORATORY (DLM1)
EGLIN AFB, FL 32542 (4)

ARMY MISSILE COMMAND
REDSTONE ARSENAL
HUNTSVILLE, AL 35809
KENNETH N LETSON, DRSMI-RLA
CARLTON CASH, DRSMI-RER
WJ LINDBERG, DRSMI RE
DR WC MC CORKLE, DRSMI-RD

ARMY MATERIAL COMMAND
OFFICE OF MISSILE ELECTRONIC WARFARE
WHITE SANDS MISSILE RANGE, NM 88002
AMSEL-WLM MA

DEFENSE DOCUMENTATION CENTER
CAMERON STATION
ALEXANDRIA, VA 22314 (20)

ARMAMENT DEVELOPMENT & TEST CENTER
EGLIN AFB, FL 32542
CAPT BL MUNGER, SD 7

AVCO SYSTEMS DIVISION
LOWELL INDUSTRIAL PARK
LOWELL, MA 01720
GW CHRISTIANSEN
AJ PATRICK, JR

APL/JHU
JOHNS HOPKINS ROAD
LAUREL, MD 20910
RK FRAZER
LS WECKESSER

BOEING COMPANY
PO BOX 3999
SEATTLE, WA 98124
FA SIMPSON

AIRBORNE INSTRUMENTS LABORATORY
A DIVISION OF CUTLER-HAMMER
DEER PARK, LI, NY 11729
RP SHERMAN
TONY DOMINIC

GENERAL DYNAMICS ELECTRONICS
PO BOX 81127
SAN DIEGO, CA 92138
CJ MEIERBACHTOL, MZ 7-61
G TRICOLES

HUGHES AIRCRAFT COMPANY
MISSILE SYSTEMS DIVISION
CANOGA PARK, CA 91304
PM ROBBINS
CE WOODBURN
RE NIELSEN

GEORGIA INSTITUTE OF TECHNOLOGY
ATLANTA, GA 30332
HL BASSETT
JN HARRIS

MOTOROLA
GOVERNMENT ELECTRONICS DIVISION
8201 E MC DOWELL ROAD
SCOTTSDALE, AZ 85252
DR L LANGLEY
EA HARRIS
JOHN JONES

RAYTHEON COMPANY
MISSILE SYSTEMS DIVISION
HARTWELL ROAD
BEDFORD, MA 01730
TAFT MURRAY

TEXAS INSTRUMENTS, INC
PO BOX 6015
DALLAS, TX 75222
D PURINTON